University of East Anglia

Identifying Glacial Meltwater in the Amundsen Sea

Louise Catherine Biddle

A thesis submitted for the degree of Doctor of Philosophy

Centre for Ocean and Atmospheric Sciences,
School of Environmental Sciences,
University of East Anglia

April 2016

Supervised by:
Prof. Karen J. Heywood (University of East Anglia),
Prof. Jan Kaiser (University of East Anglia) and
Prof. Adrian Jenkins (British Antarctic Survey)

Word Count: 40,148 words

Funded by NERC PhD Studentship 1210192

Abstract

Pine Island Ice Shelf (PIIS), in the Amundsen Sea, is losing mass due to warm ocean waters melting the ice from below. The glacial meltwater appears as a warmer and more saline water mass (with lower O_2 concentration) than the Winter Water. Tracing meltwater pathways from ice shelves is important for identifying the regions most affected by the increased input of this water type.

Water mass characteristics (temperature, salinity, O_2 concentration) are used to calculate glacial meltwater fractions (MW). The observations from the Amundsen Sea show a plume of MW travelling away from PIIS along σ = 27.7 kg m^{-3}, out to the continental shelf edge. We investigate the reliability of the interpretation of the observations as a signature of MW.

Physical and biological processes can affect the calculated apparent MW by causing variations in the water mass characteristics. In the Weddell Sea, iceberg meltwater was found to enhance biological productivity. In the Amundsen Sea, the biological productivity was seen to artificially decrease the apparent MW signature. We analyse the effects of these processes on the reliability of the calculated meltwater fractions using a modified one-dimensional ocean model. The model simulates the effects of an increase in sea ice production and an influx of Lower CDW, as well as biological activity. These processes are found to result in an observation that can conventionally be interpreted as a meltwater signature, similar to the plume observed at the continental shelf edge.

Recommendations are made to improve the reliability of MW calculations, including the identification of a 'pseudo'-CDW endpoint and to increase the uncertainty associated with the O_2 concentrations. A meltwater pathway leading to the west of PIIS, along the coastline, is observed. This has implications for water mass characteristics further to the west and ultimately AABW formation in the Ross Sea.

Publication

Chapter 4 has been previously published as a paper in *Geophysical Research Letters* under the title 'Ocean glider observations of iceberg-enhanced biological production in the northwestern Weddell Sea', with co-authors Jan Kaiser, Karen J. Heywood, Andrew F. Thompson and Adrian Jenkins. All writing and work was undertaken by L. C. Biddle, with comments and input from collaborators. It is as published, except for the inclusion of a supplementary figure and more discourse on Seagliders, which have been added for increased understanding of data collection.

Biddle, L. C., J. Kaiser, K. J. Heywood, A. F. Thompson, and A. Jenkins (2015), Ocean glider observations of iceberg-enhanced biological production in the northwestern Weddell Sea, *Geophys. Res. Lett., 42,* 459–465, doi:10.1002/2014GL062850.

Acknowledgements

This thesis could not be what it is without the help of a huge amount of people: friends and colleagues at UEA and other institutes, family members and of course all the crew from the *JCR* and *Cook* during the three cruises I was lucky enough to participate in. I can't name everyone, but know I am thankful to all who I've worked with over the last few years.

For countless laughs, tea breaks, exercise-ball-bouncing and generally keeping me sane through the last few months of the thesis (despite the distance): thank you office 3.17 (past & present, and adopted members!). Moving to Baldock was a big risk, but knowing you guys were at the other end of the phone was a huge support, and I physically could not have done it without the enormous generosity of Rich and Osgur. Thank you so much, and I probably owe you quite a few beers! Thanks must also go to Gareth, Bastien and Ben for all the lessons and fun with the Seagliders (and hilarious dancing lessons from Marina in Oban!).

To my supervisors – your patience and gentle prodding in the right direction was invaluable. Karen, I've always remembered your description of the PhD as "an apprenticeship in research" – I think it's fair to say that I've embraced that and had a huge amount of experiences in just over 3 years! I am truly grateful for both the academic and emotional support you've provided during that time. Jan and Adrian, thank you for extending my skills into (basic) biogeochemistry and (simple) modelling. I've had a lot of fun with all of the different aspects of this thesis, and I certainly have your encouragement to thank for that!!

Finally, thank you to my family. Dan, for providing annoying 'dad jokes' when I was feeling rather stressed with the thesis (and whisky)! And to Alex, for all of your wonderful support and proof-reading – thank you!

I don't think I can ever put into words how grateful I am to Mum and Harry, but I'll try. Mum, thank you for letting me disappear off to the Arctic when I was 17, and waving me off again 2 years later despite falling down crevasses the first time! You have always been such a great support for me, and your strength has often kept me going. And Harry, thank you for the many cups of tea and encouragement over the last few years, quietly supporting me every day through the highs and lows. You're my rock.

Contents

List of Figures

List of Tables

Chapter 1

Introduction

1.1 Background

The winter of 2015/2016 was the warmest winter for England, Wales and the USA since records began (Met Office, 2016; NOAA, 2016). These records reflect global trends of increasing temperatures (NASA/GISS, 2016). In December 2015, a climate deal – the 21st Conference of the Parties (COP21) in Paris – was signed by more than 190 countries, aiming to cut emissions and keep temperature increases below 2 °C (UNFCCC, 2016). The scientific consensus is that man-made climate change is happening, but climate models still contain uncertainties that prevent the community from knowing exactly how likely some of the global changes they forecast might be (Field *et al.*, 2014; Thompson *et al.*, 2015). A significant source of these uncertainties are the processes around the Antarctic continent; what controls the ice shelf melt, how will the melt impact other parts of the climate system and will there be feedbacks that we do not yet know of?

Feedbacks linked to the introduction of the fresh, cold glacial meltwater into the ocean can be identified in models (Richardson *et al.*, 2005). The addition of this water mass results in freshening of other nearby water masses (Jacobs and Giulivi, 2010), and if it enters the ocean in the surface layers then it may also influence sea

ice processes (Bintanja *et al.*, 2013). This thesis focuses on how glacial meltwater is identified in the Amundsen Sea (Figure 1.1), and aims to provide a more reliable method of meltwater calculation in order to trace meltwater pathways from this region.

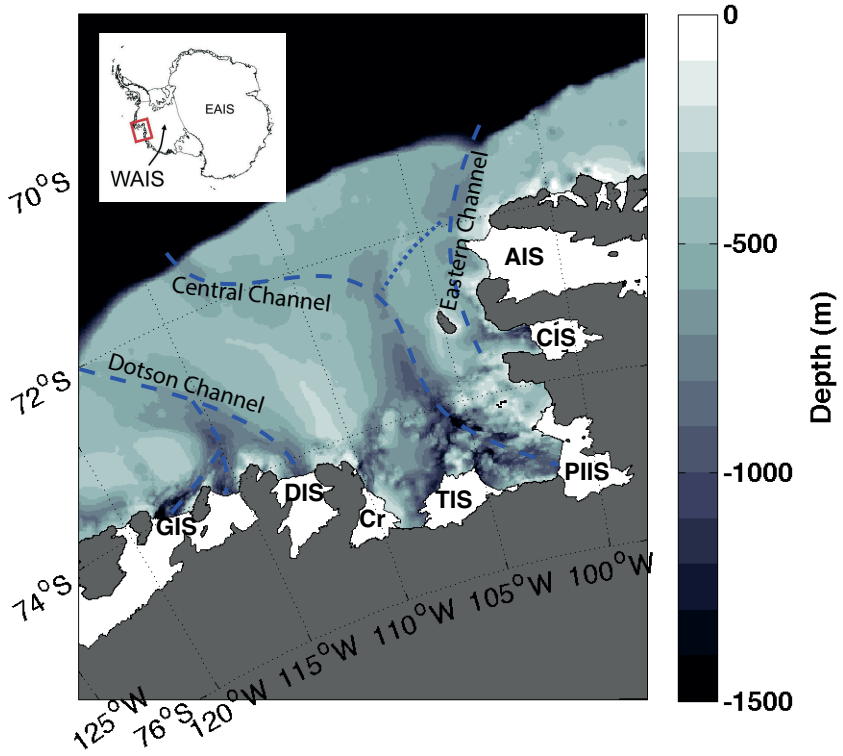

Figure 1.1: Map of the Amundsen Sea. The inset shows the area of the West Antarctic Ice Sheet (WAIS) and location of the Amundsen Sea in Antarctica (red box; from the British Antarctic Survey AmuNdsen Sea Embayment Exposure Dating project, BAS 2016). The bathymetry of the Amundsen Sea is shown in greyscale, with Abbott Ice Shelf (AIS), Cosgrove Ice Shelf (CIS), Pine Island Ice Shelf (PIIS), Thwaites Ice Shelf (TIS), Crosson Ice Shelf (Cr), Dotson Ice Shelf (DIS) and Getz Ice Shelf (GIS) identified on the map. The three main glacial channels in the region are traced with dotted lines, and labelled Eastern, Central or Dotson.

1.2 The Amundsen Sea and Pine Island Ice Shelf

The West Antarctic Ice Sheet (WAIS; Figure 1.1) holds up to 3.3 m of potential sea level rise in its glaciers and ice shelves (Bamber *et al.*, 2009), and has been observed to contain some of the fastest melting ice shelves around Antarctica (over 40 m yr^{-1}; Pritchard *et al.*, 2012). The WAIS consists of many marine based glaciers, where

the base of the glacier is below sea level and generally on reverse slope gradients (becoming deeper inland; Schoof, 2007). This predisposes the glaciers to retreat due to the forcing of the 'warm' waters from the ocean, and the retreat is only slowed by ridges in the bedrock. The glaciers terminate in ice shelves floating on the ocean.

One region of the WAIS with fast melt rates is the Amundsen Sea Embayment, containing the termini of Pine Island Glacier (PIG), Thwaites Glacier and several others (Figure 1.1). Each of these glaciers have ice shelves, and Pine Island Ice Shelf (PIIS) in particular has received increased attention over the last 20 years (Jacobs *et al.*, 2012). A research cruise to the region in 1994 identified warm Circumpolar Deep Water (CDW) on the continental shelf, with access to the cavity under the ice shelf, overlain by a colder and less saline Winter Water layer (Jacobs *et al.*, 1996). The warm CDW was over 3 °C warmer than the in-situ melting point of the base of PIIS at 800 m depth, and so resulted in melting of the ice shelf from below, termed 'oceanic basal melting' (Jacobs *et al.*, 1996). From the observations in 1994, the melt rates were assumed to be balanced by snowfall on the continent, and so the glacier was in an equilibrium state (Vaughan, 2001). However, improvements in satellite observations of ice shelf velocity and thickness began to show that these glaciers were not in balance, and instead were rapidly thinning (up to 5.5 m yr^{-1}; Rignot, 1998; Shepherd *et al.*, 2004; Rignot *et al.*, 2008). Modelling studies demonstrated that this thinning observed by satellites over 200 km from the front of the ice shelf is closely linked to the oceanic basal melt (Payne *et al.*, 2004).

This discovery motivated further research cruises to the region, including the usage of autonomous underwater vehicles (AUV) such as Autosub3 (Jenkins *et al.*, 2010; Jenkins *et al.*, 2012; Jacobs *et al.*, 2012). This AUV was able to collect temperature, salinity and bathymetry data (amongst others) from underneath the ice shelf. One of the most important results from the Autosub3 was the discovery of a ridge running across the cavity, reaching up to 600 m below sea level (Figure 1.2; Jenkins *et al.*, 2010). The ice shelf itself descends down to about 400 m below sea level, so

the combination of the ice shelf and the ridge made a narrow 200 m gap for water to flow through in order to melt at the grounding line (the point where the glacier begins to float and becomes an ice shelf). Thinning of the ice shelf likely resulted in the grounding line moving off this ridge, and rapidly retreating down the steep slope, opening a cavity behind (Jenkins *et al.*, 2010; Figure 1.2). The rate of melting

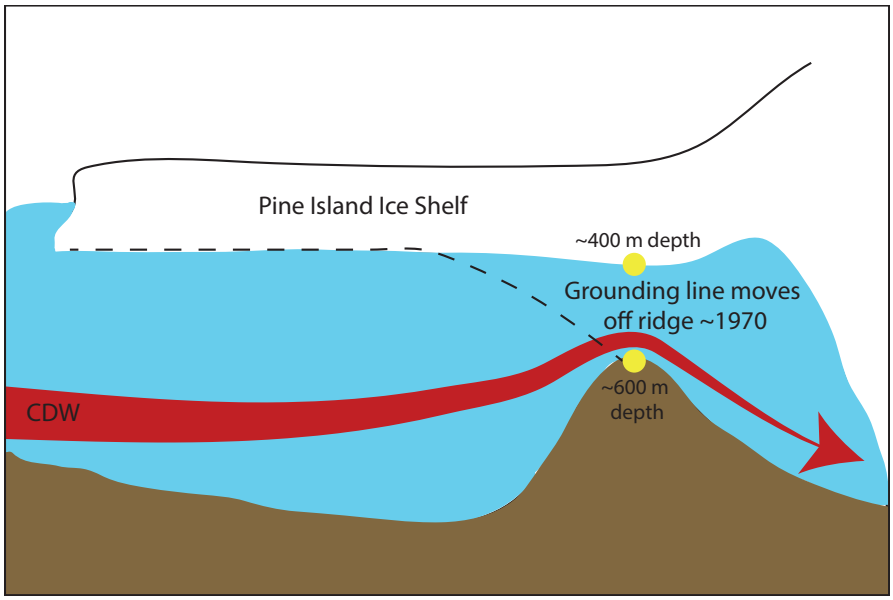

Figure 1.2: Schematic (not to scale) showing the approximate bathymetry under Pine Island Ice Shelf. The ridge extends up to 600 m below sea level, whilst the base of the ice shelf descends down to 400 m below sea level. Before 1970, satellite data suggest that the grounding line of Pine Island Glacier rested on the top of the ridge (dotted black line), before rapidly retreating downslope. Warm Circumpolar Deep Water (CDW) can access the cavity and melts PIG from the grounding line.

at the grounding line is largely controlled by how much 'warm' water reaches this point. This is driven by the strength of circulation within the cavity and the depth of the thermocline, affecting the amount of CDW that can get under the ice shelf and over the ridge (Jenkins *et al.*, 2010; Jacobs *et al.*, 2011; Dutrieux *et al.*, 2014). How these two variables change is still poorly understood and is an important element to consider in order to improve global climate models.

Over the years several models have been developed for this region in order to try to understand the variability in CDW transport (Thoma *et al.*, 2008; Schodlok *et al.*, 2012; Assmann *et al.*, 2013). The CDW is known to travel along ancient glacially-

carved channels that reach across the continental shelf (Nitsche *et al.*, 2007; Walker *et al.*, 2007; Wåhlin *et al.*, 2010), becoming modified CDW (mCDW) in the process. There are two channels that lead from the shelf edge to PIIS: the eastern channel at 103 °W and the central channel at 113 °W. The main processes that the models aim to identify are how the CDW gets into these channels and what controls the variability in the on-shelf transport.

Schodlok *et al.* (2012) and Assmann *et al.* (2013) favour the eastern channel as the main supply of mCDW to PIIS, but Thoma *et al.* (2008) also show the central channel as another source of the mCDW. Part of the reason for these differences could be the resolution of the bathymetry used (Assmann *et al.*, 2013). Observations from across the continental shelf show that whilst the warmest CDW may flow onto the continental shelf through the eastern channel, over half of the mCDW that makes its way to PIIS comes from the central trough (Nakayama *et al.*, 2013). The model results from Thoma *et al.* (2008) and Assmann *et al.* (2013) show that this mCDW is transported into the central channel by an undercurrent at the shelf break, and observations collected from the shelf edge support this (Walker *et al.*, 2007, 2013; Assmann *et al.*, 2013). Model results indicate that the variability in the transport of CDW on-shelf is driven by changes in the wind (Thoma *et al.*, 2008), and some studies have linked large-scale atmospheric oscillations to variability seen in observations in this region (Steig *et al.*, 2012; Dutrieux *et al.*, 2014). These variations at the shelf edge may help explain the variability seen in front of PIIS in the thickness of the CDW. The modified CDW travels further onto the continental shelf along the glacially carved channels, and southwards to the front of PIIS (Figure 1.3). The eastern and central channels merge around 72° S, and the main channel then deepens towards the south (Nitsche *et al.*, 2007). The transport here is geostrophic, with southward flow on the eastern flank of the channel and northward flow on the western side (Schodlok *et al.*, 2012; Nakayama *et al.*, 2013). This is reflected in where inflow and outflow under PIIS are seen: the strongest inflow of mCDW is seen at the

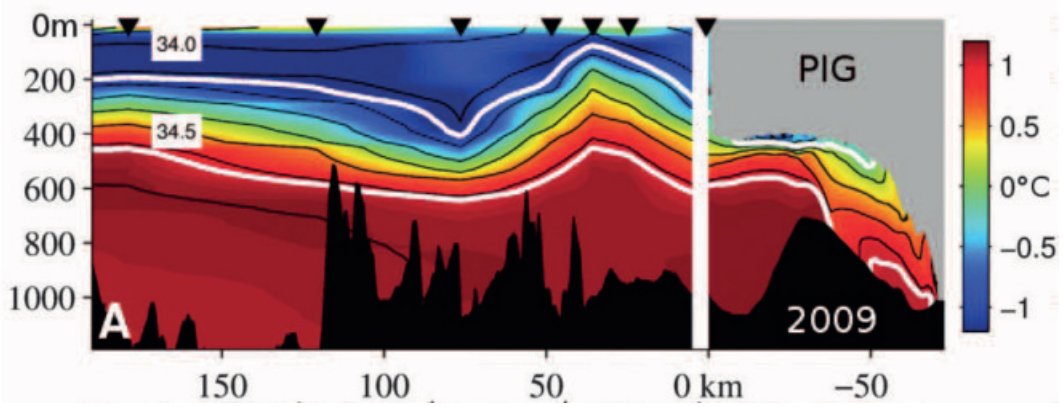

Figure 1.3: Section showing potential temperature (coloured) from the middle of the Amundsen Sea shelf to underneath Pine Island Glacier (PIG). Salinity contours are marked on in black, with 34.0 and 34.5 highlighted in white. The warm CDW can be seen underneath the ice shelf. Sourced from Dutrieux et al.*, 2014.*

northeastern end of the ice shelf, and the Coriolis-deflected outflow of mCDW mixed with glacial meltwater is seen at the southwestern end (Jacobs *et al.*, 1996; Jacobs *et al.*, 2011; Thurnherr *et al.*, 2014).

In front of PIIS, a cyclonic gyre has often been observed, likely due to the winds blowing off of the front of PIIS (Hellmer *et al.*, 1998; Jacobs *et al.*, 2011; Thurnherr *et al.*, 2014). Modelling studies have also shown that the volume of meltwater outflow from PIIS can contribute to the transport of this gyre through buoyancy forcing (Thurnherr *et al.*, 2014). This result shows the importance of understanding the meltwater outflow and where it goes once it has left the ice cavity.

Above the mCDW there is a layer of Winter Water (WW). This is a cooler and fresher water mass formed during each winter season through loss of heat to the atmosphere. The water mass characteristics are influenced by sea ice processes, and this region typically has sea ice cover throughout the year (approximately 25 - 40 % in February, 80 - 95 % in November, Figure 1.4; Stammerjohn *et al.*, 2015).

1.3 Meltwater in the Amundsen Sea

PIIS meltwater is often identified using a technique established by Jenkins (1999). This method uses temperature, salinity and dissolved oxygen concentrations to dis-

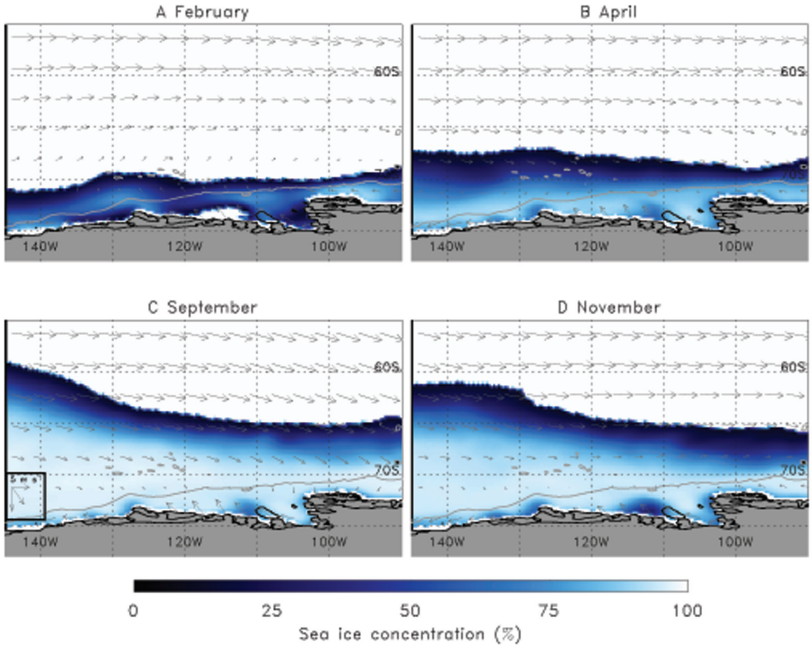

Figure 1.4: Maps showing the mean sea ice concentration for the month labelled (from Stammerjohn et al.*, 2015). A) February, B) April, C) September and D) November. The mean is calculated between 1979 - 2012 and the colour scale shows the sea ice concentration, the grey arrows show the wind speed (scale in panel C) and the grey line shows the 2000 m isobath.*

tinguish between different water masses and provide a fraction of glacial meltwater present in the water column. Observations of the glacial meltwater directly in front of PIIS have shown variability reflecting the thickness of the mCDW on shelf: the lowest melt rates were observed in 2012, when the thermocline was deepest (Dutrieux *et al.*, 2014). Few studies have published results on glacial meltwater observations further from the front of PIIS due to uncertainty in the reliability of the measurements (Jenkins, *pers. comm.*). However, further to the west, hydrographic observations have suggested the presence of glacial meltwater at the shelf edge of Dotson Trough (Randall-Goodwin *et al.*, 2015), supported by recent noble gas datasets (Kim *et al.*, 2016).

In addition to identifying the glacial meltwater to improve understanding of its effects on the local Amundsen Sea processes, it is important to trace where this meltwater goes once it has left the Embayment. Richardson *et al.* (2005) showed model results where the input of significant amounts of glacial meltwater freshened

the Antarctic Bottom Water (AABW) and increased sea ice formation. These processes also had implications for the global meridional overturning circulation, which is an important factor in redistributing heat around the planet. The effects were quickest to occur in the Pacific sector (temperature anomalies after one month), and after the model has simulated 10 years the AABW overturning had decreased by 5 % (Richardson *et al.*, 2005). All three of these modelled effects of the input of glacial meltwater have been observed: freshening of the AABW (Jacobs *et al.*, 2002; Rintoul, 2007; Jacobs and Giulivi, 2010), increases in sea ice area (Bintanja *et al.*, 2013) and a reduction in the northward spread and volume of the AABW in the Pacific Ocean (Kouketsu *et al.*, 2009; Purkey and Johnson, 2012). Of particular interest is

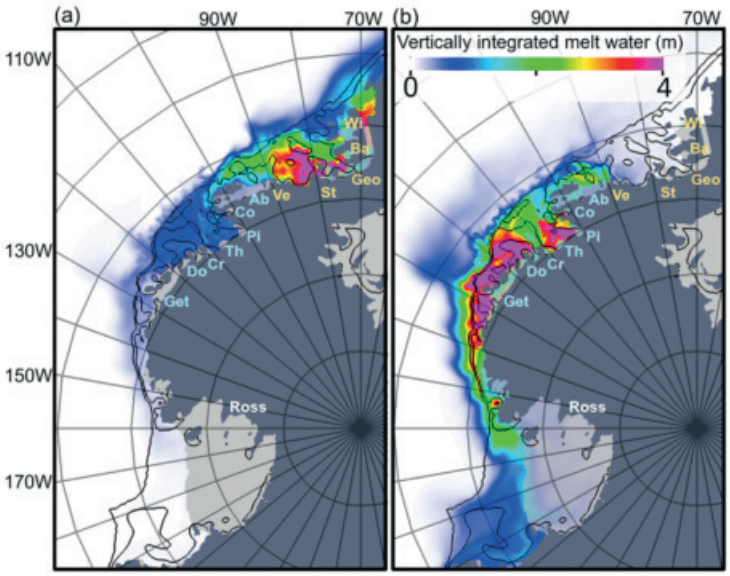

Figure 1.5: Maps showing the spread of glacial meltwater (vertically integrated) from a 10 year model run. The glacial meltwater is modelled as coming from (a) Bellingshausen Sea and (b) Amundsen Sea. Bathymetry contours of 500 m and 1000 m are shown in black, and the ice shelves are labelled in yellow (Bellingshausen Sea) and blue (Amundsen Sea). Pine Island Ice Shelf is 'Pi' (for the full list of acronyms, see Table S1, Nakayama et al.*, 2014). The glacial meltwater from the Amundsen Sea can be clearly seen to reach the eastern boundary of the Ross Sea, where freshening has been observed. Sourced from Nakayama* et al.*, 2014.*

the freshening of the AABW. Between 1958 and 2008, shelf water in the Ross Sea has been observed to be freshening by 0.03 per decade (practical salinity; Jacobs *et al.*, 2002; Jacobs and Giulivi, 2010; Schmidtko *et al.*, 2014). This freshening of the shelf waters has affected the AABW north of the shelf slope by approximately 0.01

per decade (Jacobs and Giulivi, 2010). Using oxygen isotopes, it has been shown that this freshening is most likely due to increased input of glacial meltwater as opposed to increased precipitation or sea ice melt (Jacobs and Giulivi, 2010). The westward coastal current entering the Ross Sea has freshened by 0.08 per decade (measured between 1967-2007; Jacobs and Giulivi, 2010), implicating the WAIS as a source for these less saline waters. A recent model study (Nakayama *et al.*, 2014) shows glacial meltwater from the Bellingshausen and Amundsen Seas joining the coastal current and entering the Ross Sea, reproducing the observations there (Figure 1.5). However, the pathway of glacial meltwater between the WAIS (or Bellingshausen and Amundsen Seas) and the Ross Sea has never been observed in hydrographic data due to the uncertainties associated with the glacial meltwater calculations.

1.4 Identifying glacial meltwater in the Amundsen Sea

One of the largest sources of glacial meltwater is the Amundsen Sea Embayment in Antarctica, particularly PIIS (and its glacier). This region is undergoing oceanic basal melting, where the warm Circumpolar Deep Water is able to access the grounding line of the glaciers. Most model studies and observations have focused on identifying the drivers for the transport of the CDW to the ice shelves, which is an important process for modelling future glacial melting and sea level rise.

Observations and model results from around Antarctica show that understanding the fate of the glacial meltwater is essential in order to improve global climate models and forecast future climate scenarios better. Potential impacts of increased glacial meltwater input include slow down of AABW formation (with consequential effects on the global meridional overturning circulation) and changes to sea ice formation rates. Some of these effects have already begun to be observed, most distinctly in the freshening of the Ross Sea shelf waters.

The first step on the path to improve knowledge of meltwater pathways is to be

able to confidently identify the presence of glacial meltwater as it travels across the continental shelf in the Amundsen Sea. In this thesis, I will aim to improve current glacial meltwater fraction calculations and identify the main processes that lead to uncertainties in this measurement.

The current calculation methods for glacial meltwater will be assessed in Chapter 2 and uncertainties associated with each method identified. Observational data from a recent research cruise will be presented in Chapter 3, including definitions of the water masses present on the continental shelf for 2014. Processes that may have affected the measurements will be identified (Chapter 3), including a case study observing the relationship between iceberg meltwater and biological productivity in the Weddell Sea (Chapter 4). Some of these processes are verified using a simple one dimensional ocean model, which has been developed for use in this region (Chapter 5). Finally, a recommendation for future glacial meltwater calculations in the Amundsen Sea will be made (Chapter 6). The linkages between each of these chapters (and constituent parts) can be seen in Figure 1.6.

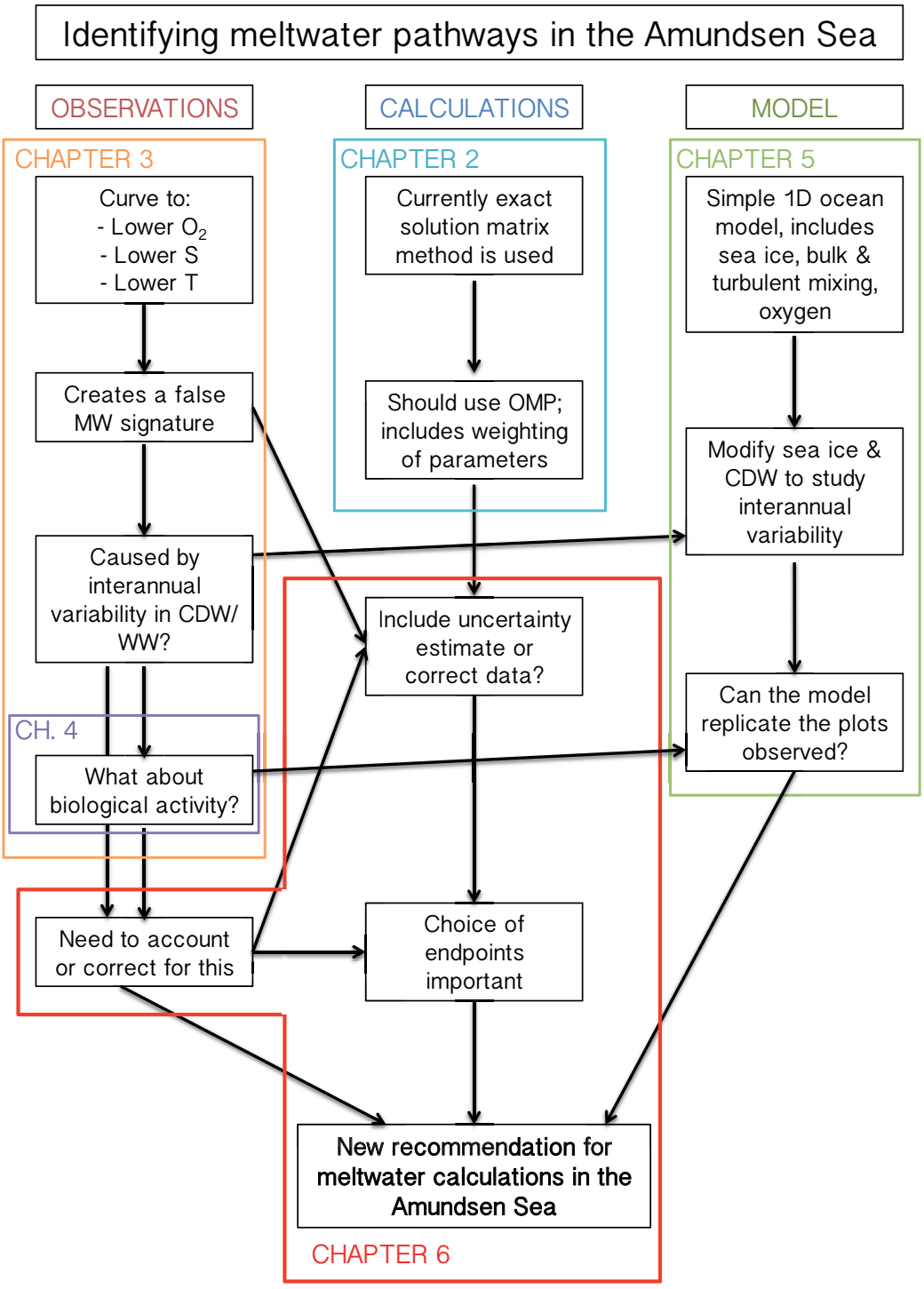

Figure 1.6: Schematic showing the different areas focused on in this thesis; the hydrographic observations, the methods of meltwater calculations and the one dimensional ocean model. The constituent parts of these areas are highlighted, with connectivity between these parts identified. Finally, boxes are shown indicating what areas are covered in each chapter.

Chapter 2

Meltwater Identification Methods

2.1 Introduction

Pine Island Ice Shelf (PIIS), as well as other ice shelves fringing the West Antarctic Ice Sheet, has been observed to be melting rapidly in recent years, increasing the input of glacial meltwater (MW) into the Amundsen Sea (Pritchard *et al.*, 2012). In order to track the meltwater we need to be able to confidently identify the meltwater fraction within the water column as it travels away from the ice shelf.

Water mass identification methods were developed following large-scale oceanic data collection efforts at the start of the 20th century (Tomczak, 1981). These data led to Wüst's diagrams and description of Southern Ocean water masses and circulation (Wüst, 1935) and Sverdrup's description of global water masses (Sverdrup, 1942), both of which are still used today. Water mass analysis also identified the oceanic equivalent of atmospheric mesoscale and weather effects, changing the way oceanographers thought about ocean processes and again highlighting the importance of understanding where water masses originate.

In order to quantify distinct water masses, we need to be able to identify their individual fingerprint, typically using the conservative properties of that water mass on a property-property diagram. A conservative property is one that does not vary in

a fluid parcel except through physical mixing processes, such as air-sea interaction or water mass mixing, with conservative temperature and absolute salinity (IOC *et al.*, 2010) the most common examples of these. It is also important here to establish the differences between 'water mass' and 'water type'. A water mass is the oceanic representation of a water type. The water type relates to a single point on a property-property diagram (characteristic temperature and salinity), whereas a water mass is representative of the ocean observations and will typically occupy some space around the water type on the property-property plot. Throughout this thesis, 'water type' (or 'source water type') will be interchangeable with 'endpoints', which are used to describe the central point of a water mass. On the Amundsen Sea continental shelf, the modifed Circumpolar Deep Water (mCDW) has a characteristic absolute salinity of 34.88 g kg^{-1} and conservative temperature of 1.23 °C, whilst Winter Water (WW), by comparison, is cooler (-1.7 °C) and fresher (34.3 g kg^{-1}). When these two water masses mix, the resulting water parcels (e.g. red dot, Figure 2.1) will lie along a line connecting the two water masses, and the respective fractions of each water mass can be calculated.

Other tracers, such as dissolved oxygen and silica, are biogenic, meaning they are affected by biological activity (production, respiration, oxidation and remineralisation) as well as mixing processes, making them non-conservative properties. If these non-conservative processes are small or can be accounted for, then these properties are useful when identifying water masses.

This chapter will look at and compare the methods of water mass identification. It is also important how the end-points – or source water types – are selected, and the effects of uncertainty in this will also be discussed. A method of meltwater identification will be established for this thesis.

2.2 Water mass identification

The method chosen for water mass identification is dependent on how many tracers are available to be used (n_t, including the equation for mass conservation), and how many water masses are present in the region of interest (n_w). Typically, this will produce either an exact system, where $n_t = n_w$, or an over-determined system, where $n_t > n_w$. In some cases, $n_t < n_w$, and this would be an under-determined system. This study will only focus on the exact and over-determined systems.

2.2.1 Exact system method

An exact system is one where the number of tracers (n_t) available to be used equals the number of unknowns ($n_t = n_w$; where mass conservation is included as a tracer). As mass must be conserved, there is always one 'tracer' available to be used;

$$x_{\mathrm{mCDW}} + x_{\mathrm{WW}} + x_{\mathrm{MW}} = 1, \tag{2.1}$$

where x_k is the fraction for water type k. This means that for the exact system method (ESM), the number of water mass tracers required is one less than the number of water masses to be identified. In the Amundsen Sea, we are interested in identifying three water masses, mCDW, WW and MW, which will only need two tracers, χ_1 and χ_2. We then obtain two more equations describing the water mass fractions;

$$\chi_{1,\mathrm{mCDW}}\ x_{\mathrm{mCDW}} + \chi_{1,\mathrm{WW}}\ x_{\mathrm{WW}} + \chi_{1,\mathrm{MW}}\ x_{\mathrm{MW}} = \chi_{1,\mathrm{obs}}, \tag{2.2}$$

$$\chi_{2,\mathrm{mCDW}}\ x_{\mathrm{mCDW}} + \chi_{2,\mathrm{WW}}\ x_{\mathrm{WW}} + \chi_{2,\mathrm{MW}}\ x_{\mathrm{MW}} = \chi_{2,\mathrm{obs}}. \tag{2.3}$$

There are now three equations for three unknowns. These equations can be amalgamated and written as a matrix calculation:

$$\begin{pmatrix} \chi_{1,\mathrm{mCDW}} & \chi_{1,\mathrm{WW}} & \chi_{1,\mathrm{MW}} \\ \chi_{2,\mathrm{mCDW}} & \chi_{2,\mathrm{WW}} & \chi_{2,\mathrm{MW}} \\ 1 & 1 & 1 \end{pmatrix} \begin{pmatrix} x_{\mathrm{mCDW}} \\ x_{\mathrm{WW}} \\ x_{\mathrm{MW}} \end{pmatrix} = \begin{pmatrix} \chi_{1,\mathrm{obs}} \\ \chi_{2,\mathrm{obs}} \\ 1 \end{pmatrix}, \tag{2.4}$$

$$\mathbf{A}\mathbf{x} = \mathbf{b}, \tag{2.5}$$

where **A** is the matrix containing the water mass characteristics, **x** is the array of water mass fractions and **b** is the array containing observational data. This matrix equation is easily solved to provide the three water mass fractions, but can provide values of $x_i < 0$.

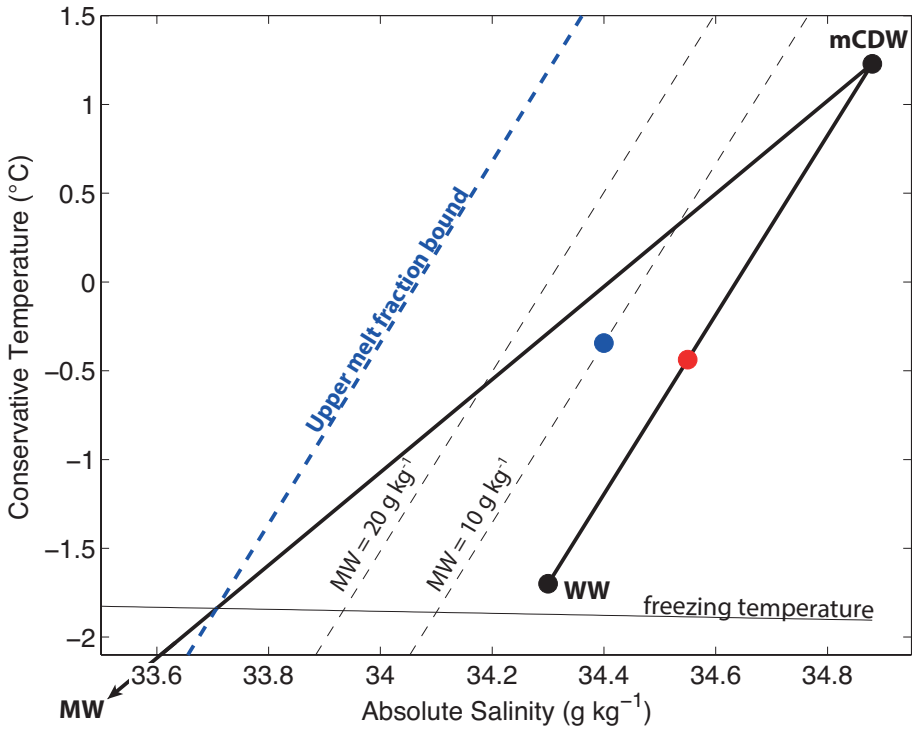

Figure 2.1: Schematic diagram showing the linear mixing lines that exist in conservative temperature - absolute salinity (Θ-S_A) space between mCDW and WW, and mCDW and MW, where S_A is χ_1 and Θ is χ_2. In the ambient water column any data point (e.g. red dot) will lie along the mCDW-WW line, whilst as soon as meltwater has been added to the water column the data point (e.g. blue dot) will move off this line into the triangular mixing space formed. The meltwater fraction increases parallel to the ambient mixing line, with a maximum melt fraction imposed by the minimum temperature possible in the water column.

2.2.2 Composite tracer method

In the Amundsen Sea region, a meltwater fraction calculation described by Jenkins (1999) is the most commonly used. This method creates a composite tracer that uses the mixing line between mCDW and WW (Figure 2.1). This is referred to as the ambient mixing line, as we should expect all data points to fall on it when no meltwater is present (e.g. red dot, Figure 2.1, equation 2.6). If observations are taken from a water column that contains only mCDW and WW (the ambient water column), then the gradient between any data point and the mCDW endpoint will be equal to the gradient of the ambient mixing line (equation 2.7).

$$\frac{\mathrm{d}\chi_2}{\mathrm{d}\chi_1} = \frac{\chi_{2,\mathrm{mCDW}} - \chi_{2,\mathrm{WW}}}{\chi_{1,\mathrm{mCDW}} - \chi_{1,\mathrm{WW}}}, \tag{2.6}$$

$$\frac{\mathrm{d}\chi_2}{\mathrm{d}\chi_1} = \frac{\chi_{2,\mathrm{mCDW}} - \chi_{2,\mathrm{obs}}}{\chi_{1,\mathrm{mCDW}} - \chi_{1,\mathrm{obs}}}, \tag{2.7}$$

where χ represents the tracer measured, e.g. Θ or S_A. The composite tracer, $\psi_{1,2}$, is calculated by setting the right hand side (RHS) of equation 2.6 equal to the RHS of equation 2.7, which is possible as both of the left hand sides (LHS) of the equations are the same. This new equation can be rearranged so that all constituent parts are on the RHS, and set equal to the composite tracer, $\psi_{1,2}$ (equation 2.8). This equation is equal to zero for any data point that is in the ambient water column (equation 2.9).

$$\psi_{1,2} = 0 = (\chi_{2,\mathrm{mCDW}} - \chi_{2,\mathrm{obs}}) - (\chi_{1,\mathrm{mCDW}} - \chi_{1,\mathrm{obs}})\left(\frac{\chi_{2,\mathrm{mCDW}} - \chi_{2,\mathrm{WW}}}{\chi_{1,\mathrm{mCDW}} - \chi_{1,\mathrm{WW}}}\right), \tag{2.8}$$

$$\psi_{\mathrm{w}} = 0. \tag{2.9}$$

The value of ψ will become non-zero if a process such as a new water mass mixing with the ambient water column occurs, moving the data point (e.g. blue dot, Figure 2.1) off the ambient mixing line. It is assumed here that the only water mass that can do this is glacial meltwater. This assumption will be critically assessed in Chapter 3.

The value of ψ in meltwater (ψ_{ice}) is:

$$\psi_{ice} = (\chi_{2,mCDW} - \chi_{2,MW}) - (\chi_{1,mCDW} - \chi_{1,MW}) \left(\frac{\chi_{2,mCDW} - \chi_{2,WW}}{\chi_{1,mCDW} - \chi_{1,WW}} \right). \quad (2.10)$$

The measured data point can then be assumed to consist of some fraction (Q_w or Q_{ice}) of each of the two established values of composite tracer (ambient water; ψ_w, and ice; ψ_{ice}).

$$Q\psi_{1,2} = \cancel{Q_w \psi_w} + Q_{ice}\psi_{ice}, \quad (2.11)$$

where $Q\psi_{1,2}$ represents the data point measured. In the ambient water column, the composite tracer is equal to zero ($\psi_w = 0$; equation 2.8), and so this term is removed from equation 2.11. This equation can then be rearranged to calculate the fraction of meltwater present in the water column:

$$x_{MW\ 1,2} = \frac{Q_{ice}}{Q} = \frac{\psi_{1,2}}{\psi_{ice}}. \quad (2.12)$$

Upper and lower bounds can be applied to this calculation. The lower bound is zero, as there can be no negative concentration of meltwater, whilst the upper bound is controlled by the amount of melt possible when the ambient water column temperature has been reduced to the freezing point (Θ_{fp}):

$$x_{MW,upperbound} = \left(\frac{\Theta_{mCDW} - \Theta_{fp}}{\Theta_{mCDW} - \Theta_{MW}} \right). \quad (2.13)$$

Figure 2.1 shows the upper bound mixing line and how the meltwater fraction increases with distance from the ambient mixing line.

Similarly to the ESM outlined earlier, the composite tracer method can only be used with two tracers at any time, and in the Amundsen Sea, is typically used with temperature, salinity and dissolved oxygen concentration. The combination of these three tracers provides three estimates of meltwater fraction, which are simply averaged to get the final solution (equation 2.14).

$$x_{\mathrm{MW,av}} = \frac{x_{\mathrm{MW\ 1,2}} + x_{\mathrm{MW\ 1,3}} + x_{\mathrm{MW\ 2,3}}}{3}. \tag{2.14}$$

This method is in fact the same calculation as the ESM outlined in section 2.2.1 (for proof, see Appendix A).

2.2.3 Over-determined system method

An over-determined system is one where the number of tracers available outnumbers the amount of unknowns (where mass conservation is included as a tracer; $n_{\mathrm{t}} > n_{\mathrm{w}}$). This results in the source water matrix (**A**) and the water mass fractions vector (**x**) being different dimensions;

$$\begin{pmatrix} \chi_{1,\mathrm{mCDW}} & \chi_{1,\mathrm{WW}} & \chi_{1,\mathrm{MW}} \\ \chi_{2,\mathrm{mCDW}} & \chi_{2,\mathrm{WW}} & \chi_{2,\mathrm{MW}} \\ \chi_{3,\mathrm{mCDW}} & \chi_{3,\mathrm{WW}} & \chi_{3,\mathrm{MW}} \\ 1 & 1 & 1 \end{pmatrix} \begin{pmatrix} x_{\mathrm{mCDW}} \\ x_{\mathrm{WW}} \\ x_{\mathrm{MW}} \end{pmatrix} = \begin{pmatrix} \chi_{1,\mathrm{obs}} \\ \chi_{2,\mathrm{obs}} \\ \chi_{3,\mathrm{obs}} \\ 1 \end{pmatrix}, \tag{2.15}$$

$$\mathbf{Ax} = \mathbf{b}. \tag{2.16}$$

In an over-determined system, there could be 0 or 1 exact solutions. However, in general there will be no exact solution due to measurement errors and other uncertainties. The 'best' solution is found by minimising the residual between the modelled observations from the fractions calculated and the real observations ($\mathcal{D}^2$; equation 2.17):

$$\mathcal{D}^2 = (\mathbf{Ax} - \mathbf{b})^{\mathbf{T}} \mathbf{W}^{\mathbf{T}} \mathbf{W} (\mathbf{Ax} - \mathbf{b}). \tag{2.17}$$

where we minimise $\mathcal{D}^2$, apply non-negativity constraints on **x**, **W** is the weighting matrix and $\mathbf{W}^{\mathbf{T}}$ represents the transpose of the matrix **W**. This form of water mass identification is described by Tomczak and Large (1989) and developed further by

Karstensen and Tomczak (1997). The method is used widely in both polar and tropical regions (c.f. Poole and Tomczak, 1999; Beaird *et al.*, 2015), and is known as 'Optimum Multi-Parameter Analysis' or OMPA.

The tracers used in the source water matrix (**A**) are typically spread over very different ranges and are in different units. This means that it is important to normalise these measurements. The mean and standard deviation of each tracer in the source water matrix **A** are used ($\bar{A_i}$, σ_i; equation 2.18) so that **A** will have a mean of 0 and variance of 1 (renamed G). The observational data will also lie within this range, and the array is renamed d.

$$G_{ij} = \frac{A_{ij} - \bar{A_i}}{\sigma_i}, \quad d_i = \frac{b_i - \bar{A_i}}{\sigma_i}, \tag{2.18}$$

where

$$\bar{A_i} = \frac{1}{n_\mathrm{w}} \sum_{j=1}^{n_\mathrm{w}} A_{ij} \quad \text{and} \quad \sigma_i = \sqrt{\frac{1}{n_\mathrm{w} - 1} \sum_{j=1}^{n_\mathrm{w}} (A_{ij} - \bar{A_i})^2}. \tag{2.19}$$

Following the normalisation, G and d are weighted (becoming $\tilde{G}$ and $\tilde{d}$; equation 2.20), in order to balance the relative inputs from each tracer and to account somewhat for uncertainties in the observed tracers.

$$\tilde{G_{ij}} = G_{ij}\ W_{ii} \quad \text{and} \quad \tilde{d_i} = d_i\ W_{ii}. \tag{2.20}$$

The weighting matrix, as used in equation 2.20, is calculated using the variance in the endpoints in the source water matrix, and the uncertainties associated with each tracer. The uncertainty (υ) is made up of both analytical uncertainty from the measurements and the uncertainty associated with setting the endpoints (the environmental uncertainty). The effect of these uncertainties is discussed further in section 2.4. The weights are calculated from:

$$W_{ii} = \frac{\sigma_i^2}{\upsilon_i} \tag{2.21}$$

where σ_i^2 is the variance of tracer i in the source water matrix, and υ_i is the uncertainty

associated with tracer *i*. This dataset and source water matrix are then used to calculate the water mass fractions. Iterations of possible solutions are used to minimize the least squares residual (between model fit and observation), and a non-negativity constraint is enforced. The residuals can be useful to observe whether there are certain depth ranges that have a greater residual (and lower certainty). This OMPA is especially useful for regions with influences from multiple water masses, and can be combined with nutrients or radionuclides to estimate age of each individual water mass (Loose *et al.*, 2009a).

2.3 Comparison of methods

In order to compare the ESM and OMPA for calculating meltwater fractions, a simulated observation dataset ($\tilde{\mathbf{b}}$) was constructed using a set of randomly generated water mass fraction arrays ($\tilde{\mathbf{x}}$) and a source water matrix of mCDW, WW and MW ($\tilde{\mathbf{A}}$). The sum of the water mass fraction array was constrained to equal 1, with meltwater constrained between 0 g kg^{-1} and 25 g kg^{-1}. The meltwater fraction constraints were introduced to ensure that the resultant simulated observational dataset ($\tilde{\mathbf{b}}$) contained values that are within reasonable oceanic measurements. Figure 2.2 shows that $\tilde{\mathbf{b}}$ encompasses a range of values within the mCDW-WW-MW mixing space, also providing a range of meltwater values ($\tilde{\mathbf{x}}$). This set of simulated observations was then used with each method to re-calculate the water mass fractions (**x'**), which can be compared with the original water mass fractions dataset ($\tilde{\mathbf{x}}$).

Using $\tilde{\mathbf{b}}$, both the ESM and OMPA produced **x'** that was identical to $\tilde{\mathbf{x}}$: differences were in the order of the machine precision (10^{-15} to 10^{-16}). This shows that there is no theoretical difference to using either technique.

We can now apply the same comparison exercise to a small portion of a historical dataset. The data we use here are from a transect across the front of the Pine Island Ice Shelf collected during the 2010 Polarstern ANTXXVI/3 cruise to the Amundsen

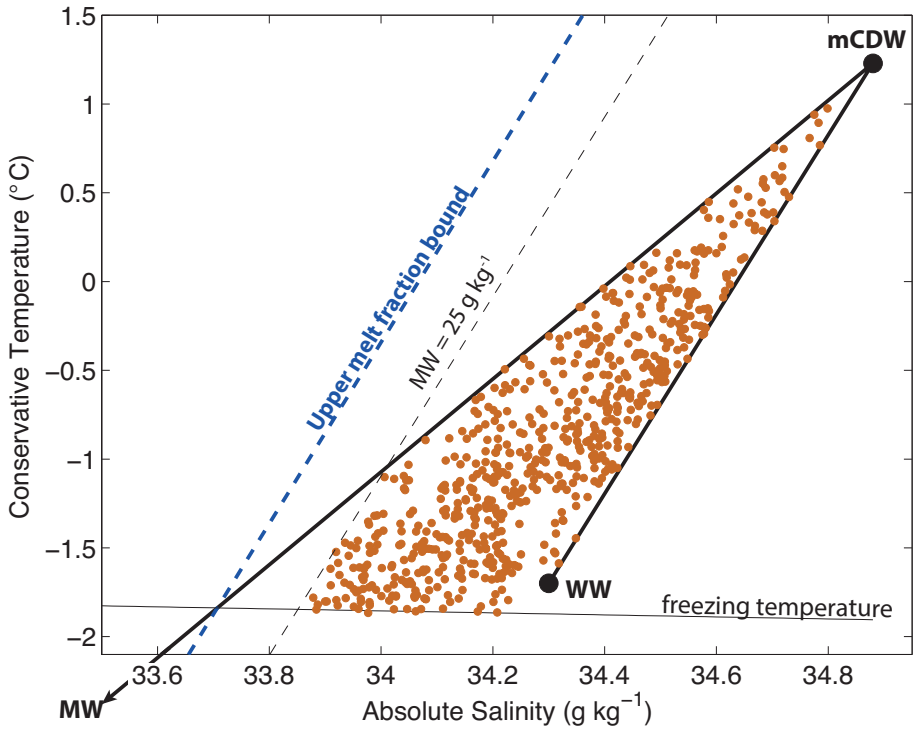

Figure 2.2: Data points generated by running the forward calculation in the ESM (dots). These all lie within the bounds of the mCDW-WW-MW triangular mixing space and are limited by a maximum melt fraction of 25 g kg^{-1}.

Sea (Nakayama *et al.*, 2013; Figure 2.3). This uses stations 152 to 157, where station 157 is at the southern end of the ice front and has the strongest outflow (Section 1.2). We follow the published results for selecting endpoints in this region (Table 2.1). The choice of endpoints will be discussed further in section 2.4.

	mCDW	**WW**	**MW**	υ	W
Potential Temperature (°C)	1.18	-1.8	-90.8	1	2732
Salinity	34.7	34	0	0.5	787
Dissolved Oxygen (ml kg^{-1})	4.18	6.83	28.5	5	35.6

Table 2.1: Endpoints used by Nakayama et al. *(2013) for mCDW, WW and MW in the Amundsen Sea. Units are kept identical to those used in the paper to avoid conversion errors. Uncertainties and consequential weighting values were estimated for each parameter.*

The resulting meltwater fractions calculated from the ESM can be seen in Figure 2.3, below the figure from Nakayama *et al.* (2013) that uses the Jenkins (1999) method (referred to in section 2.2.2 in this chapter as the composite tracer method). The coloured lines represent the same meltwater calculation method in both the

Nakayama *et al.* (2013) results (upper panels) and the results obtained in this study (lower panels). All of these lines are near-identical between the two studies, confirming the comments made in section 2.2.2 about the composite tracer method being equivalent to the ESM. The average meltwater fraction (equation 2.14) is plotted as a black line in all plots from this study for comparison purposes. In this particular case, the average meltwater fraction follows the $c(O)_2$-S meltwater fraction closely, with the θ-S and $c(O_2)$-θ lines (blue and red respectively) diverging from the average line in almost equal amounts at the surface.

A similar exercise can be undertaken for OMPA, with this analysis technique also using a weighting matrix. As outlined in section 2.1.3, we can use the spread in the end-points provided in Table 2.1, and estimate uncertainties in those endpoints (also shown in Table 2.1). Using this, OMPA gives meltwater fractions (purple lines in all plots in Figure 2.3). Similarly to the ESM meltwater fractions, the OMPA fractions are near-identical at depth but diverge from the average meltwater fraction at the surface.

This divergence between different methods that is observed at the surface is due to the water mass transformation processes that occur here: mainly atmospheric-oceanic exchange of temperature, freshwater and gases, and biological activity affecting dissolved oxygen concentrations. In previous studies using the ESM, surface values (above 150-200 m) have been ignored for this reason. However, in many OMPA studies, this surface exchange is included as an additional water mass. Surface exchange is not included in this study, as there are large uncertainties in the temperature and salinity endpoints resulting from atmospheric fluxes and calculations would only be possible using ESM, which does not allow for weighting of the different variables.

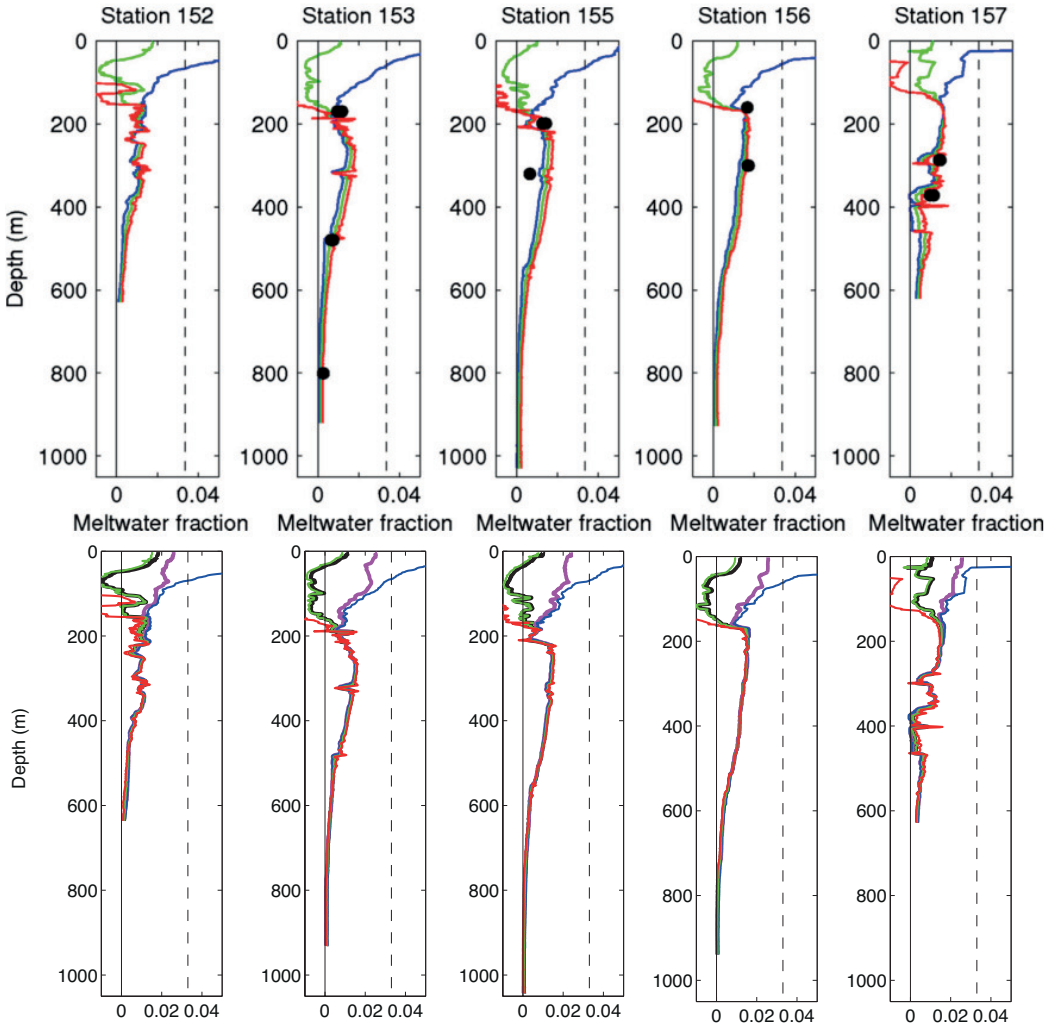

Figure 2.3: Comparison of different meltwater fraction calculation methods from Figure 13 from Nakayama et al. *(2013) in the top 5 panels, and a replication of those calculations below. The meltwater fractions are reported as a fraction of 1, and can be translated to g* kg^{-1}*, as 0.02* $\times 10^3$ *g* kg^{-1}*. The lines are meltwater fractions calculated by: θ-S (blue line), c(O_2)-S (green line), c(O_2)-θ (red line), average from ESM (black line) and OMPA (purple line). Below approximately 200 m depth, these calculation methods are near identical, but show divergence in the surface waters due to atmospheric interaction and biological activity.*

2.4 Endpoint uncertainty

An essential step for water mass identification – regardless of the method chosen – is creating the source water matrix by setting the endpoints. The approximate characteristics of each water mass can often be easily identified from a Θ-S_A plot (e.g. figure 2.1), which is the case for mCDW and WW in the Amundsen Sea. The salinity endpoint for MW is set at zero salinity, as glacial ice is freshwater. However, selecting

the temperature or dissolved oxygen endpoint for MW typically uses extrapolation of a mCDW-MW mixing line defined by a CTD profile taken in the outflow of PIIS. The values gained from this can be compared with far-field ice temperature values and gas analysis of ice cores (e.g. Martinerie *et al.*, 1992).

In the majority of published literature for the Amundsen Sea region (Jenkins, 1999; Nakayama *et al.*, 2013), the effective potential temperature of the ice ($\Theta_i^\star$) is approximately (-90.8 ± 1.2) ° C, calculated based on the heat required to bring the far-field ice temperature (Θ_i) to the melting point (Θ_{fp}) and the latent heat of fusion (L_f, through the phase change of ice to water). This gives

$$\Theta_i^\star = \Theta_{fp} - \frac{L_f}{c_w} - \frac{c_i}{c_w}\ (\Theta_{fp} - \Theta_i), \tag{2.22}$$

as described by Jenkins (1999), but modified from θ to Θ (an almost exact translation), and where c_w and c_i are the specific heat capacities of seawater and ice. The far-field ice temperature (Θ_i) can vary greatly, and has previously been calculated to be between -15 °C and -20 °C (Hellmer *et al.*, 1998; Jenkins, 1999).

To determine the dissolved oxygen concentration for meltwater, measured values from the nearest ice core are used (Byrd ice core, 80 °S, 120 °W; Martinerie *et al.*, 1992). This provides a value of approximately (23.5±1.4) ml l^{-1} (or (1050±70) μmol kg^{-1}) for ice formed at an elevation of 1500 m. Due to variations in elevation, Jenkins and Jacobs (2008) found that a value of 24 to 25 ml l^{-1} represents the meltwater dissolved oxygen content for the George VI Ice Shelf in the Bellingshausen Sea. When the mCDW-MW mixing line is extrapolated to zero salinity in O_2-S_A space, a similar value is obtained for PIIS, which translates to approximately (1125±200) μmol kg^{-1}. Nakayama *et al.* (2013) used an endpoint of 28.5 ml kg^{-1}, which translates to 1273 μmol kg^{-1}, which is within the bounds suggested. This leads to the following characteristics of meltwater in the Amundsen Sea which will be used in this study:

$$\Theta = (-90.8 \pm 1.2)\ ^\circ\ \mathrm{C},$$

$$S_A = (0 \pm 0.1)\ \mathrm{g\ kg^{-1}},$$

$$c(O_2) = (1125 \pm 200)\ \mu\text{mol kg}^{-1}.$$

Obtaining MW endpoints from these theoretical methods and far-field measurements means that the environmental uncertainties associated with the MW endpoint are much higher than those associated with mCDW or WW endpoints. However, there are still some uncertainties associated with the mCDW and WW properties, mainly caused by human error when picking the endpoint on a property-property plot, as well as spatial and temporal variations. To test the effects of these variations in the endpoint, a Monte Carlo simulation is run. This involves many repeated water mass fraction calculations on the simulated observation dataset ($\tilde{\mathbf{b}}$) with the source water matrix ($\mathbf{A}$) slightly perturbed on each iteration. The perturbation for each property of each water type (A_{ij}) is randomly selected from a dataset created with a normal distribution defined by the mean and standard deviation of the typical values used in the Amundsen Sea and the associated uncertainties (see Table 2.2). Each property's uncertainty was based on the variation seen in observational datasets of the mCDW and WW endpoints on property-property plots.

	mCDW	**WW**	**MW**
Conservative Temperature (°**C**)	1.23 ±0.05	-1.7 ±0.05	-90.8 ±1.2
Absolute Salinity (g kg^{-1})	34.88 ±0.01	34.3 ±0.05	0 + 0.1
Dissolved Oxygen (μmol kg^{-1})	187 ±2	300 ±5	1125 ±200

Table 2.2: Endpoints used in Monte Carlo simulations. Presented as the mean value ± standard deviation (or uncertainty) for that particular parameter for each water mass. The dataset was created as a randomly selected normal distribution described by these values.

From $\tilde{\mathbf{b}}$, 92 randomly distributed observations were selected, with each observation run through the OMPA 10,000 times, producing 920,000 perturbed water mass fractions ($\mathbf{x}_{\text{MC}}$). Several different simulations were run, where either all water masses were perturbed, or only one of the three were perturbed (all with OMPA weightings based on the uncertainties in the MW endpoint). The second version of the simulation should allow determination of which water mass contributes the most uncertainty to the overall MW fraction calculated.

In order to assess these results, the differences between the known MW fraction ($\tilde{\mathbf{x}}$) and the simulated MW fraction ($\mathbf{x}_{\mathrm{MC}}$) were plotted as a histogram (Figure 2.4), allowing the distribution of these differences to be observed easily. The standard deviation (σ_k) of the difference between $\tilde{\mathbf{x}}$ and $\mathbf{x}_{\mathrm{MC}}$ represents the uncertainty associated with that water mass (k) for each simulation set up (whether all water masses were perturbed, or just one). When all water masses are perturbed, the uncertainty on the meltwater fraction is ± 2 g kg^{-1}. When individual water masses are perturbed, the shape of the histograms suggest that the majority of the uncertainty may be derived from the WW variability (Figure 2.4f), as this panel shows the widest range of values between -5 g kg^{-1} and 5 g kg^{-1}. However, the standard deviations show that variations in mCDW result in a larger uncertainty (± 1.2 g kg^{-1} compared to ± 0.95 g kg^{-1}; Figure 2.4d). This is linked to the number of $\mathbf{x}_{\mathrm{MC}}$ results that had a greater than 1 unit difference from $\tilde{\mathbf{x}}$, which is also noted on the individual water mass perturbed plots (Figures 2.4d-f). There were few results that fell into this category – at most 3,366 out of 920,000, or 0.3 % of the total mCDW pertubations (Figure 2.4d). When the simulated observations that resulted in these large differences were plotted, they all occurred in locations that fell directly on the mCDW-MW mixing line. The location of these observations in property-property space means that they are liable for the largest variations in meltwater fraction, as they may move in or out of the mixing triangle formed between mCDW-MW-WW.

Typical meltwater fractions in front of PIIS reach 26 g kg^{-1}, so a ± 2 g kg^{-1} uncertainty of this represents approximately an 8 % uncertainty. This relative uncertainty is greater for the lower meltwater fractions – as observations move away from the ice shelf, the uncertainty of ± 2 g kg^{-1} could represent the entire meltwater fraction identified. This means that in order to rely on meltwater fractions produced for the wider Amundsen Sea shelf, we need to reduce the uncertainties in the endpoint values. Until this is achieved, meltwater fractions away from the front of PIIS can only be qualitative.

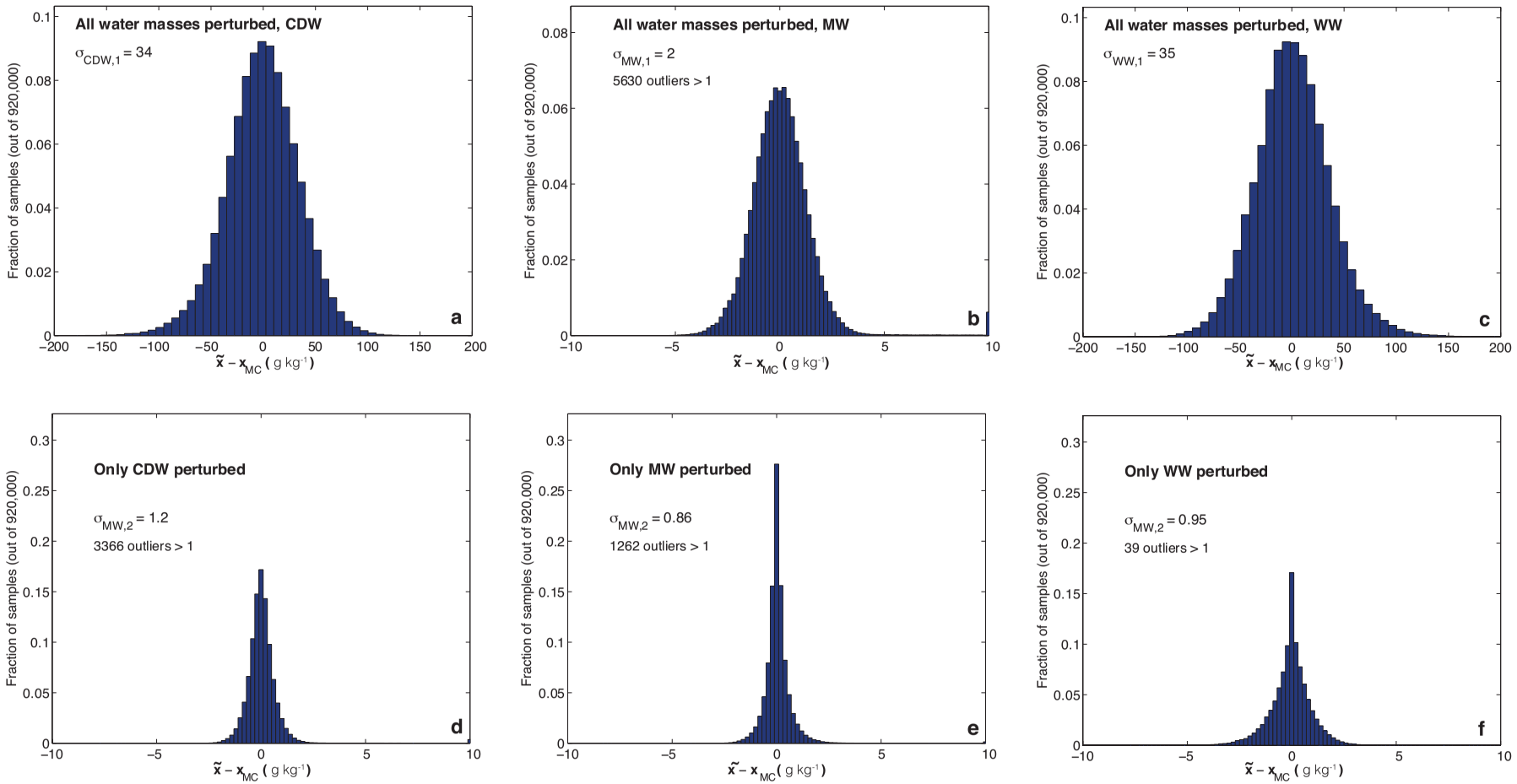

Figure 2.4: Histograms showing the spread in $\tilde{\boldsymbol{x}}$ - $\boldsymbol{x}_{MC}$ *for Monte Carlo simulations of the OMPA method. The top row shows results for simulation run 1, where all endpoints were perturbed: a) CDW fraction, b) MW fraction, and c) WW fraction. The bottom row shows the results for MW fraction when d) only CDW is perturbed, e) only MW is perturbed, and f) only WW is perturbed. All plots show the standard deviation* ($\sigma_{k,n}$)*, where* k *shows the water mass that the fraction refers to and* n *shows the simulation run. For the MW plots (b,d,e,f), the number of outliers (where* $\tilde{\boldsymbol{x}}$ - $\boldsymbol{x}_{MC}$ > 1*) is shown.*

2.5 Conclusion

This chapter looked at the methods to calculate water mass fractions. Due to the number of water masses that we want to identify in the Amundsen Sea, combined with the number of tracers available to be used, Optimum Multi-Parameter Analysis (OMPA) was determined to be the most useful method for this region. Variations between methods mainly occurred in the surface layers where there is strong interaction with the atmosphere affecting heat, freshwater and gas budgets. Weighting the different tracers allowed the more reliable tracers to have a bigger influence on the results. This will be the method used throughout this thesis, with the weightings used established for each case.

An important element to all water mass calculation methods is setting the endpoints. Due to both analytical errors and environmental uncertainties, these endpoints are not definite. Monte Carlo simulations were used to approximate the errors introduced by this variability into the endpoint and showed that meltwater fractions have a standard uncertainty of ± 2 g kg^{-1}. This uncertainty could represent as little as 7.7 % of the calculated meltwater fraction, or could represent the entire meltwater fraction. Due to this, meltwater calculations are most likely only reliable when they are larger than 8 g kg^{-1} (resulting in a 25 % uncertainty). Lower meltwater fractions (≥ 2 g kg^{-1}) should be used as indicators of the presence of meltwater, rather than accurate quantifiable meltwater readings. This shows that whilst these methods are highly uncertain away from the front of PIIS, they are still useful to identify the presence of meltwater – and therefore can be used to identify possible meltwater pathways.

In order to make these estimates more reliable, it is important to collect observations to improve the uncertainties associated with the endpoints. An increase in observations may also lead to identification of other processes that could be affecting water mass characteristics below the surface layer. This will be assessed further in Chapter 3, where observations are collected in the Amundsen Sea between the continental shelf edge and the front of the ice shelf.

Chapter 3

Amundsen Sea Hydrography

3.1 Introduction

The importance of identifying meltwater pathways has been discussed in Chapters 1 and 2, highlighting how the introduction of this lower salinity, lower density water mass to the ocean may have an influence on processes around the Antarctic coastline. Yet it has also been established that the current methods of meltwater fraction calculation are limited by the uncertainties associated with defining the endpoints of the water masses in the Amundsen Sea (Chapter 2). These uncertainties are in part introduced by variability in apparent endpoints across the Amundsen Sea, as can be observed in previous data published from the region (e.g. Nakayama *et al.*, 2013).

In order to understand the uncertainties associated with the different endpoints, and how they come about, it would be useful to know the pattern of ocean circulation across the continental shelf in the Amundsen Sea. This could identify what water masses are mixing under the ice shelf and where mixing with meltwater may occur. However, this requires spatially diverse data collection, and full studies of the region are rare as the Amundsen Sea is notorious for bad sea ice conditions making certain parts of the continental shelf inaccessible. This means that the locations of observations of the area are limited to ice-free zones, resulting in under-studied areas of the

continental shelf.

In the austral summer of 2014, the Ocean2ice research project conducted an oceanographic cruise to the region to study the transport of warm mCDW on shelf and to identify meltwater travelling away from PIIS. These observations will be used to try to understand how the endpoints vary and whether any sub-surface processes may be affecting how the water masses are defined. These processes could include additional water masses mixing in the column or biological activity (respiration or productivity). This chapter will discuss the results from this cruise, focussing on the endpoint variability observed between different regions of the Amundsen Sea, and also between different years, as well as identifying any additional processes that may be affecting the meltwater calculations.

3.2 Data Collection and Processing

The Ocean2ice cruise took place on the *RRS James Clark Ross*, between January and March 2014, with 104 CTD stations in total (Conductivity-Temperature-Depth; Figure 3.1). CTD measurements were collected using two identical Seabird sensors (providing salinity, temperature and pressure), an SBE 43 dissolved oxygen electrode, a fluorometer, beam transmissometer and a PAR (photosynthetically active radiation) sensor. CTD data were processed using Seabird processing software and the CTD sensor showing the best stability of the two was chosen. The preferred CTD sensor was consistent throughout the cruise, except for CTD station 24 where it was frozen on the downcast and so the other CTD sensor was used. Final data files were binned into 2 db (approximately 2 m) intervals. The CTD rosette also held 24 bottles to collect water samples at discrete depth intervals.

Temperature was calibrated using a SBE 35 deep thermometer (at depths where bottles were fired). The differences between the SBE 35 and SBE 911 temperatures were plotted and found to be constant throughout the cruise with no dependence on

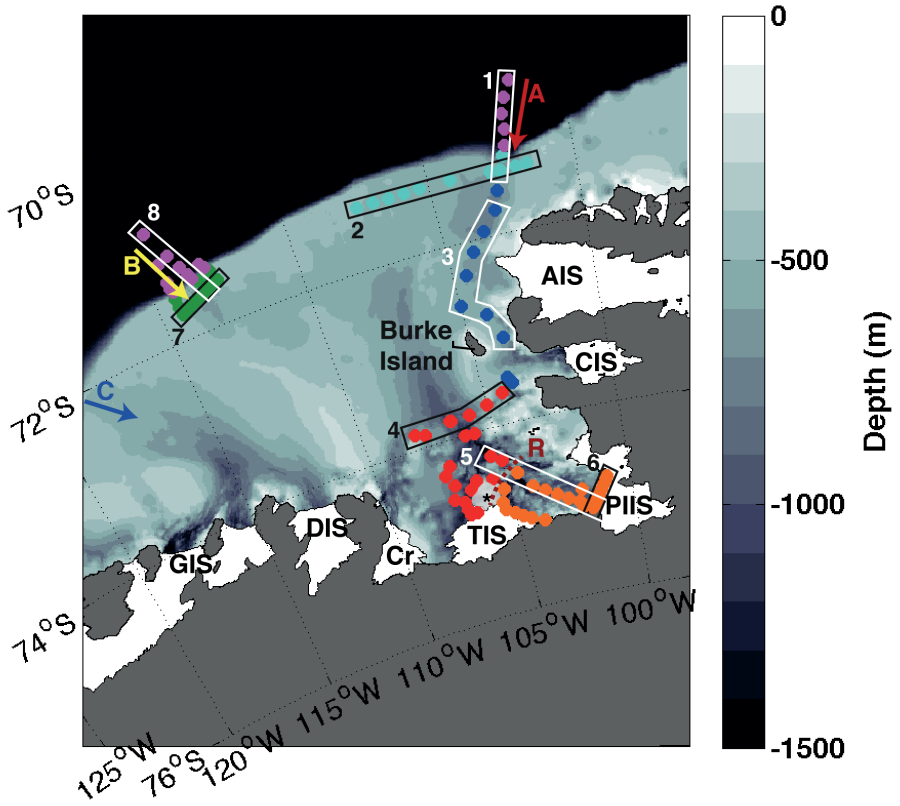

Figure 3.1: Map showing the CTD stations from Ocean2ice, split into characteristic regions. Purple = Off Shelf, Cyan = Shelf Edge (East), Blue = Eastern Channel, Green = Shelf Edge (Central), Red = Outer Pine Island Bay (PIB) and Thwaites Ice Shelf (TIS), and Orange = Inner PIB and Pine Island Ice Shelf (PIIS). The numbers relate to different sections plotted in Figures 3.5 - 3.12, and the letters and arrows show the three main channels into the Amundsen Sea; A = Eastern Channel, B = Central Channel and C = Western Channel. Burke Island is labelled as well as the ridge (R) separating the PIB and PIIS CTD groupings. The asterisk (*) marks an area of fast ice in front of TIS. Local ice shelves are also labelled: Abbot Ice Shelf (AIS), Cosgrove Ice Shelf (CIS), Crosson Ice Shelf (Cr), Dotson Ice Shelf (DIS) and Getz Ice Shelf (GIS).

pressure, temperature, salinity or time. Water samples were collected for analysis of salinity and dissolved oxygen concentrations ($c(O_2)$), using a Guildline Autosal salinometer and automated Winkler titration with photometric endpoint detection on-board the ship. Temperature and practical salinity were converted to conservative temperature (Θ) and absolute salinity (S_A) following The Equation Of State, 2010 (TEOS-10; IOC *et al.*, 2010). Fluorescence (as a measure of chlorophyll *a* concentrations), beam transmission and PAR sensors were not calibrated. The corresponding data are only used in relative terms.

The hydrographic data is analysed using property-property plots (Figures 3.2 and 3.3) and as sections (Figures 3.5 to 3.12). The colour schemes used in these plots follows the colours used in the map shown above (Figure 3.1).

3.3 Water mass characterisation

Three of the water masses on shelf (mCDW, WW and AASW) can be easily identified in the Θ-S_A and c(O_2)-S_A plots that contain all of the Ocean2ice continental shelf data (Figures 3.2-3.3). In addition to these three water masses, in the continental shelf edge sections and property-property plots (Figures 3.2, 3.3, 3.5, 3.12) the two components of CDW can be seen. Upper CDW (UCDW) is the warmest portion of the CDW (over 1.5 °C) and the Lower CDW (LCDW) is as a cooler, saltier, higher oxygenated water mass below the UCDW. The properties of the main three water masses vary spatially across the shelf (Figures 3.5 - 3.12), giving some spread in their exact definition on the property-property plots.

The Amundsen Sea is split into different regions, using similar criteria to Nakayama *et al.* (2013), where regions are separated by differences in maximum temperature at depth (relating to mCDW variations) or differences in the WW salinity or temperature (where the coldest temperature is used as the WW endpoint; Table 3.1). The boundaries of these regions can be affected by the bathymetry of the Amundsen Sea, especially around the front of Thwaites Ice Shelf (TIS) where an underwater ridge extending from underneath TIS out into PIB (ridge R, Figure 3.1) separates the CTD stations here into two different groups.

At the surface is the seasonally warmed and freshened AASW, which is typically around 100 m thick. It is much fresher (33.2 to 34.2 g kg^{-1}) due to sea ice melt, and has a wide range in temperature properties, varying from the local freezing point (-1.8 °C) to around 0.2 °C at its warmest. This variability in temperature is in part due to the temporal changes between the beginning and end of the cruise, when the days were

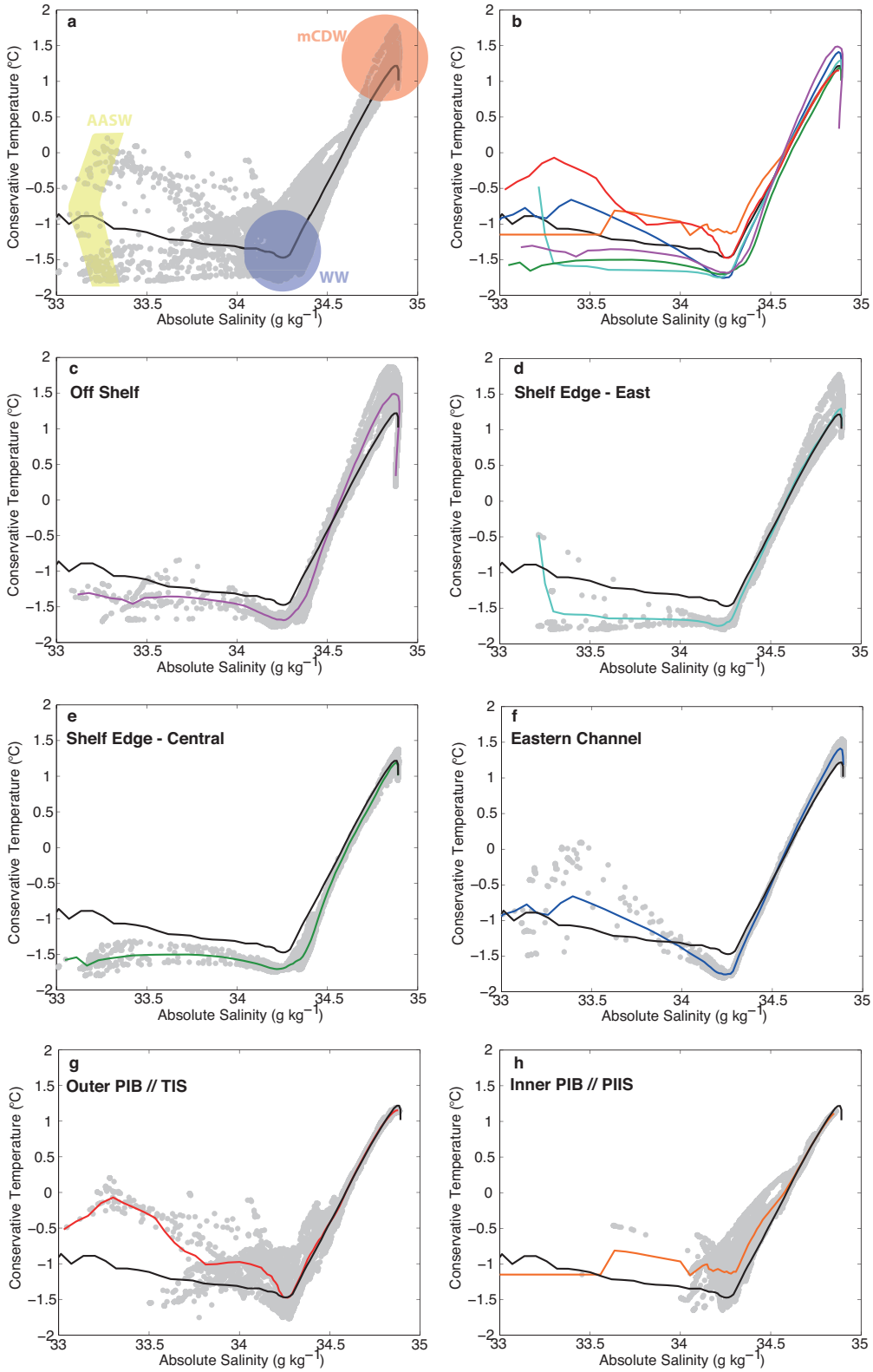

Figure 3.2: Conservative temperature - absolute salinity (Θ-S_A) diagrams for the separate regions in the Amundsen Sea, using Ocean2ice data. a: All data plotted as grey dots with the density-average profile plotted above in black. The main water masses (mCDW, WW and AASW) are highlighted. b: All of the mean profiles for each region, including the overall mean in black. c - h: For each of the separate regions, all of the CTD data from that region are plotted behind the mean profile in grey dots, with the overall mean profile also plotted in black. The coloured line represents the density-averaged values for that region, where the colours follow those shown in Figure 3.1.

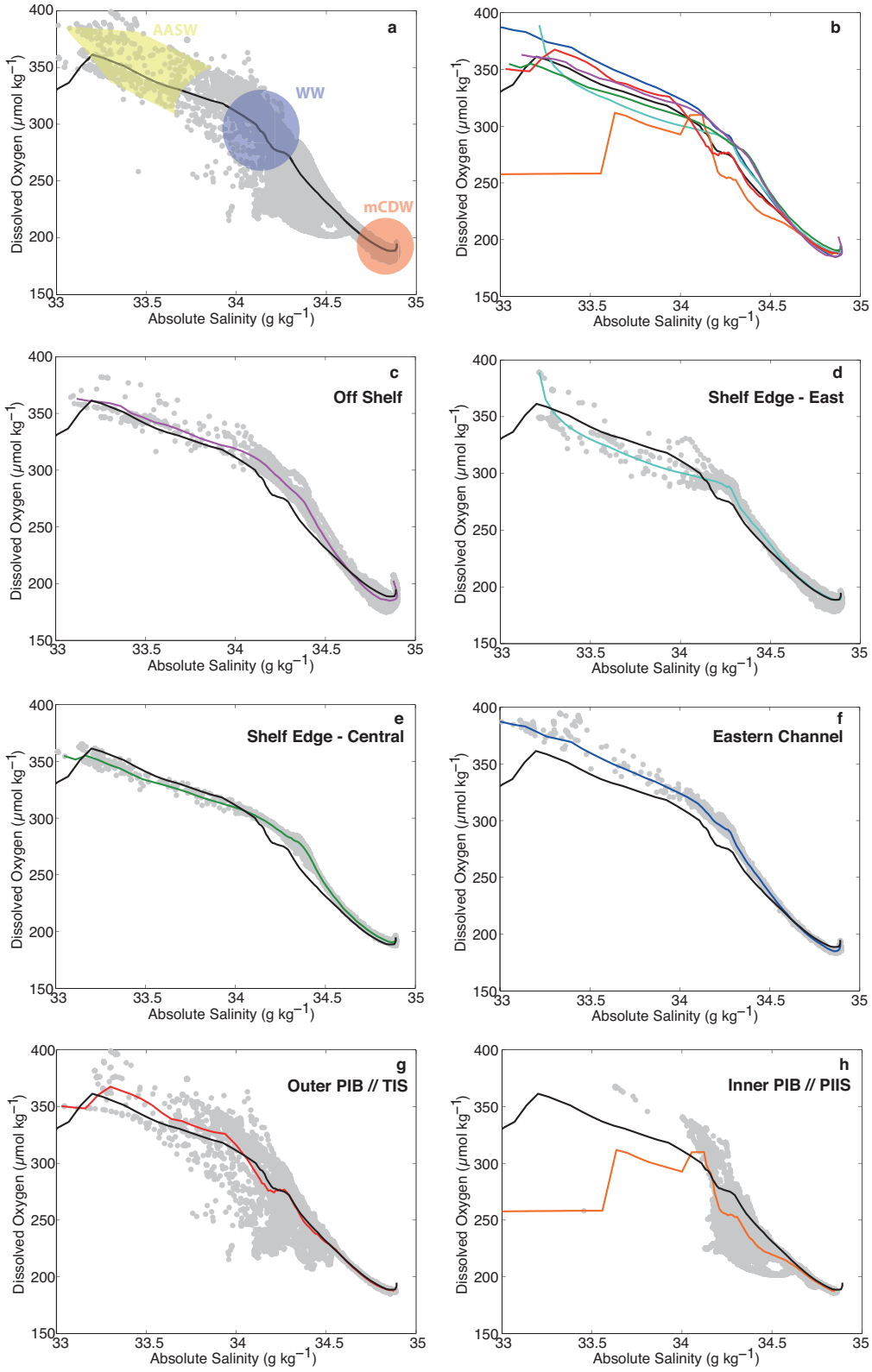

Figure 3.3: Dissolved oxygen - absolute salinity ($c(O_2)$-S_A) diagrams for the separate regions in the Amundsen Sea, using Ocean2ice data. a: All data plotted as grey dots with the density-average profile plotted above in black. The main water masses (mCDW, WW and AASW) are highlighted. b: All of the mean profiles for each region, including the overall mean in black. c - h: For each of the separate regions, all of the CTD data from that region are plotted behind the mean profile in grey dots, with the overall mean profile also plotted in black. The coloured line represents the density-averaged values for that region, where the colours follow those shown in Figure 3.1.

mCDW	Θ (°C)	S_A (g kg^{-1})	c(O_2) (μmol kg^{-1})
Off Shelf	> 1.55	34.89	186
Shelf Edge (East)	1.30	34.9	187
Shelf Edge (Central)	1.21	34.88	191
Eastern Channel	1.41	34.88	186
PIB and TIS	1.15	34.87	187
PIIS	1.13	34.86	187

WW	Θ (°C)	S_A (g kg^{-1})	c(O_2) (μmol kg^{-1})
Off Shelf	-1.67	34.28	288
Shelf Edge (East)	-1.75	34.22	291
Shelf Edge (Central)	-1.68	34.34	282
Eastern Channel	-1.76	34.27	291
PIB and TIS	-1.47	34.27	277
PIIS	-1.14	34.27	256

Table 3.1: Endpoints for mCDW and WW across the eastern Amundsen Sea, split into regions defined by the maximum mCDW temperature or the minimum temperature below the surface (WW). These regions relate to the different coloured CTD stations in Figure 3.1

getting shorter, shifting into austral autumn, and sea ice production was occurring. The dissolved oxygen concentrations are mainly controlled by local biological activity, and are typically super-saturated on the continental shelf (eastern channel and PIB values; Figure 3.4b). The highest values of up to 400 μmol kg^{-1} were recorded to the east of Burke Island (Figure 3.7c). These concentrations of dissolved oxygen are approximately 113 % saturation (c(O_2)$_{sat}$ = 354 μmol kg^{-1}; Figure 3.4a). This biological productivity is reflected by higher chlorophyll *a* concentrations (Figure 3.4d). The lowest dissolved oxygen concentrations (around 340 μmol kg^{-1}; Figure 3.10c) in AASW were measured in front of PIIS, which had significantly under-saturated surface dissolved oxygen concentrations (Figure 3.4b). This was likely due to strong levels of upwelling of low oxygen water emerging from underneath the ice shelf, and minimal biological productivity.

The S_A, Θ and c(O_2) data can also be used to identify the variability in WW properties between the central and eastern channels. WW is formed in winter through air-sea interaction and sea ice formation, and represents the minimum temperature

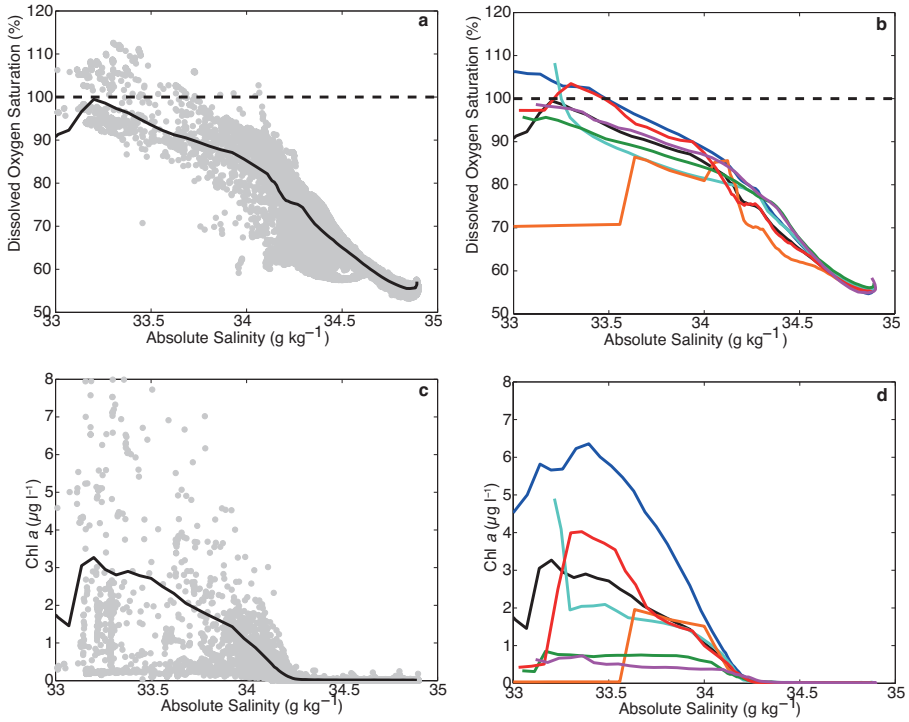

*Figure 3.4: Dissolved oxygen saturation - absolute salinity (a) and (b) and chlorophyll-*a *- absolute salinity (c) and (d) diagrams for the Amundsen Sea, using Ocean2ice data. a and c: All data plotted as grey dots with the mean profile plotted above in black. b and d: All of the mean profiles for each region, including the overall mean in black. The coloured lines represent the density-averaged values for that region, where the colours follow those shown in Figure 3.1.*

below the surface layer, typically seen at about 200 m depth (Figures 3.5-3.12). In the eastern channel it is approximately -1.76 °C with S_A = 34.27 g kg^{-1} and c(O_2) = 291 μmol kg^{-1}. The WW is comparatively warmer (-1.68 °C), slightly fresher (34.23 g kg^{-1}) but equally oxygenated (291 μmol kg^{-1}) at the continental shelf edge of the central channel. This area appears to have a secondary WW feature at approximately 34.34 g kg^{-1} (Θ = -1.68 °C, c(O_2) = 282 μmol kg^{-1}), creating a large spread in the WW in this region (Figure 3.2e and 3.3e). In both Θ-S_A and c(O_2)-S_A space, this secondary WW type forms the endpoint in the mCDW-WW mixing line, and so this will be the WW endpoint used for this region (Table 3.1).

Further south in the outer PIB (as defined by Figure 3.1) and towards PIIS, the WW layer is warmer (-1.14 °C), also becoming more saline with lower oxygen concentrations (as low as 256 μmol kg^{-1}. In section 4 (zonal across PIB, Figure 3.8), the

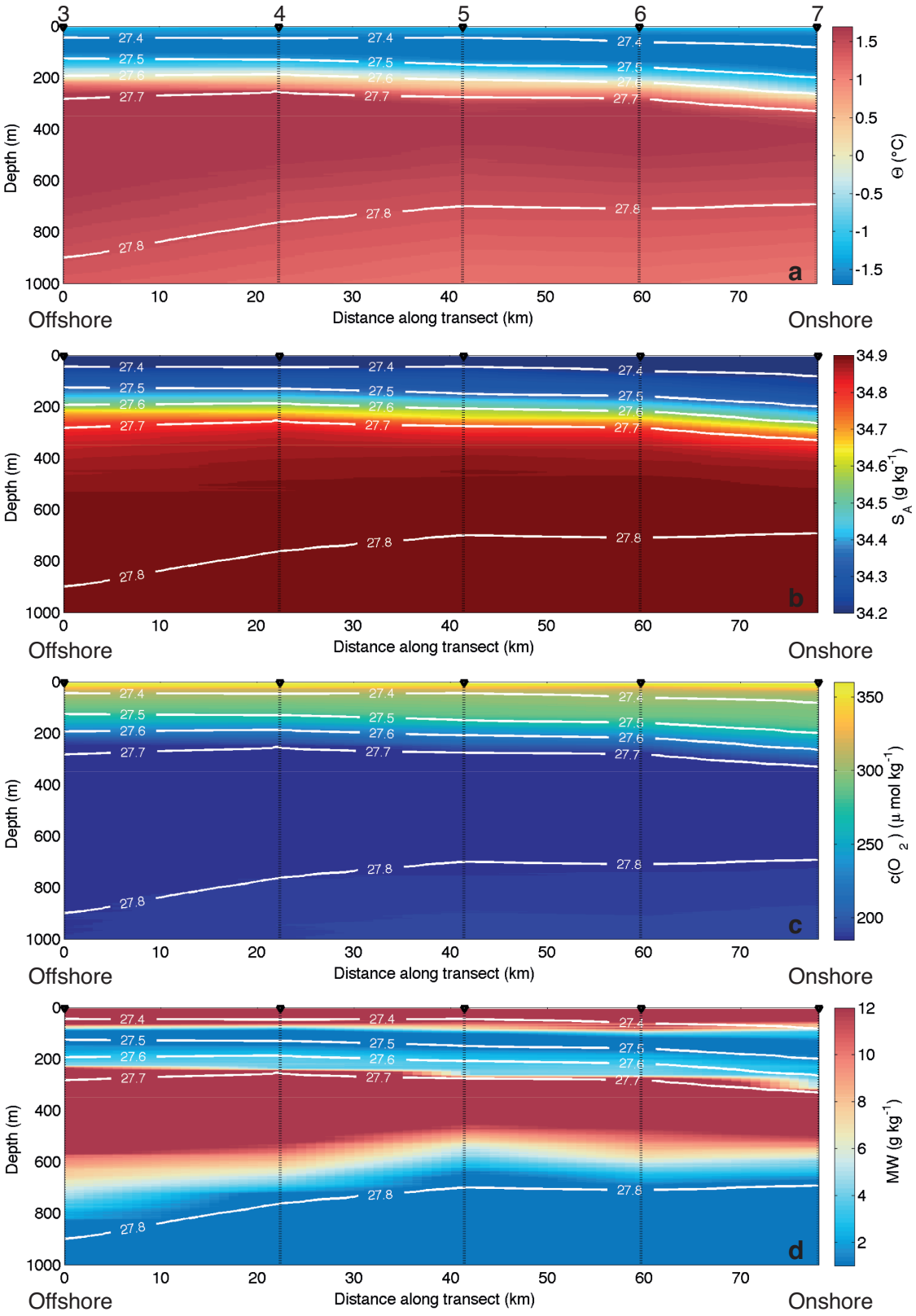

Figure 3.5: Section plots for section 1, oriented meridionally crossing the eastern continental shelf edge (Figure 3.1), showing conservative temperature (Θ, a), absolute salinity (S_A, b), dissolved oxygen concentrations (c(O_2), c) and meltwater fractions (MW, d). Isopycnals are plotted in white between 27.4 - 27.8 kg m^{-3}, and the CTD stations used to make the sections are marked as black lines, with the station numbers marked at the top of panel a. The UCDW (between 300 - 600 m depth) appears as an apparent meltwater signature in (d).

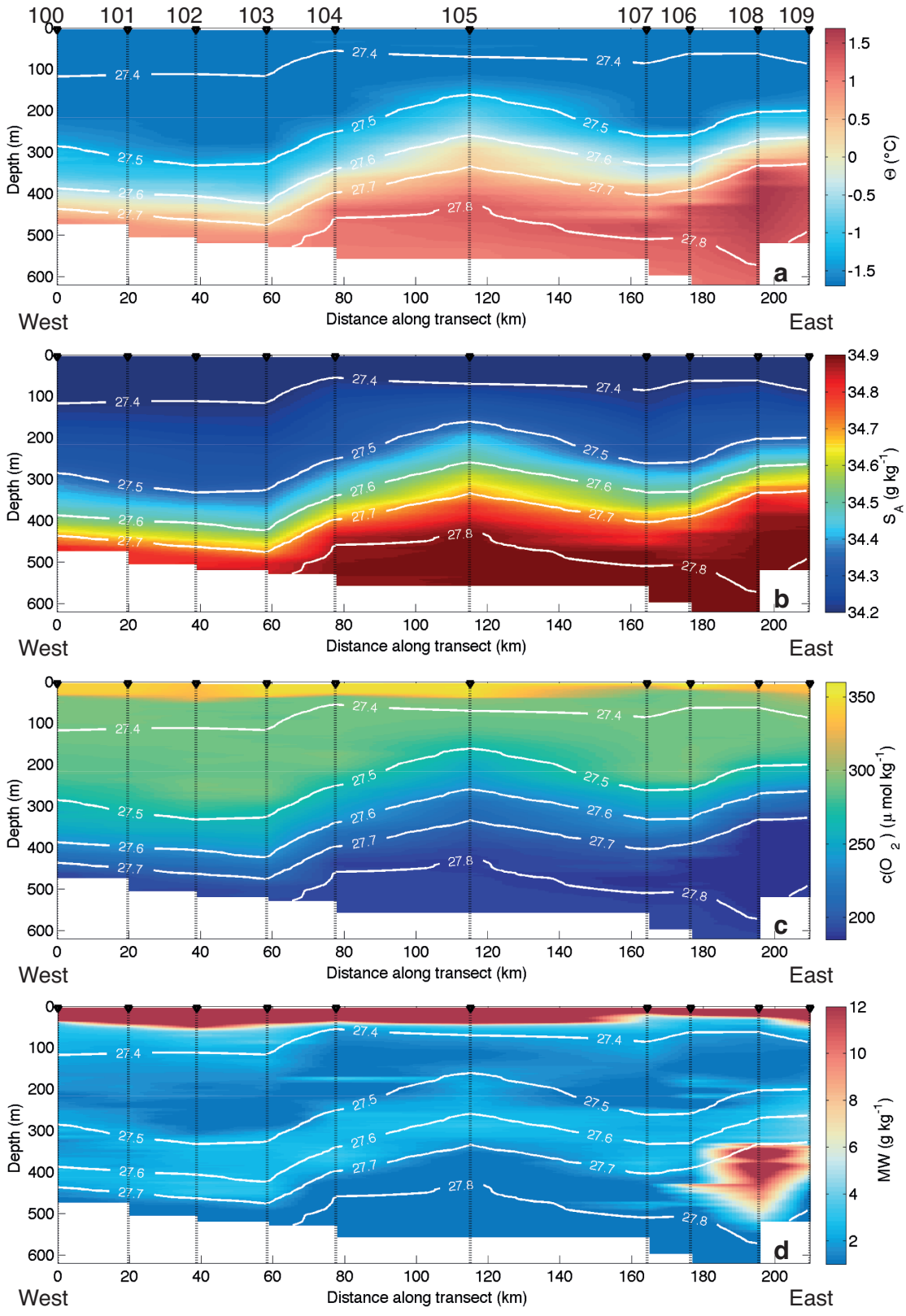

Figure 3.6: Section plots for section 2, oriented zonally across the eastern continental shelf edge (Figure 3.1), showing conservative temperature (Θ, a), absolute salinity (S_A, b), dissolved oxygen concentrations (c(O_2), c) and meltwater fractions (MW, d). Isopycnals are plotted in white between 27.4 - 27.8 kg m^{-3}, and the CTD stations used to make the sections are marked as black lines, with the station numbers marked at the top of panel a. The UCDW can be seen as an apparent meltwater signature between 400 - 500 m at CTD 108 (d).

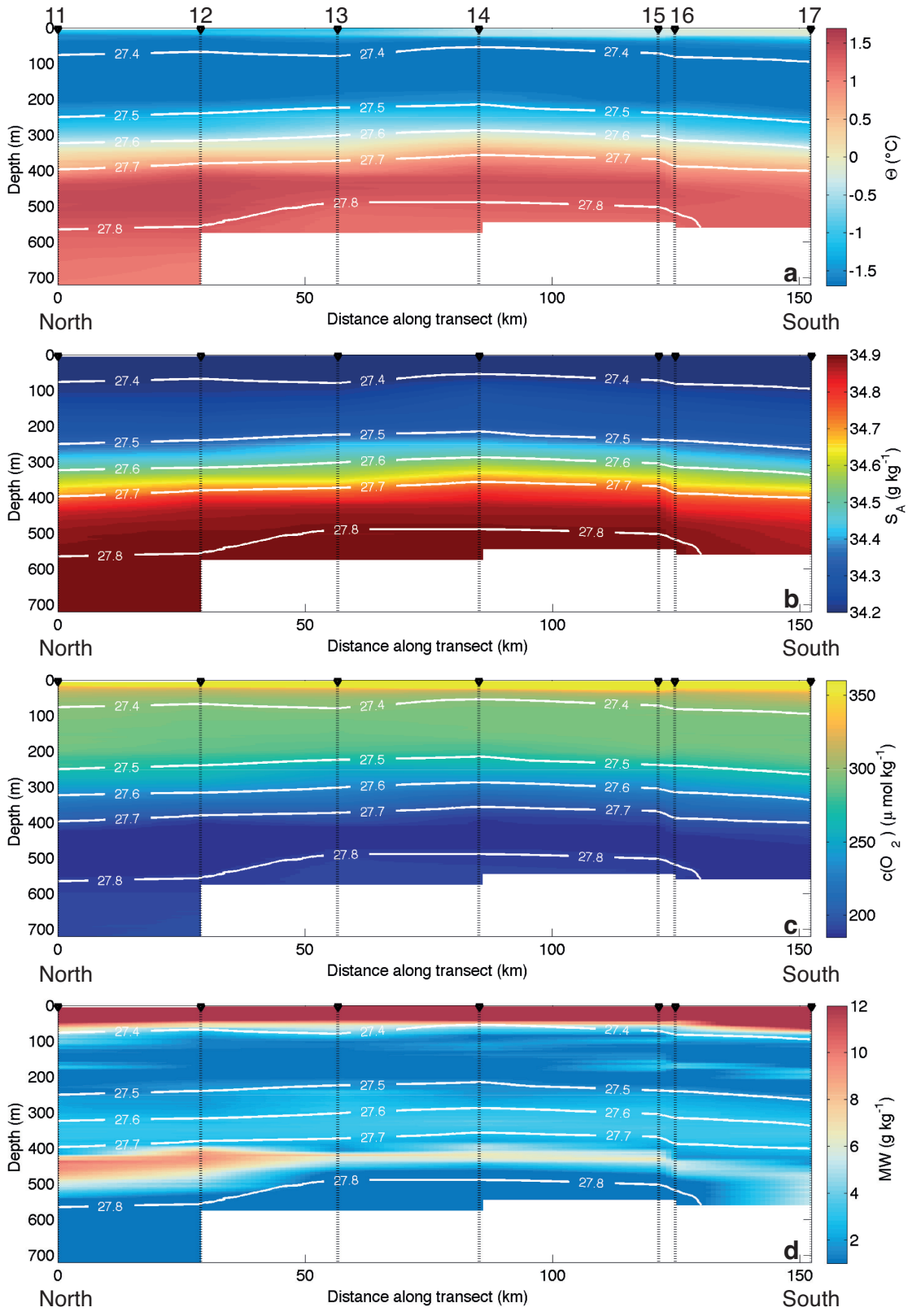

Figure 3.7: Section plots for section 3, oriented meridionally down the eastern channel (Figure 3.1), showing conservative temperature (Θ, a), absolute salinity (S_A, b), dissolved oxygen concentrations (c(O_2), c) and meltwater fractions (MW, d). Isopycnals are plotted in white between 27.4 - 27.8 kg m^{-3}, and the CTD stations used to make the sections are marked as black lines, with the station numbers marked at the top of panel a. The UCDW can be seen as an apparent meltwater signature between 400 - 500 m (d).

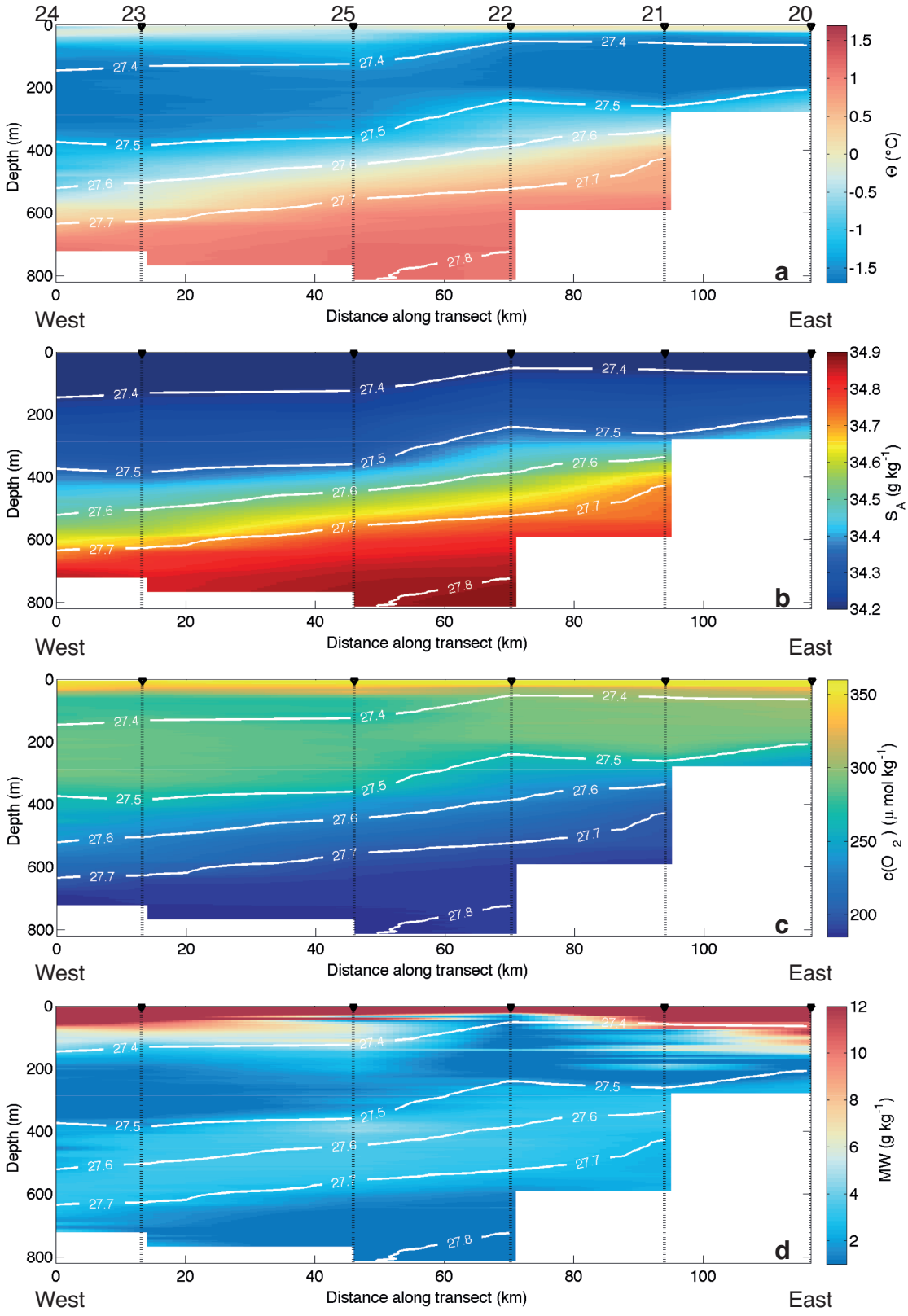

Figure 3.8: Section plots for section 4, oriented zonally across PIB (Figure 3.1), showing conservative temperature (Θ, a), absolute salinity (S_A, b), dissolved oxygen concentrations ($c(O_2)$, c) and meltwater fractions (MW, d). Isopycnals are plotted in white between 27.4 - 27.8 kg m^{-3}, and the CTD stations used to make the sections are marked as black lines, with the station numbers marked at the top of panel a.

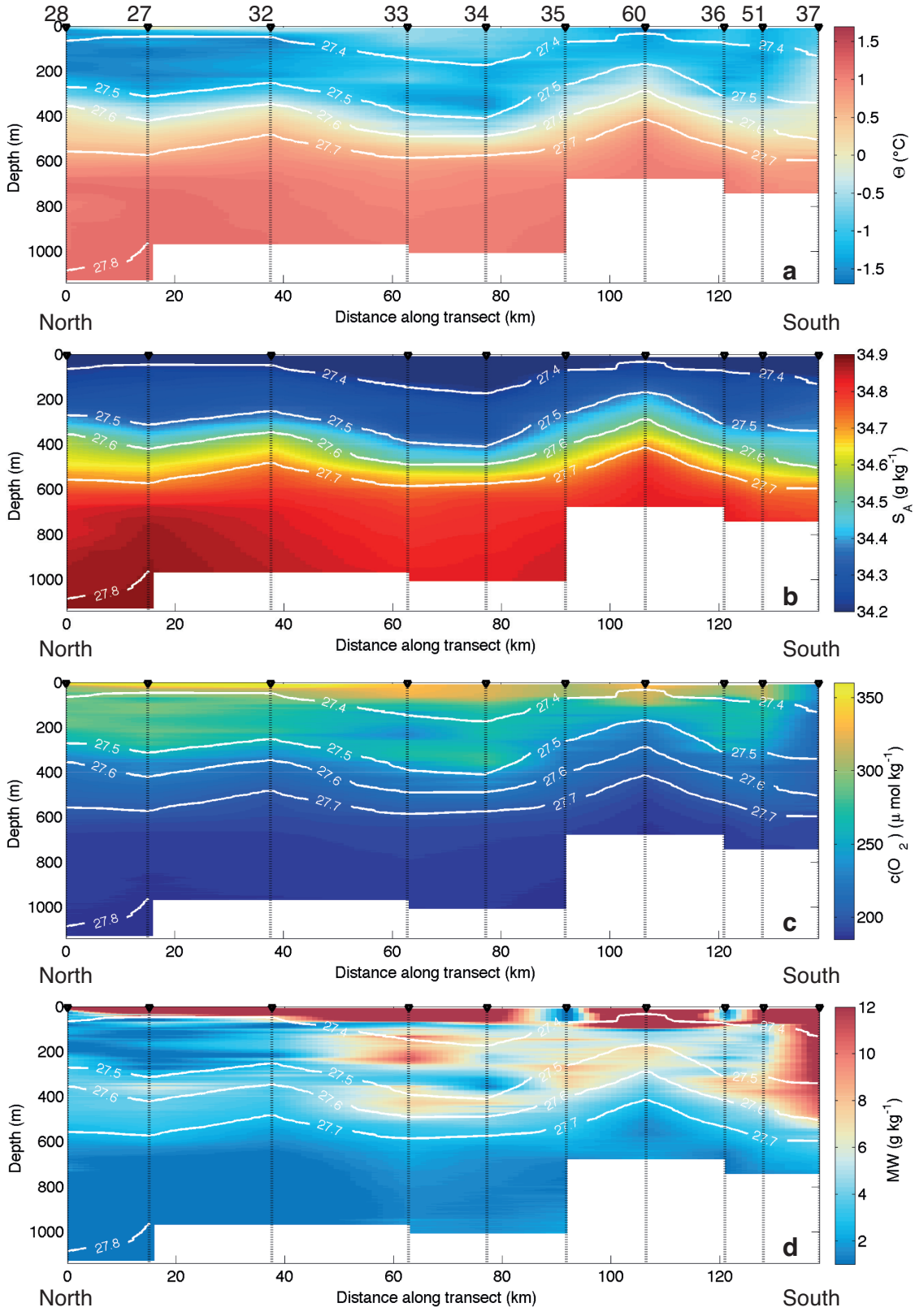

Figure 3.9: Section plots for section 5, oriented meridionally into PIIS (Figure 3.1), showing conservative temperature (Θ, a), absolute salinity (S_A, b), dissolved oxygen concentrations ($c(O_2)$, c) and meltwater fractions (MW, d). Isopycnals are plotted in white between 27.4 - 27.8 kg m^{-3}, and the CTD stations used to make the sections are marked as black lines, with the station numbers marked at the top of panel a.

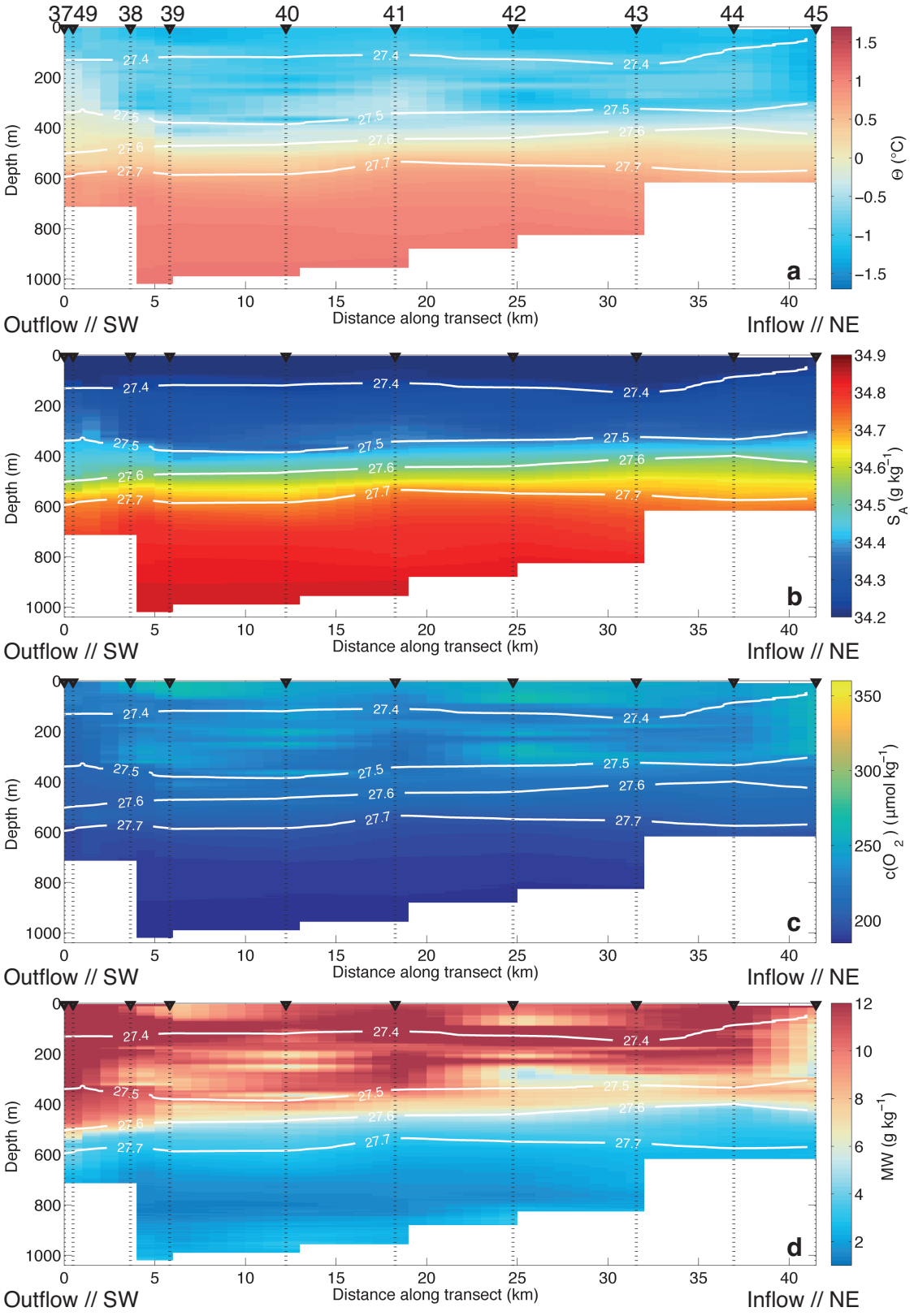

Figure 3.10: Section plots for section 6, oriented southwest-northeast across the front of PIIS (Figure 3.1), showing conservative temperature (Θ, a), absolute salinity (S_A, b), dissolved oxygen concentrations (c(O_2), c) and meltwater fractions (MW, d). Isopycnals are plotted in white between 27.4 - 27.8 kg m^{-3}, and the CTD stations used to make the sections are marked as black lines, with the station numbers marked at the top of panel a.

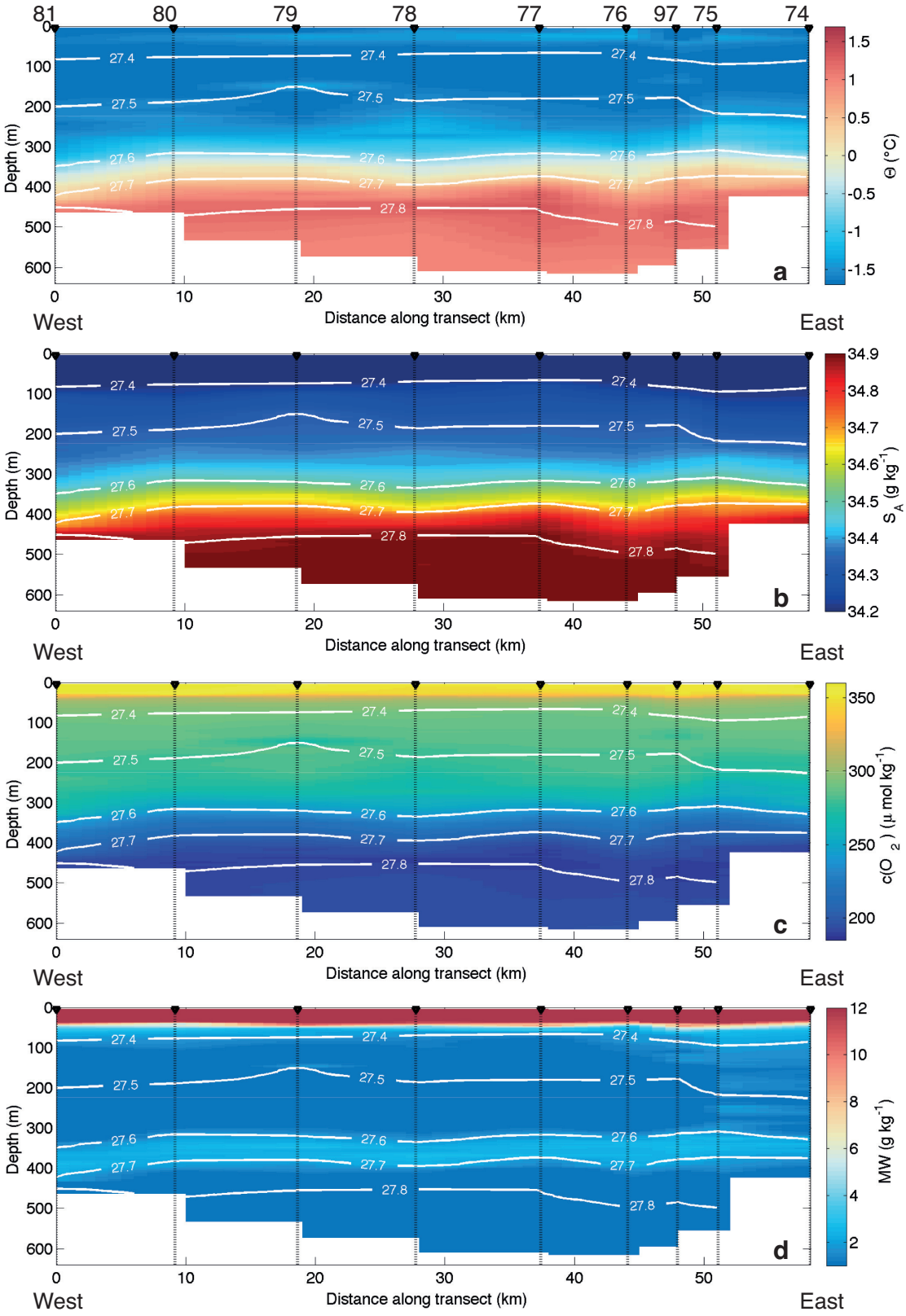

Figure 3.11: Section plots for section 7, oriented zonally across the central continental shelf edge (Figure 3.1), showing conservative temperature (Θ, a), absolute salinity (S_A, b), dissolved oxygen concentrations ($c(O_2)$, c) and meltwater fractions (MW, d). Isopycnals are plotted in white between 27.4 - 27.8 kg m^{-3}, and the CTD stations used to make the sections are marked as black lines, with the station numbers marked at the top of panel a.

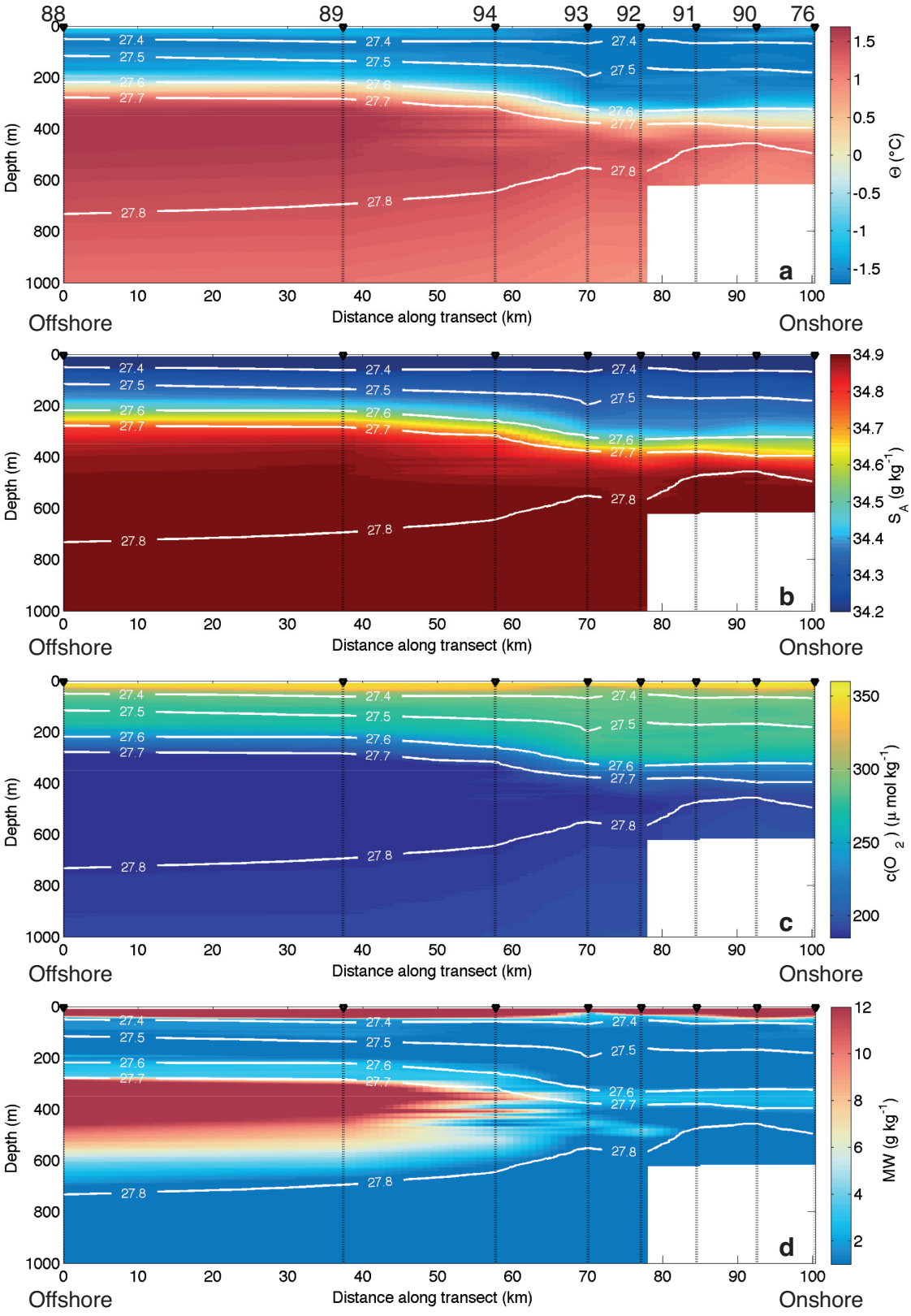

Figure 3.12: Section plots for section 8, oriented meridionally crossing the central continental shelf edge (Figure 3.1), showing conservative temperature (Θ, a), absolute salinity (S_A, b), dissolved oxygen concentrations ($c(O_2)$, c) and meltwater fractions (MW, d). Isopycnals are plotted in white between 27.4 - 27.8 kg m^{-3}, and the CTD stations used to make the sections are marked as black lines, with the station numbers marked at the top of panel a.

depth of the minimum temperature seems to vary greatly across the section. This is in part due to the tilting isopycnals, associated with the geostrophic transport around the Amundsen Sea (Schodlok *et al.*, 2012; Nakayama *et al.*, 2013), but during the sampling for this section there was also a high concentration of icebergs surrounding the ship. These icebergs and bergy bits (small parts of the icebergs that have broken off and are floating in the water nearby) would have contributed warmer fresher water to the surface layers (as the freezing point of freshwater is warmer than that of ocean water). The depth of the iceberg's keel will also influence what depth of the water column is affected, possibly contributing to this variability seen across the section.

The small dome in the thermocline in section 5 is striking (between 80 - 120 km along the section meridional into PIIS, Figure 3.9). This feature is very distinctive in all of the sections, and is associated with the cyclonic gyre that exists in front of PIIS (Jacobs *et al.*, 2011; Schodlok *et al.*, 2012). The CTD stations taken across this feature (35, 60 and 36) show varying effects of this gyre; Station 60 shows the shallowest depth of the isopycnals between 80-120 km along the section. Station 60 was sampled 8 days after Stations 35 and 36, but the section likely shows a synoptic view of the gyre based on previous observations of the gyre in this region(e.g. Jacobs *et al.*, 2011; Thurnherr *et al.*, 2014). Stations 35 and 36 also have relatively more saline and slightly cooler surface layers than those surrounding. This suggests that the more saline water has been brought up from depth and possibly cooled on contact with the atmosphere – these surface waters also have higher dissolved oxygen concentrations than waters of a comparable salinity in stations nearby.

The warmest mCDW (1.3 - 1.5 °C) can be found in the eastern channel and to the east of Burke Island (Figure 3.1), with a cooler mCDW (1.21 °C) in the central channel (Figure 3.2). In both of the cross-shelf (zonal) sections, the mCDW can be seen as a higher temperature, lower oxygen water mass entering onto the shelf on the eastern side of the channels (Figures 3.6 and 3.11). As well as the decrease in temperature of the mCDW between the two channels, there is an increase in the

minimum dissolved oxygen concentration (186 μmol kg^{-1} to 191 μmol kg^{-1}; Figure 3.3). The presence of mCDW on the eastern side of the channels continues in section 4 (zonal across PIB, Figure 3.8), where the top of the mCDW can be seen to be significantly shallower towards the eastern end of the section. The concentration of the mCDW towards the east is largely due to geostrophic currents in the region, travelling southwards on the eastern side of the channels, and northwards on the western flank. Further south, the densest mCDW (σ_θ = 27.81 kg m^{-3}), relating to S_A > 34.89 g kg^{-1}, does not reach PIIS (Figure 3.9). This means that the mCDW signature here is from the slightly shallower waters which are cooler (1.13 °C) and less saline (34.86 g kg^{-1}). Due to fairly constant vertical dissolved oxygen concentrations at depth, the change in c(O_2) is minimal (187 μmol kg^{-1}).

Using the depth of the maximum temperature as the top of the mCDW layer, and the seafloor as the bottom of the layer, the thickness of the mCDW layer (h_{CDW}) for this dataset can be calculated (Table 3.2). In the eastern channel, the mCDW layer thins from 360 m to 100 m as it travels southward past Burke Island, whilst in the centre of the main channel in PIB it reaches thicknesses of 600 m (Table 3.2). In front of PIIS the mCDW layer is only 100 m thick and is cooler than the mCDW layers further north. The thickness of the mCDW may be important in controlling the amount of above freezing-temperature water than can both get under the base of PIIS and over the ridge that crosses the cavity (Jacobs *et al.*, 2011).

	Av. h_{CDW}	**Max h_{CDW}**	**Min h_{CDW}**	**Θ_{CDW} (°C)**
Shelf Edge (East)	200	328	98	1.47
Shelf Edge (Central)	188	264	100	1.21
Eastern Channel	223	362	100	1.37
PIB and TIS	278	664	98	1.15
PIIS	101	114	98	1.13

Table 3.2: mCDW thicknesses (in metres) across the shelf of the Amundsen Sea. The thickness is calculated using the depth of the maximum temperature in the water column, with the mCDW layer reaching from this depth to the seafloor (taken as the bottom of the CTD cast – casts were on average 10 m from the seafloor). CTD Station 8 is removed from the Shelf Edge (east) dataset as it is set slightly off shelf.

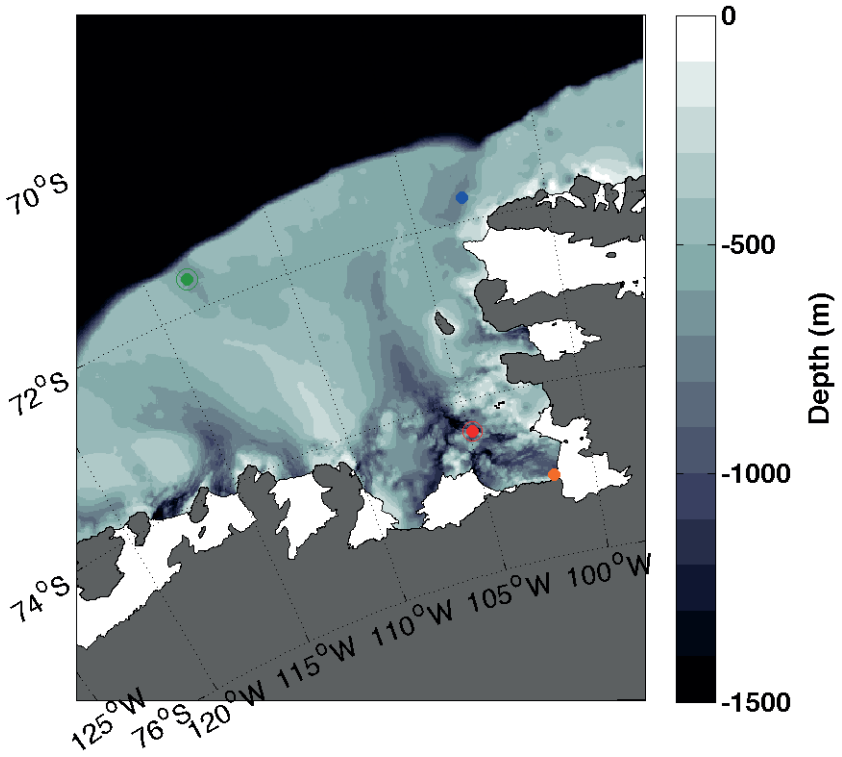

Figure 3.13: Map showing the locations of the repeat historic CTD stations in front of PIIS (orange), in PIB (red), at the central shelf edge (green) and in the eastern channel (blue). The location plotted is the average of all the stations used, and the circle surrounding that point (visible in PIB and at the central shelf edge) represents the distance between stations. The maximum distance between two stations for one location was 12 km, but in the eastern channel the exact same CTD location was sampled in each year, creating the most consistent repeat station.

Some of the locations of the Ocean2ice CTD stations have been sampled in previous years, and so it is possible to compare water mass characteristics between these years. These stations have been indicated in Figure 3.13, showing the average location and spread of the stations being compared. There are repeat stations in front of PIIS, in the central PIB, at the shelf edge of the central channel and just on shelf in the eastern channel. The maximum distance between two CTD stations in one location was 12 km, but on average the distance was less than 5 km. In the eastern channel the same CTD station was sampled in several years, creating a consistent location (distance between stations was less than 1 km). Only the Θ and S_A data will be used as the level of calibration of oxygen data is unknown. In front of PIIS, there are four repeat stations from 1994, 2009, 2010 and 2014 (this study). Whilst

all profiles diverge from the ambient mCDW-WW towards MW values (mCDW-WW mixing line for 2014 plotted on Figure 3.14a), it can be seen that 2009 and 2010 have the warmest mCDW endpoints. These years have been reported to have 'warmer' mCDW on shelf (Schmidtko *et al.*, 2014), and higher melt rates (Jacobs *et al.*, 2011). When the mCDW layer thickness is calculated, using the same method as above, it appears to be relatively constant, with 1994, 2009 and 2014 all between 99 - 103 m. In 2010, the mCDW layer thickness was 177 m and a maximum temperature reaching 1.17 °C in front of PIIS. Whilst the mCDW layer in 2009 was a similar thickness to other years, the maximum temperature was 1.16 °C – higher than those other years. The combination of mCDW temperature and thickness of the layer means that the mCDW in these two years likely carried a considerably higher amount of heat to PIG.

Further away from PIIS, the differences between the years become slightly harder to distinguish, and become affected by WW processes. In PIB (Figure 3.14b), the mCDW-WW mixing line in the 2014 profile can be seen to have cooler temperatures than the previous years, except for the 2000 profile. At the continental shelf edge (Figures 3.14c,d), the biggest variations seem to occur in the WW salinity. This is largely due to the different months of the year that the cruises took place; data collection spread between December to early March in some cases. At the continental shelf edge of the central channel, a spread in the maximum mCDW temperature can also be seen, possibly reflecting the variability that is seen closer to PIG.

Using the data from other research cruises allows a comparison of the endpoints measured in 2014 to those in previous years. These data show that 2014 was not the warmest year recorded, and was most similar to 1994 and 2012. The range in endpoint characteristics can be seen in all years, showing that the variability seen in the endpoints in 2014 is not unique to the Ocean2ice dataset and potentially affects meltwater calculations taken in these other years. This means that the endpoints chosen for use in these calculations will be unique to each dataset.

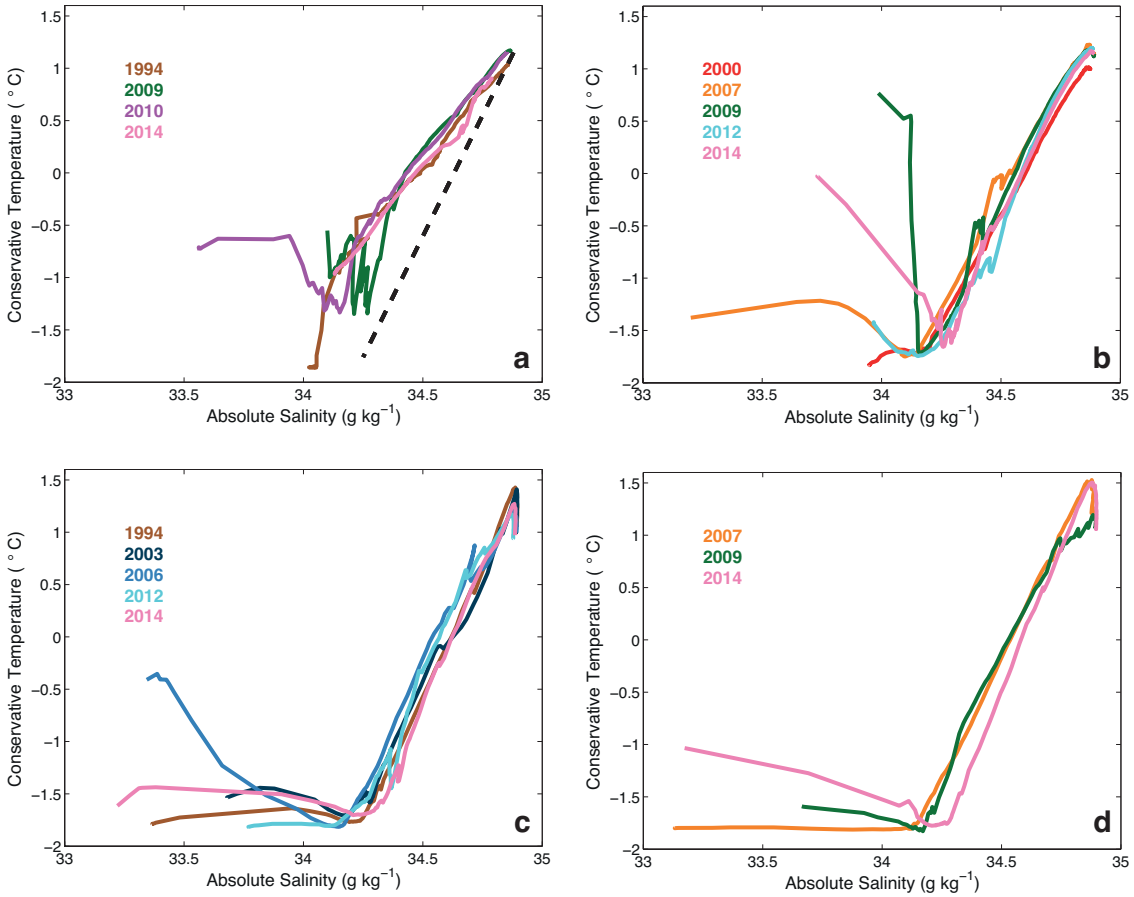

Figure 3.14: Conservative temperature - absolute salinity (Θ-S_A) plots for the four locations of repeat stations shown in Figure 3.13; a) in front of PIIS, b) in PIB, c) in the central channel and d) in the eastern channel. The profiles are coloured by the year the data was collected in with the years labelled on each plot. In the PIIS plot (a), the mCDW-WW mixing line for the Amundsen Sea is plotted on as a black dashed line.

3.4 Variability in endpoints and endpoint selection

As has been discussed in Chapter 2, the uncertainties associated with the WW and mCDW endpoints (Section 2.4) can affect the meltwater fraction by up to ± 2 g kg^{-1}. Variability in the mCDW and WW endpoints was identified across all of the CTD stations, showing that there are considerable environmental uncertainties in both endpoints. In order to understand the uncertainties that this will introduce into the meltwater calculations, it is useful to consider where this variability comes from.

Theoretically, formation of WW is through winter cooling of the surface layers and it represents the remnant of the winter mixed layer. In this region, the winter

mixed layer is typically at the freezing temperature. These waters retain the freezing point temperature and salinity associated with their formation, and could have dissolved oxygen concentrations at or near surface saturation (if they were in contact with the atmosphere). However, the WW endpoint observed displays some variability in temperature, salinity and dissolved oxygen concentration, which is likely due to different surface heat fluxes each year, likely affecting sea ice processes. One area may have more sea ice formation, resulting in a more saline and colder WW endpoint (e.g. eastern channel; Figure 3.2f), whereas another area may experience more sea ice melt, creating a fresher WW (e.g. top layer of the central channel; Figure 3.2e). This inequality in sea ice melt/formation can occur through sea ice transport across the continental shelf: the coastal environment in the eastern channel may encourage conditions favourable to sea ice formation, with winds blowing off the ice shelf then exporting the sea ice from this region creating a net sea ice formation. This variation in sea ice distribution can also be seen in Figure 1.4: along the continental shelf edge there are higher sea ice concentrations than along the eastern channel. Along the continental shelf edge, such as where the central channel CTD stations are located (Figure 3.1), sea ice will be imported from PIB and also from further east in the Bellingshausen Sea, creating a higher potential for net sea ice melt. The deeper, secondary WW type in the central channel is most likely also a product of this sea ice variability; the more saline water mass could have been formed in an especially cold winter, such as the much colder period recorded in 2013 (Webber *et al.*, *in review*).

However, sea ice variability does not account for the warmer and more saline WW layer that occurs in PIB and in front of PIIS (Figure 3.2g,h). This difference in WW is due to the influence of meltwater from PIG, which, due to mixing with mCDW, emerges from under PIIS as a warmer, more saline and lower oxygen water mass than WW. Across all CTD stations, the dissolved oxygen concentrations of WW are lower than surface saturation at the temperature and salinities that they are associated with (Figure 3.4b; surface saturation for Θ = -1.65 °C and S_A = 34.27 g kg^{-1} is 368 μmol

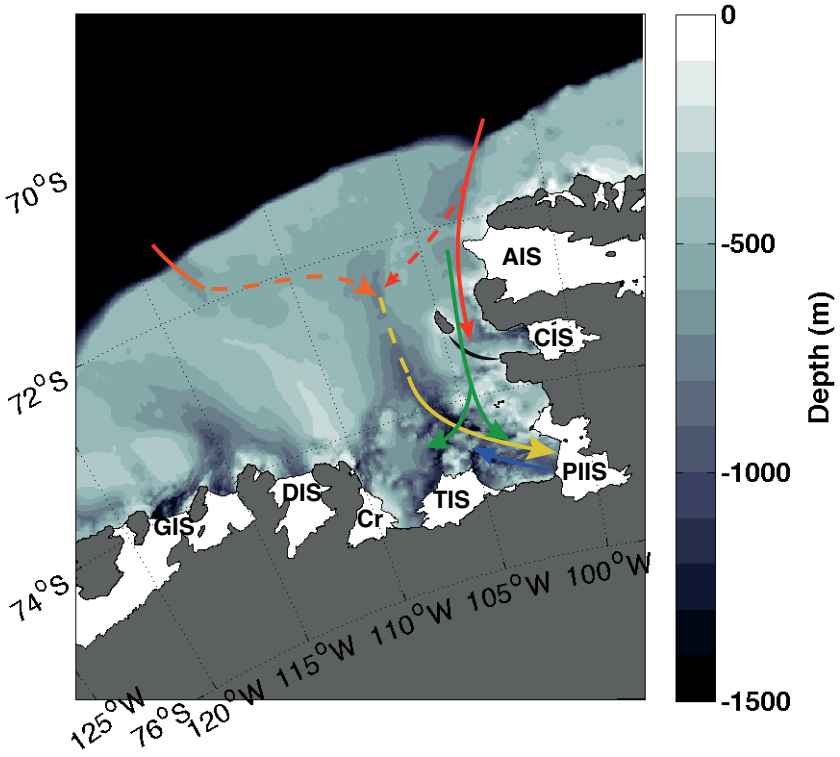

Figure 3.15: Schematic showing inferred water pathways in the eastern Amundsen Sea. The red arrow shows the warmest mCDW comes on shelf in the eastern channel, but is likely blocked by a sill (black bracket) from reaching PIIS. Some of the warmest mCDW mixes with the slighty cooler central channel mCDW (orange arrow), which combine and cool towards PIIS (yellow arrow). The WW in the eastern channel and PIB have similar properties, suggesting a link between these locations (green arrow). The outflow from PIIS is on the western edge, and will contain a mixture of MW and mCDW (blue arrow). The dotted portions of the arrows are where no data was collected in 2014, but previous model studies suggest these pathways (e.g. Schodlok et al.*, 2012; Nakayama* et al.*, 2013).*

kg^{-1}) . This is likely due to a combination of restriction of atmospheric interaction due to the sea ice formation and biological respiration consuming the oxygen once the WW is below the surface.

The range of possible WW endpoints in salinity is approximately 0.05 g kg^{-1} (Figure 3.2b; Table 3.3), and so for the glacial meltwater calculations the WW endpoint for the eastern channel is used (S_A = 34.27 g kg^{-1}, Θ = -1.76 °C, c(O_2) = 291 μmol kg^{-1}). This is because it shares the same WW salinity endpoint as the WW in PIB and in front of PIIS, but the other properties in this area are likely to have been modified, potentially by meltwater addition (Figure 3.15). This is favoured over the central channel continental shelf edge values due to the large range in possible WW

values there from the secondary WW feature seen.

Variations in mCDW across the shelf are likely to be more related to the bathymetry and the depth of the thermocline at the shelf edge (Jacobs *et al.*, 2011). The eastern channel has the deepest shelf edge bathymetry in the Amundsen Sea, and has a shallower thermocline than the central channel, allowing a thicker mCDW layer on shelf (Figures 3.5 and 3.12). Due to this, the eastern channel is the location of the warmest mCDW that comes on shelf (Figure 3.15). The central channel has a shallower inlet at the continental shelf edge and has a cooler and more oxygenated, but of the same salinity, mCDW. The transition from the warmer off shelf CDW (consisting of LCDW and UCDW) to the on-shelf mCDW can be seen in Figures 3.5 and 3.12. The warmer UCDW is located above the bathymetry of the shelf edge channels, but due to cross-shelf processes this does not simply flow on shelf unimpeded. Due to the deeper bathymetry and shallower thermocline in the eastern channel (Figure 3.5a), the UCDW nearly reaches the shelf, resulting in the higher temperatures here. At the shelf edge of the central channel, however, the LCDW appears to shoal and squeeze out the UCDW, resulting in the cooler mCDW temperatures on-shelf. This is similar to what was observed by Walker *et al.* (2007, 2013) and Assmann *et al.* (2013). Further on shelf, the mCDW signature cools; partly due to the cold WW above it resulting in heat loss, but also due to bathymetry changes preventing the densest (and therefore warmest) waters from progressing further south (Figure 3.15). The densest mCDW is not present in front of PIIS: the mCDW found there is the coolest and least saline across the continental shelf (Figure 3.9). The dissolved oxygen concentrations remain approximately constant, likely due to biological respiration at depth.

In the Amundsen Sea, values for the mCDW endpoint are typically chosen from the average properties on shelf which often reflect the values within PIB (e.g. Nakayama *et al.*, 2013). For these meltwater calculations we shall follow these previous studies, and use the mCDW endpoint from PIB of Θ = 1.15 °C, S_A = 34.87 g kg^{-1}, c(O_2) = 187 μmol kg^{-1} (Table 3.3).

The MW endpoint is the most consistent of all 3 endpoints, but not due to a lack of uncertainties. Instead this endpoint is consistent between studies as it cannot be directly analysed and so must be derived from far-field observations or theoretical calculations, as was described in Chapter 2. Due to this, we retain the standard values for MW of Θ = - (90.8 ±1.2) °C, S_A = (0 ±0.1) g kg^{-1}, c(O_2) = (1125 ±200) μmol kg^{-1} (Table 3.3). As the MW endpoint still contains the largest uncertainties, these will be used when calculating the weightings used in OMPA.

	CDW	**WW**	**MW**	υ	***W***
Θ (°**C**)	1.15	-1.76	-90.8	1.2	2277
S_A (g kg^{-1})	34.87	34.27	0	0.1	3984
c(O_2) (μmol kg^{-1})	187	291	1125	400	661

Table 3.3: Endpoints used throughout this study. Uncertainties (υ) estimated from spread in endpoints on property plots, or errors associated with MW endpoints and used to calculate the weightings (W; Chapter 2).

3.5 Glacial meltwater fractions

Using these endpoints we can calculate the meltwater fractions for the Ocean2ice data (Figures 3.5-3.12d). The meltwater fraction decreases as the distance from the front of PIIS gradually increases. Notable is the apparent high meltwater fraction in the surface layer. The cause for this is apparent from the Θ-S_A diagrams (Figure 3.2): in the summer months, the surface layer is warmed through solar radiation, and freshened by sea ice melt. This combination of warming and freshening results in the properties of the AASW layer moving towards the MW endpoint in mCDW-MW-WW mixing space and appearing as glacial meltwater (Figure 3.16). Increases in temperature and decreases in salinity or dissolved oxygen concentrations will appear as apparent increased glacial meltwater fractions (red arrows; Figure 3.16), whilst the apparent glacial meltwater fraction will decrease for changes to properties in the opposite direction (blue arrows; Figure 3.16).

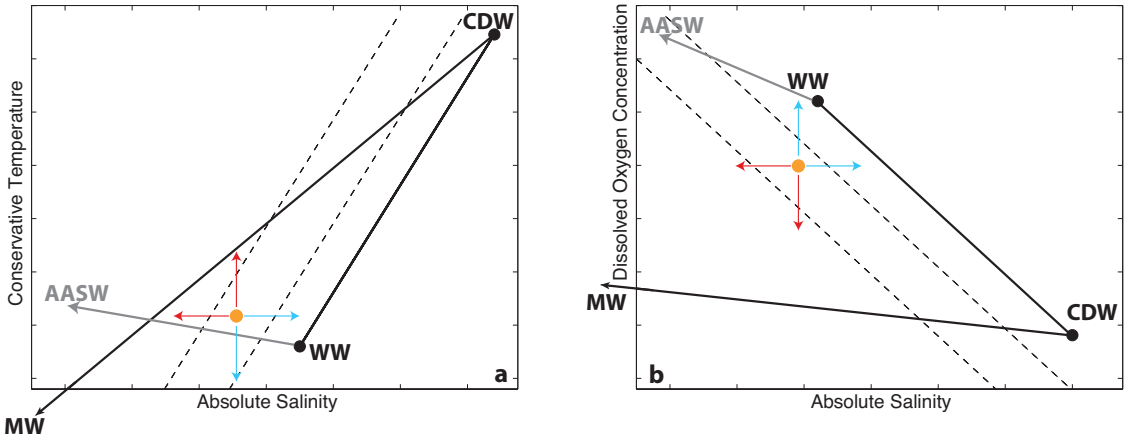

Figure 3.16: Schematic diagrams showing how changes in properties may affect MW fractions for conservative temperature - absolute salinity (a) and dissolved oxygen concentration - absolute salinity (b). CDW, WW and MW mixing lines are shown in black, with the extension between WW and AASW in grey. Isolines of increasing MW fraction are shown as dashed lines, and property changes that cause an increase in MW fraction are shown as red arrows, whilst decreases in MW fraction are shown as blue arrows.

The distribution of glacial meltwater in front of PIIS (Figure 3.10d) is similar to previous years (Jacobs *et al.*, 2011; Nakayama *et al.*, 2013); the highest concentrations on the southern edge of PIIS (where the outflow is observed), and the lowest concentrations on the northern edge. It occurs at depths of 500 m or shallower, which is due to the depth of PIIS (the ice shelf extends down to about 400 m; Jenkins *et al.*, 2010). When the meltwater flows out from underneath the ice shelf it mixes with surrounding water (Naveira-Garabato *et al.*, *submitted*). At the surface the meltwater signature is consistently high in front of PIIS (Figure 3.10d), except in two locations at approximately 6 and 25 km from the outflow (0 km) where it displays a less concentrated signature (discussed in Section 3.7).

Further from PIIS along the meridional section (Figure 3.9d), the meltwater appears in patches along the 27.5-27.7 kg m^{-3} isopycnal. Around the dome caused by the larger cyclonic eddy structure at around 60 km, there are two distinct lower concentrations of MW at the surface. This is likely due to the more saline water mass observed at the surface (compared to adjacent surface waters), as the more saline component combined with the cooler temperature and higher oxygen concentration

(from atmospheric interaction) will reduce the apparent MW fraction (Figure 3.16). Across PIB there appears to be a distinct meltwater signature between 100 - 200 m (zonal section across PIB; Figure 3.8d), most likely linked to the high concentration of icebergs that were present in this area. However, due to atmospheric interaction affecting the apparent MW signature in the top 150 m, these signatures are ignored.

In order to identify meltwater pathways, the meltwater calculation needs to be reliable at the continental shelf edge of the Amundsen Sea. In both of the meridional cross-shelf sections (Figures 3.5d and 3.12d) and the zonal cross-shelf section across the eastern channel (Figure 3.6d), the warm core of the UCDW appears as a distinct apparent MW signature, and the tongue of this warm water that gets on shelf in the eastern channel can be seen spreading southwards and eventually dissipating (Figure 3.7d). This apparent meltwater signature caused by the UCDW and its 'tongue' can be explained by taking into account the much warmer endpoint of mCDW in this area of the Amundsen Sea. As OMPA is being used for the MW calculations, the fractions calculated are constrained by a non-negativity condition, which results in the OMPA 'correcting' the fractions when they become negative. In the eastern channel, the warmer mCDW (derived from the UCDW) lies on the 'negative CDW' fraction (but 'positive MW' fraction) side of the mCDW-WW and mCDW-MW mixing lines, and by correcting this the warmer mCDW appears as a high MW fraction. This is an artefact that needs to be removed.

To remove this, the endpoints from the eastern channel (Table 3.1) will need to be applied to the eastern region of the Amundsen Sea to allow for the different ambient mixing line between mCDW and WW. The resulting meltwater fractions can be seen in Figure 3.17b, and can be compared to the original meltwater fractions (Figure 3.17a). This correction removes the tongue except for the segment to the north of the shelf edge, where the maximum temperature is greater than the mean value for the eastern channel (and the mCDW endpoint used). This highlights that the same endpoints are not suitable for all areas of the Amundsen Sea.

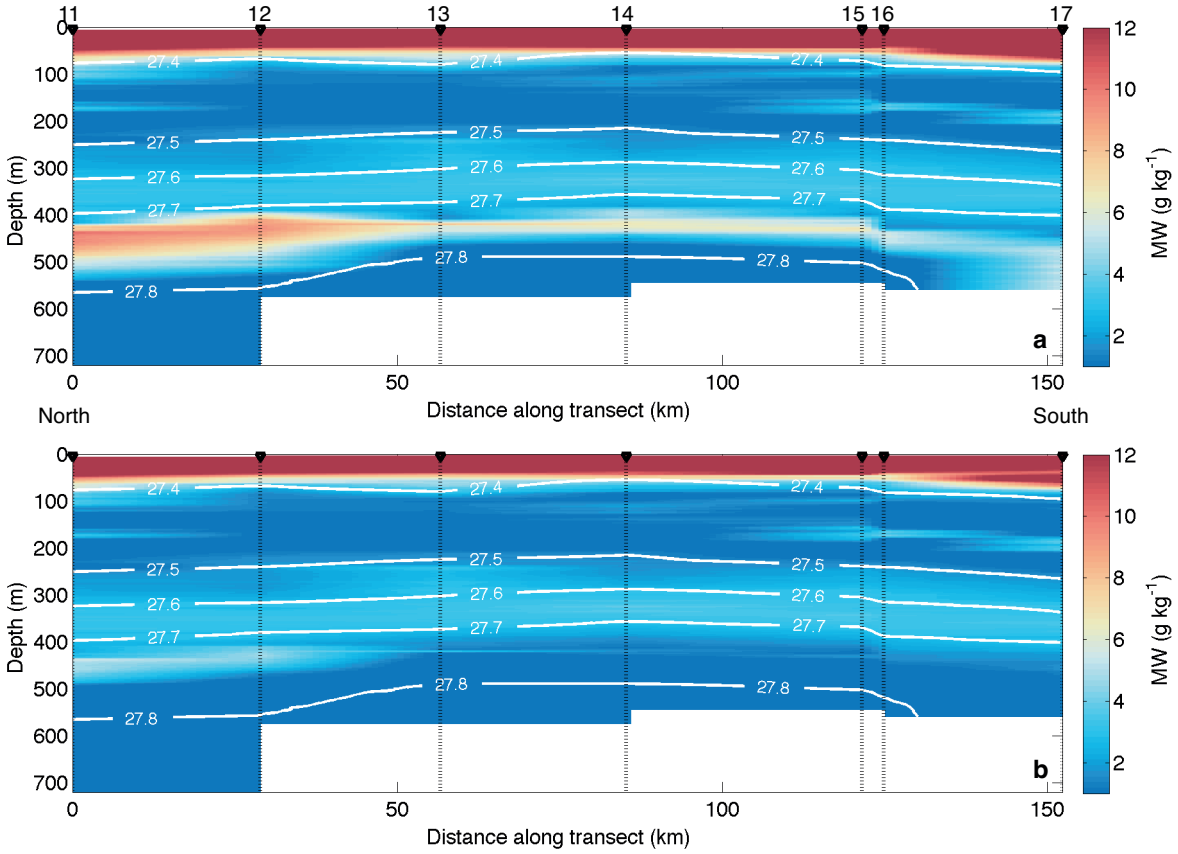

Figure 3.17: Section plots for section 3 (meridional eastern channel), showing MW fraction calculated using mCDW endpoints of (a) Θ = 1.15 °C, S_A = 34.88 g kg^{-1}, c(O_2) = 187 µmol kg^{-3} and (b) Θ = 1.5 °C, S_A = 34.88 g kg^{-1}, c(O_2) = 186 µmol kg^{-3} to remove the effect caused by the UCDW tongue at depth on the calculated MW fraction.

Higher in the water column in the eastern channel, there appears to be a background presence of meltwater of around 4 g kg^{-1} between 100 - 200 m towards the southern end of the channel (Figure 3.17b). Whilst the outflow circulation is thought to be on the western side of the Amundsen Sea and along the coast (Nakayama *et al.*, 2014), there are many ice shelves along this eastern channel, including the Abbott Ice Shelf (AIS; Figure 3.1). This meltwater signature observed in the upper water column could be meltwater from these ice shelves.

Across all of the sections (Figures 3.5-3.12d), there is an apparent meltwater 'plume' between the 27.5 - 27.7 kg m^{-3} isopycnals, which occurs at approximately 400 m depth. The correction applied to the eastern channel meltwater calculation also

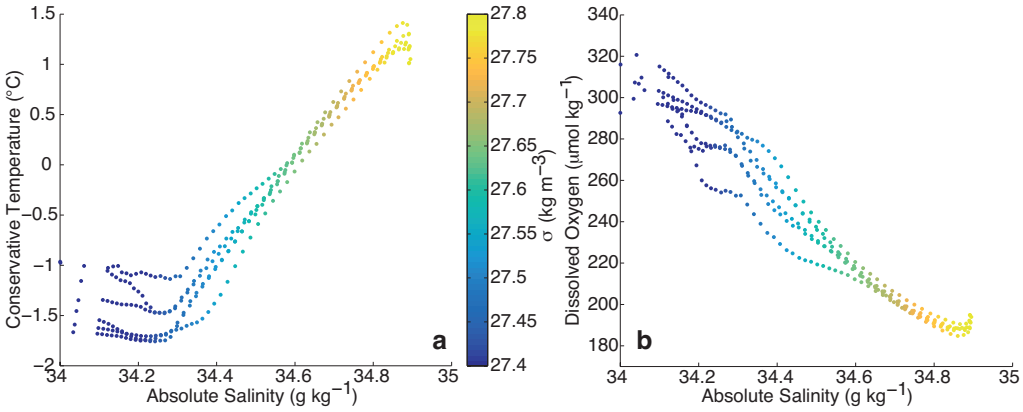

Figure 3.18: Conservative temperature - absolute salinity (a) and dissolved oxygen - absolute salinity (b) plots of the density-average profiles for each region coloured by σ_θ.

makes this plume more apparent in this region (compare Figures 3.17a and 3.17b). This plume can be identified all the way out to the shelf edge, and, if reliable, could signify a clear route that the meltwater takes after it leaves the ice shelf.

In both the Θ-S_A and c(O_2)-S_A plots (Figures 3.2-3.3, and Figure 3.18), a curvature in the mCDW-WW mixing line can be seen, especially in the c(O_2)-S_A plot. This indicates a movement of the water properties off the ambient mixing line into the mCDW-MW-WW mixing space, which will result in the meltwater signature observed. At the isopycnals where the meltwater plume is located, the profile curves away from the ambient mixing line – significantly so in c(O_2)-S_A space (Figure 3.18). Yet what is notable about this curvature is that it appears to occur in all of the profiles in c(O_2)-S_A space (Figure 3.3), and a large number of the profiles in Θ-S_A space (Figure 3.2). This homogeneity of curvature across all CTD stations suggests that whatever causes this curvature is widespread across the Amundsen Sea. Modelling of the ocean circulation on the shelf indicates that the MW outflow is expected to flow westwards and along the coast after leaving PIIS, so this curvature may not be entirely caused by meltwater (Nakayama *et al.*, 2014).

3.6 Curvature in the mixing line

If this curvature that is observed in the property-property plots is not caused by meltwater, then some other process must be occurring in the subsurface and causing inaccuracies in the meltwater calculations. If the entire curvature is not due to meltwater, then it can be assumed that this other process contributes up to 4 g kg^{-1} uncertainty into the meltwater fraction calculations, as this is the maximum MW fraction observed in the sections at the depth concerned (Figures 3.5-3.12d). In order to understand what process could be providing an excess of heat for a given salinity (and loss of dissolved oxygen concentrations) in order to cause this curvature, the curvature must be quantified.

3.6.1 Quantifying the curvature

Quantifying the curvature by equalising the different properties is important, as the difference in the range in values for each property is significant. This range in values could cause the curvature to look greater in $c(O_2)$-S_A space than Θ-S_A space, as $c(O_2)$ has a larger range than Θ. Therefore the properties are normalised to range between 0 and 1 (equation 3.1). The area between the linear mixing line (mCDW-WW) for each region and the curve formed by the data can now be used as a parameter to assess the level of curvature (Figure 3.19). The magnitude of this area can be seen to change between the different regions and different properties, despite the normalisation (values $\times 10^{-3}$; Figures 3.20-3.21).

$$\mathrm{norm}(\Theta) = \frac{\Theta - \Theta_{\mathrm{min}}}{\Theta_{\mathrm{max}} - \Theta_{\mathrm{min}}}. \tag{3.1}$$

The curvature in Θ-S_A space is negligible at the eastern continental shelf edge and directly in front of PIIS (with the average line for those regions crossing to both sides of the linear mCDW-WW mixing line), and is relatively small in the eastern channel and in PIB ($< 1.8 \times 10^{-3}$; Figure 3.20). However, at the central shelf edge,

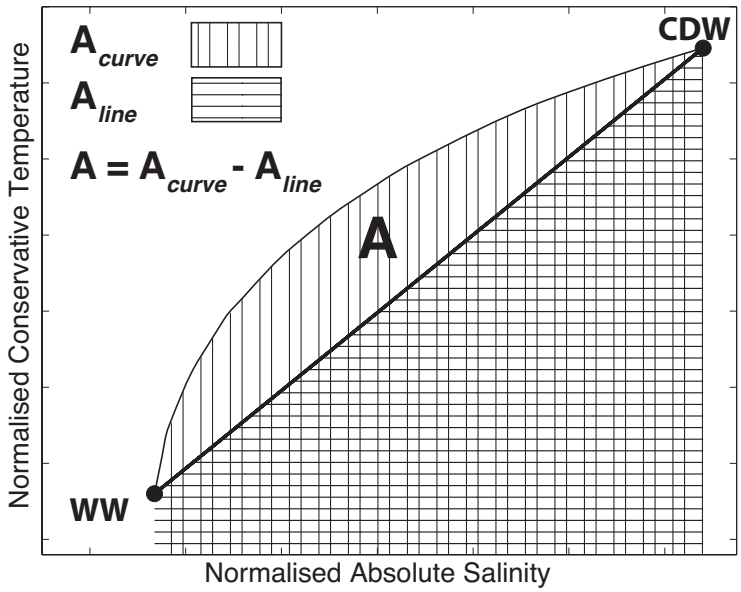

Figure 3.19: Schematic diagram to show how the area between the ambient mixing line and the curve formed by the data is calculated. In normalised conservative temperature - normalised absolute salinity space, the area (A) is equal to the area of the curve (A_{curve}) minus the area of the line (A_{line}). In normalised dissolved oxygen concentration - absolute salinity space, the curvature is in the opposite direction, so here the area (A) is equal to the area of the line (A_{line}) minus the area of the curve (A_{curve}).

this curvature becomes more noticeable, and the area under the curve here reaches 2.7×10^{-3}. In comparison, the curvature in c(O_2)-S_A space is apparent in all regions of the Amundsen Sea, and relatively homogeneous (approximately 3.5×10^{-3}; Figure 3.21). It is greatest in the eastern channel (4.53×10^{-3}).

This spatial variability suggests that there are possibly two processes causing the curvature. The first process affects all three properties and is greatest at the central shelf edge, with minimal effect in front of the ice shelf. The second process only appears to affect c(O_2) and is approximately homogeneous across the continental shelf. Due to the spatial variability of the first process (greatest at the shelf edge, minimal in front of PIIS) and the specificity of the second process (only affecting dissolved oxygen), it is unlikely that either of these processes – and therefore the curvature – is caused by meltwater. Alternative hypotheses are important to consider in order to understand what causes this curvature and its effect on the meltwater calculation.

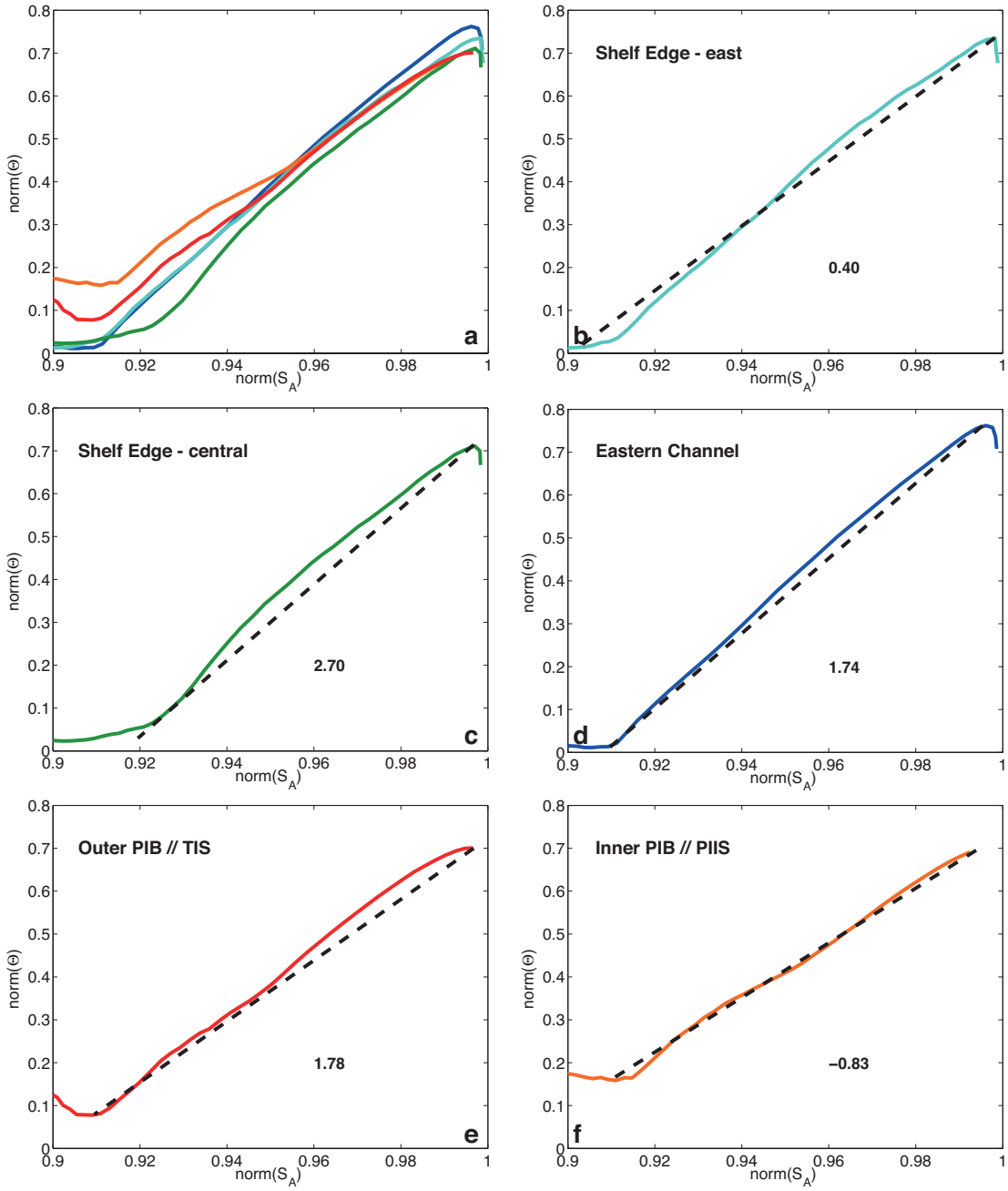

Figure 3.20: Normalised conservative temperature - absolute salinity plots for each region: a) all average profiles from all the regions, b) average profile from the eastern shelf edge region, c) average profile from the central shelf edge region, d) average profile from the eastern channel, e) average profile from PIB and f) average profile from in front of PIIS. On each of the regional plots the local mCDW-WW mixing line is plotted as a black dashed line. The area between the profile and the linear mixing line (A_{curve} - A_{line}) is shown in the lower right quadrant on each plot ($\times 10^{-3}$).

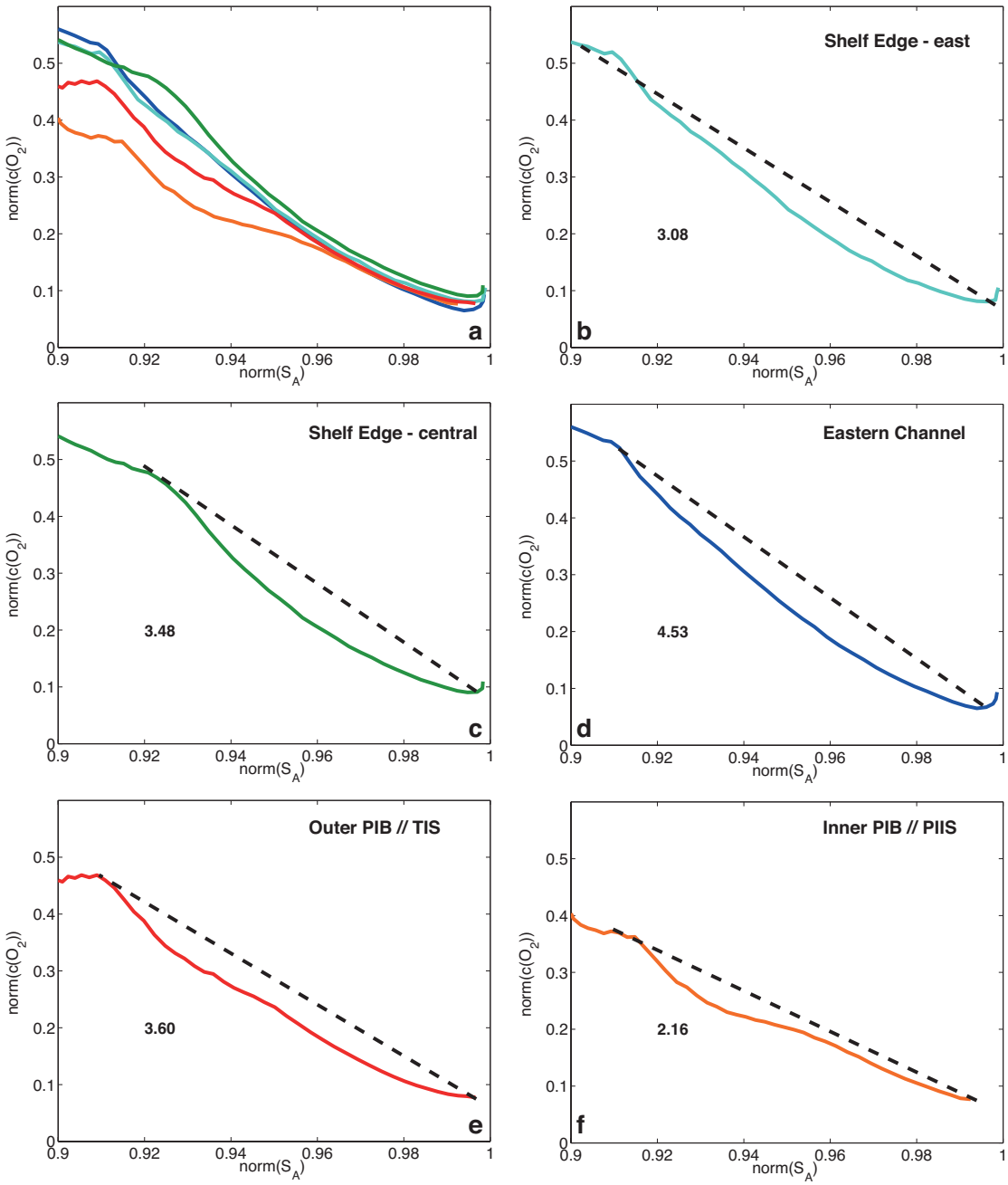

Figure 3.21: Normalised dissolved oxygen - absolute salinity plots for each region: a) all average profiles from all the regions, b) average profile from the eastern shelf edge region, c) average profile from the central shelf edge region, d) average profile from the eastern channel, e) average profile from PIB and f) average profile from in front of PIIS. On each of the regional plots the local mCDW-WW mixing line is plotted as a black dashed line. The area between the profile and the linear mixing line (A_{line} - A_{curve}) is shown in the lower left quadrant on each plot ($\times 10^{-3}$).

The curvature tends towards lower $c(O_2)$, lower S_A and higher Θ, so any processes to be considered must in some way simulate these changes. All subsurface water mass transformations must be linked to physical or biological processes. Working from this foundation, two general processes can be identified: water mass addition and biological activity.

3.6.2 Water Mass Addition

In the Amundsen Sea region there is no deep water formation, limiting the water masses on shelf to the four previously discussed; AASW, WW, mCDW and MW. MW addition has already been considered as a subsurface process in the Amundsen Sea, but as discussed above it cannot account for this curvature observed in the data between mCDW and WW endpoints. So if another water mass has been added to the subsurface water column, what are the possible sources of it?

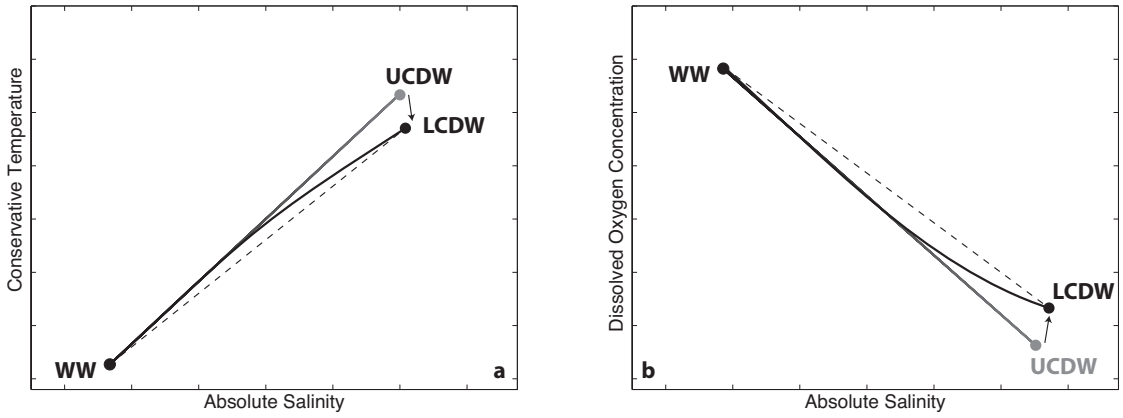

Figure 3.22: Schematic diagram to show how a switch between a WW-UCDW mixing line and a WW-midpoint-LCDW mixing line can cause the curvature observed in the Amundsen Sea data. The 'original' WW-UCDW line is plotted in grey, and the new curved mixing line is plotted in black, with endpoints (WW, UCDW, LCDW) labelled. The linear mixing line between WW and LCDW is also marked on as a dashed line.

The mCDW forms from the off shelf CDW, which consists of UCDW and LCDW. This transformation occurs as the CDW moves on shelf, which is generally assumed to result in thorough mixing across the shelf, producing a well-defined mCDW end-point (changing only with bathymetry restrictions as the water mass travels south

towards PIIS). However, in the meridional section of the central channel at the continental shelf edge (Figure 3.12), the UCDW component of CDW appears to be absent on shelf, resulting in the LCDW being the main component of CDW on shelf. This could result in the upper water column retaining a mixing line between WW and UCDW, but the lower water column would mix between some point along the WW-UCDW mixing line and the LCDW component that moves on shelf. This produces a curvature of the apparent mCDW-WW mixing line, in the direction that is observed in the CTD data (Figure 3.22).

The other water mass that has not been considered is WW. This forms annually through heat loss to the atmosphere, and so is affected by the meteorological conditions each year: this interannual variability could cause variability in the endpoint. In colder winters, more sea ice will be produced, resulting in a more saline, slightly colder (due to the lowering of the freezing temperature) and lower oxygen WW being formed. This 'new', colder WW endpoint will create a new mixing line, connecting with the 'old' ambient mCDW-WW mixing line at some depth (Figure 3.23), resulting in a curvature of the apparent mixing line.

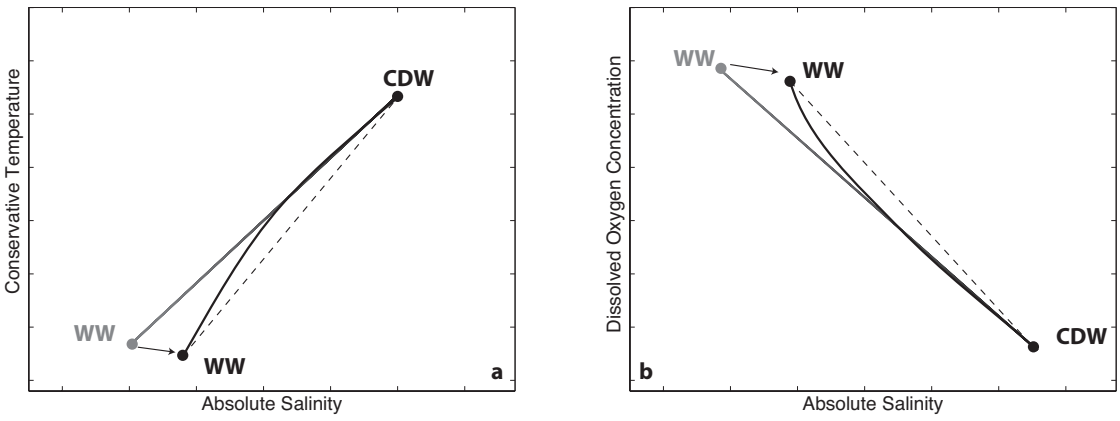

Figure 3.23: Schematic diagram to show how changes in sea ice formation or melting (causing changes in the WW endpoint) can result in the curvature seen in the Amundsen Sea data. The colder, more saline, lower oxygen WW endpoint formed in years with more sea ice formation is marked in black, whilst the slightly warmer, fresher and higher oxygen WW endpoint used as the 'original' WW endpoint is marked in grey. The curve forms between some midpoint on the original WW-CDW mixing line and the newer WW endpoint (marked in black). The linear mixing line between CDW and WW is marked as a dashed line.

It is not possible to identify whether these processes occur in the Amundsen Sea from the observational data alone, as it would require an age tracer of the water masses and more information about the WW properties between the different years. The later is difficult to collect, as the moorings that are able to capture winter measurements do not collect information from the top of the water column in order to avoid being damaged by icebergs travelling through the area.

3.6.3 Biological Activity

Biological activity can affect dissolved oxygen concentrations through productivity (increases $c(O_2)$) and respiration (decreases $c(O_2)$). As the curvature tends towards lower dissolved oxygen concentrations, and occurs at approximately 400 m depth, biological respiration is the most likely cause of depleted oxygen levels. Biological productivity occurs through photosynthesis, which requires light, but this is absent at 400 m depth. Usage of dissolved oxygen occurs through organisms respiring and remineralisation of planktonic shells as they fall through the water column. In order to form a curvature, these respiration rates must be greatest at the depth of the curvature. This may also explain why the curvature in $c(O_2)$-S_A space is greatest in the eastern channel: this was the region where the most biological productivity was seen at the surface, meaning the respiration rates at depth are likely to also be higher in order to export the new biological matter to depth.

There have been no studies in this region focusing on respiration rates at depth, which makes it hard to assess how much this process may be contributing towards the curvature. To measure these rates, year round dissolved oxygen concentration and CFC measurements would be needed.

3.7 Surface processes affecting meltwater calculation

In the Amundsen Sea, the AASW had very high MW fractions (Figures 3.5-3.12d). This was attributed to solar radiation warming and sea ice melt freshening the surface waters, resulting in higher apparent MW concentrations. This atmospheric interaction can work both ways; as austral winter approaches, the waters will cool through heat fluxes to the atmosphere and become more saline from brine rejection, reducing that apparent MW fraction. However, this is not taking into account the effects that atmospheric interaction may have on dissolved oxygen concentrations.

At the surface, the air-sea interface will tend to an equilibrium level of dissolved oxygen concentration – or the surface saturation value for that Θ and S_A. This means that if the ocean waters are over-saturated in dissolved oxygen, gas will transfer to the atmosphere, or vice-versa when the water is under-saturated. The oxygen saturation concentration tends to increase with decreasing temperature.

Biological productivity also has a large effect on the AASW dissolved oxygen concentration. Across a lot of the Amundsen Sea continental shelf CTD stations, the surface waters were over-saturated in dissolved oxygen due to biological productivity (Figure 3.4). This increase in $c(O_2)$ would cause the MW fractions to appear lower (Figure 3.16), but due to the amount of freshening from sea ice melt it has negligible effect in lowering the surface MW fractions.

In front of PIIS, the top 250 m show an almost homogeneously high MW fraction due to the strong outflow from PIG (Naveira-Garabato *et al.*, *submitted*). However, at approximately 6 and 25 km along the section, there are two areas of lower MW fraction (Figure 3.24c). When their locations are compared with the $c(O_2)$ distribution, these same regions have slightly higher concentrations of dissolved oxygen (Figure 3.24a). Whilst the fluorometer on the ship was not calibrated, the data can still be used to show relative increases (or decreases) in biological matter in the water column, and Figure 3.24b shows that there are two patches of high chlorophyll *a* concentrations that correlate with the higher $c(O_2)$ and lower MW fraction. This

shows that biological productivity (causing high chlorophyll *a* concentrations) produced dissolved oxygen, resulting in an apparent low MW fraction.

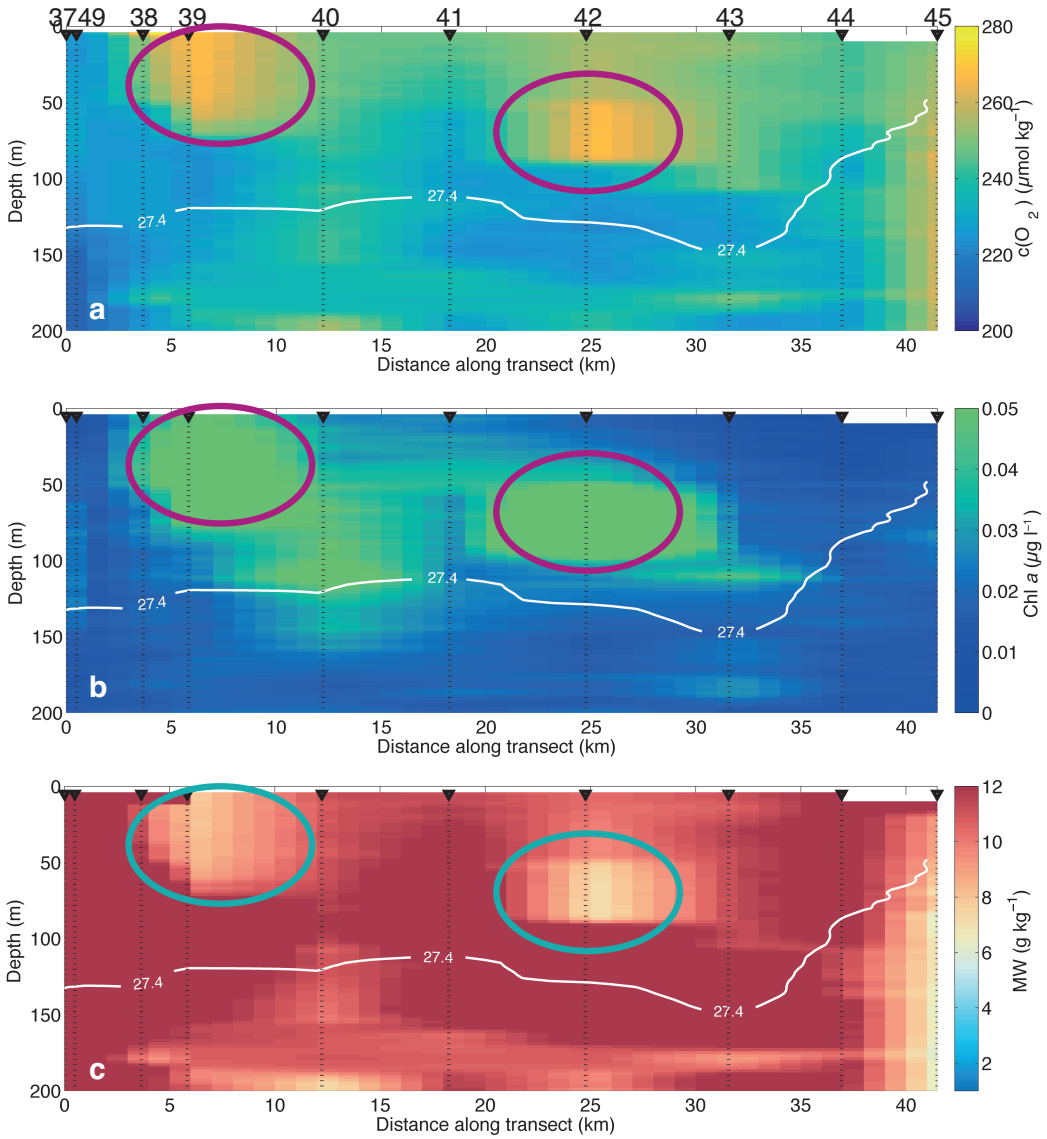

Figure 3.24: Section plots in front of PIIS (section 6), focused on the top 200 m, showing a) dissolved oxygen concentrations ($c(O_2)$), b) uncalibrated chlorophyll a *concentrations and c) MW fractions. The CTD Stations used are labelled on the top plot, and the areas of high $c(O_2)$, high chl* a *and low MW fraction are circled in purple or blue.*

Due to these surface processes, unless an atmospheric endpoint can be introduced (such as was done by Loose *et al.*, 2014), the top 150 m is ignored in MW fraction calculations. As was discussed in Chapter 2, the three tracers available (and mass conservation equation) limit the OMPA to three water masses, so an additional tracer (such as a noble gas) would need to be introduced to resolve atmospheric interac-

tion. However, the link between MW and biological productivity is interesting to investigate further, as previous studies (Raiswell *et al.*, 2008; Biddle *et al.*, 2015) have showed that sediment-laden MW can encourage biological productivity. This is discussed further in Chapter 4.

3.8 Conclusion

The Ocean2ice cruise in 2014 collected a comprehensive CTD dataset from the Amundsen Sea, including Θ, S_A and $c(O_2)$ measurements. These data identified three of the water masses on the continental shelf (mCDW, WW and AASW), as well as areas that were influenced by MW. The mCDW temperature and thickness was comparable to 1994 and 2012, and was cooler than 2009 and 2010 recordings. This thickness of mCDW may have implications for melt rate under PIG.

Endpoints were selected for mCDW and WW for use in the MW fraction calculations. The values for PIB were used for mCDW, and, due to warming of WW by MW in the PIB region, the eastern channel endpoint was used for WW. This selection highlighted that the eastern channel and shelf edge requires different endpoints due to the warmer mCDW endpoint that exists in this area.

Throughout the Amundsen Sea region the surface waters displayed very high apparent MW fractions, due to solar radiation and sea ice melt. In front of PIIS, the surface waters were also seen to be affected by biological productivity. This linkage between the existence of MW and biological productivity is explored further in Chapter 4.

The main PIG MW outflow signature was observed towards the southern end of the ice shelf, with eddy-type structures forming as the MW exited the ice shelf. These structures were visible up to 60 km away from the ice shelf and most likely formed due to the high turbulence that the MW obtained as it left the cavity (Naveira-Garabato *et al.*, *submitted*). Meltwater from icebergs in PIB was identified towards

the surface of the water column, whilst glacial MW from the Abbott Ice Shelf was observed at approximately 200 m depth in the eastern channel.

At approximately 400 m depth a meltwater plume was observed in all sections. This was correlated to a curvature seen in both Θ-S_A and $c(O_2)$-S_A space, but spatial variations and an exaggerated effect on $c(O_2)$ indicated that this curvature was not caused by MW. Variations in the mCDW or WW endpoints were suggested as alternative hypotheses, whilst biological respiration could be responsible for the decreases seen in $c(O_2)$.

It is important to understand the source of this curvature in order to improve the reliability of the MW fraction calculations. The processes postulated for causing the curvature cannot be proven to occur from the observational dataset, and so an alternative approach, such as ocean modelling, needs to be used to see how these processes may affect the water column. This is discussed further in Chapter 5.

Chapter 4

Iceberg Enhanced Biological Production in the Northwestern Weddell Sea

The following chapter was published as a paper in *Geophysical Research Letters* under the title 'Ocean glider observations of iceberg-enhanced biological production in the northwestern Weddell Sea', with co-authors Jan Kaiser, Karen J. Heywood, Andrew F. Thompson and Adrian Jenkins. All writing and work was undertaken by L. C. Biddle, with comments and input from collaborators. It is as published, except for the inclusion of a supplementary figure and more discourse on Seagliders, which have been added for increased understanding of data collection.

This chapter demonstrates how glacial meltwater and biological production can affect dissolved oxygen concentrations at the surface. The relationship between glacial meltwater and biological productivity is an important one to bear in mind when calculating meltwater fractions; in Chapter 3, CTD stations were identified where biological productivity at the surface caused a decrease in the meltwater fraction due to elevated dissolved oxygen concentrations. In the case discussed within this chapter, glacial meltwater acts to increase dissolved oxygen concentrations, in

addition to the contribution from biological productivity.

Biddle, L. C., J. Kaiser, K. J. Heywood, A. F. Thompson, and A. Jenkins (2015), Ocean glider observations of iceberg-enhanced biological production in the northwestern Weddell Sea, *Geophys. Res. Lett., 42,* 459–465, doi:10.1002/2014GL062850.

4.1 Introduction

Almost half of the mass loss from Antarctica is attributed to iceberg calving (Depoorter *et al.*, 2013). Atmospheric warming increases iceberg production from the Antarctic Peninsula into the Weddell Sea (Scambos *et al.*, 2000). Icebergs enhance primary productivity (Martin *et al.*, 1990; Raiswell *et al.*, 2008; Lancelot *et al.*, 2009) and recent studies have described icebergs as “Lagrangian estuaries"; a localised nutrient and iron (Fe) rich environment that encourages phytoplankton blooms (Smith *et al.*, 2007, 2011). Additional melting ice may therefore have a significant impact on the ecosystem of the Antarctic coastal seas. Ocean colour remote sensing, using 10 years of data, showed that the effect of icebergs on production varied between October to March, depending on the existing environmental conditions (Schwarz and Schodlok, 2009). For example, on average during February, an iceberg caused a decrease in chlorophyll *a* concentrations, thought to be due to an increase in vertical mixing, resulting in dilution of the surface phytoplankton concentration. There are in-situ observations of delivery of Fe by icebergs with the potential to enhance productivity (Martin *et al.*, 1990; Smith *et al.*, 2007; Raiswell *et al.*, 2008; Lancelot *et al.*, 2009), but these observations are inconsistent with the apparent decrease in chlorophyll *a* concentrations observed by Schwarz and Schodlok (2009). One of the methods of mixing proposed by Schwarz and Schodlok (2009) to enhance productivity (or dilute chlorophyll *a*) is caused by basal and sidewall melting of the iceberg. The meltwater is fresher than ambient waters, and so relatively buoyant (Huppert and

Turner, 1980; Jenkins, 1999). This upwelling promotes turbulent mixing through the water column. Depending on the conditions, the upwelled water may enhance phytoplankton growth through micronutrient injection into the surface layer or dilute chlorophyll *a* concentrations (Neshyba, 1977; Sancetta, 1992; Vernet *et al.*, 2011). Mechanical mixing can also occur at the keel depth of the iceberg, where the movement of the ice stirs up waters and sediment nearby. Besides injecting micronutrients through enhanced mixing, icebergs carry terrigenous materials that are released during melting, providing another source of particulate iron (Raiswell *et al.*, 2008; Lancelot *et al.*, 2009; Shaw *et al.*, 2011). In the Weddell Sea, icebergs and low salinity surface waters were found to be enriched in dissolved iron (Lin *et al.*, 2011).

The northwestern Weddell Sea, where the Antarctic Slope Current carries icebergs along the continental slope around the Powell Basin, is known as 'iceberg alley' (Thompson and Heywood, 2008; Gladstone *et al.*, 2001; Stuart and Long, 2011). Whilst the population of icebergs in this area is relatively dense, the scarcity of *in-situ* observations of iceberg-related biological activity is in part due to the logistics of accessing this remote region and also the ship-time required to identify and track a suitable iceberg for study. A glider deployment there surveyed biological, chemical and physical properties at high spatial and temporal resolution close to a large iceberg. Here we present evidence of enhanced biological production in surface waters affected by the iceberg and describe how small scale patchiness is an underestimated feature of Southern Ocean production.

4.2 Data Collection and Seagliders

As part of the GENTOO ('Gliders: Exciting New Tools for Observing the Ocean') project, Seaglider SG522, Beluga, (Eriksen *et al.*, 2001) surveyed the continental shelf and slope in the northwestern Weddell Sea between January and March 2012 (Figure 4.1). The Seaglider is an autonomous underwater vehicle that profiles be-

tween the surface and 1000 m on a dive slope of approximately 25°, giving an effective spacing between full depth dives of approximately 4 km (Figure 4.2). The glider ascends or descends by changing its buoyancy relative to the water column by pumping oil between internal and external reservoirs. It is also able to execute small navigational changes whilst underwater through meridional and zonal battery movements, using an onboard compass and depth-average current calculations made using hydrodynamical parameters. During 310 profiles, the glider, equipped with a Seabird CT sail, Aanderaa oxygen optode and a WETLabs ECO Triplet, measured pressure, temperature, salinity, dissolved oxygen concentration, chlorophyll and CDOM (Coloured Dissolved Organic Matter) fluorescence and optical backscatter (532 nm).

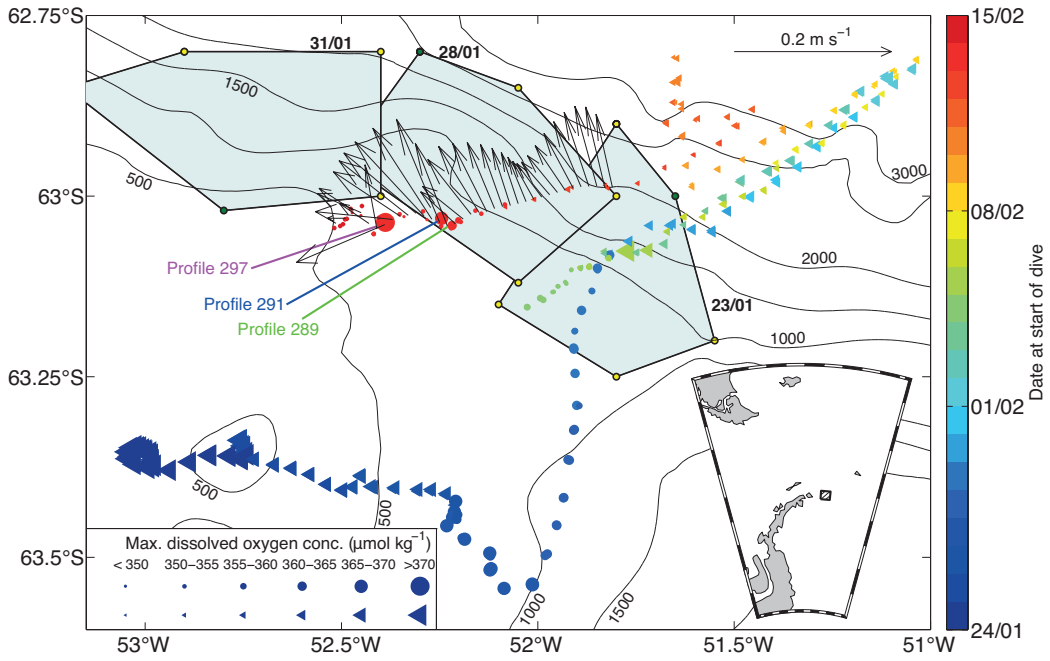

Figure 4.1: Maximum dissolved oxygen concentration shown by size of symbol (see legend), measured during each vertical profile completed by the glider (two profiles per dive, see Figure 4.2), with bathymetry contours every 500 metres. Circles represent profiles in or near the Antarctic Slope Current (ASC), and triangles are the remaining profiles from the mission. The iceberg outlines are from Polarview SAR satellite imagery, with one corner coloured green to highlight the spinning of the iceberg. The three profiles of interest (289, 291, 297) can be seen near to the outline of the iceberg on 28/01. Arrows indicate the dive-averaged current measured from the glider and show the strong currents that indicate the ASC.

The TEOS-10 absolute salinity (S_A; IOC *et al.*, 2010) and conservative temperature (Θ) scales are used to report all salinity and temperature values. Outliers and

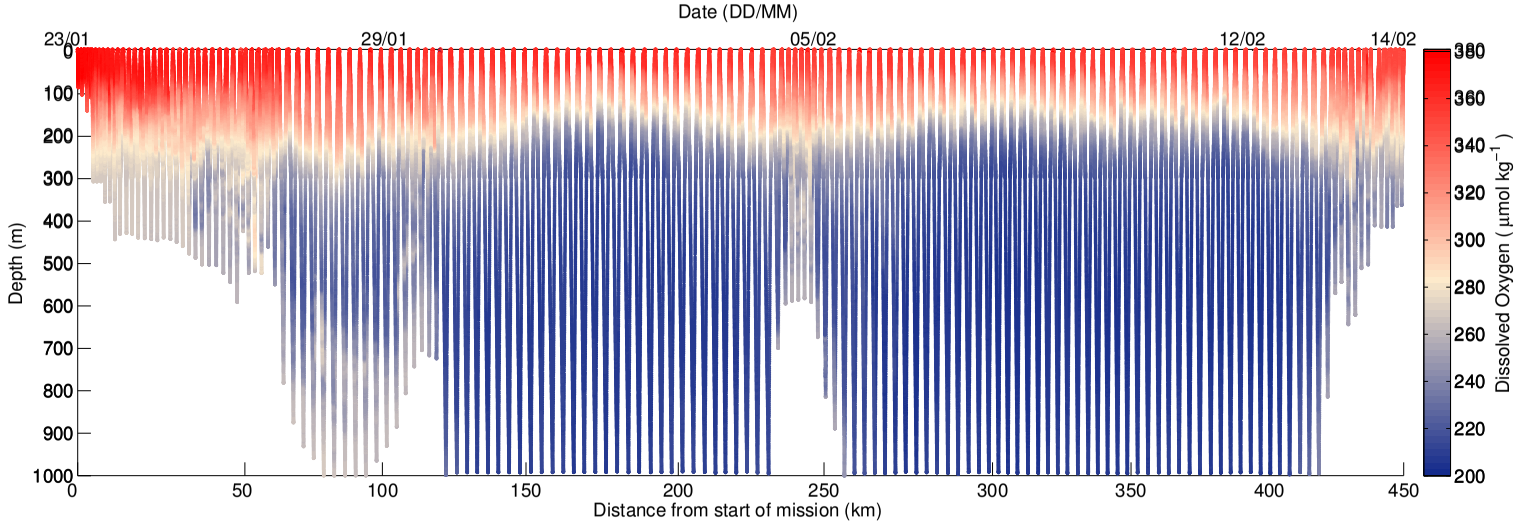

Figure 4.2: All dissolved oxygen data from glider SG522, between 23rd January 2012 and 14th February 2012. Both date and distance from start of the mission are measured along the x-axis, showing the high spatial and temporal resolution of data that ocean gliders are able to collect. High dissolved oxygen concentrations can be seen in the surface waters, and at the beginning of the deployment a small eddy can be seen on shelf.

surface spikes were identified and removed from the glider salinity and dissolved oxygen data. Salinity was calibrated against in-situ water samples collected during deployment. Dissolved oxygen concentrations could not be calibrated against Winkler titrations, but are of the expected magnitude when adjusted for the colder Antarctic temperatures (within 20 μmol kg^{-1} of air saturation at the surface). However, this is not a problem, as the method used here to calculate net community production (Riser and Johnson, 2008) only requires measurement of a change in oxygen concentration over time. Chlorophyll *a* and CDOM concentrations were derived from the fluorescence measurements using the manufacturer's calibration curves.

Synthetic Aperture Radar (SAR) satellite data were obtained from Polar View Antarctica [*www.polarview.aq*] to track a large iceberg (C-19c, 39 km x 22 km) that transited through the northwest Weddell Sea during the cruise, between 23rd - 31st January (Figure 4.1). It travelled cyclonically along the continental shelf break, west of the Powell Basin (Fig 4.1). Satellite ocean colour observations were not available during the study period, as clouds obscured the area of interest. Schwarz and Schodlok (2009) and Arrigo *et al.* (2008) also encountered this problem during the same season (late summer).

The Antarctic Slope Front is located using a hydrographic definition; the shoreward extent of the 0 °C isotherm and an oxygen minimum concentration of >240 μmol kg^{-1} occur at a neutral density anomaly of 28.2 (Jacobs, 1991; Thompson and Heywood, 2008). We define glider profiles lying within, and immediately on the flanks of, the Antarctic Slope Front as those with minimum dissolved oxygen concentrations between 235 - 245 μmol kg^{-1} at a potential density anomaly of 27.8. These profiles are shown in Figure 4.1, where the glider's depth-averaged current vectors also show the Antarctic Slope Current.

4.3 Results and Discussion

Three main water masses are identified in the glider data by their hydrographic characteristics (Figure 4.3a): relatively warm and saline Circumpolar Deep Water (34.8 g kg^{-1}; CDW), the temperature minimum layer (Winter Water, WW), and the relatively fresh (33.4 g kg^{-1} – from sea ice melt over summer) Antarctic Surface Water, cooling toward the freezing point (-1.83 °C) as autumn proceeds. Dissolved oxygen concentrations decrease from around the air saturation value of 370 μmol kg^{-1} to 200 μmol kg^{-1} for CDW (Figure 4.3b).

Three glider profiles (289, 291, 297), close to the shelf break at isobaths of 600 - 800 m, show the signature of iceberg meltwater in the top 15 m (Figure 4.4). These three profiles are each no further than 2 km from other profiles that do not show the same features, suggesting a representative scale of this meltwater signature. The profiles have cooler and fresher surface water than those nearby (profiles 283 - 310; on average by 0.1 °C and 0.1 g kg^{-1} lower; Figure 4.4a,b) and show mixing between WW and a cold, fresh water mass in their Θ-S_A profiles (Figure 4.3a). There is no peak in the chlorophyll fluorescence measured on these profiles (Figure 4.4d), but CDOM concentration and optical backscatter have peaks at depths shallower than 5 metres. These profiles exhibit the highest values of these latter parameters of the entire deployment of the glider at 7.93 μg L^{-1} and 0.0323 m^{-1} sr^{-1} (Figure 4.4e,f). These CDOM and backscatter peaks indicate high levels of yellow-brown particles in the water, which can represent dead algae or terrigenous material deposited by the iceberg (Raiswell *et al.*, 2008; Lin *et al.*, 2011).

These profiles are also distinguishable by their higher dissolved oxygen concentrations compared with other profiles above similar isobaths (Figure 4.1). They show striking peaks in dissolved oxygen concentrations at 8-12 m depth (average 9 μmol kg^{-1} higher than average local values; Figures 4.3b and 4.4c). The depth of the dissolved oxygen concentration enhancement in profile 297 is much greater than in profiles 289 and 291 (Figure 4.4c). Other than the latter two profiles that show a de-

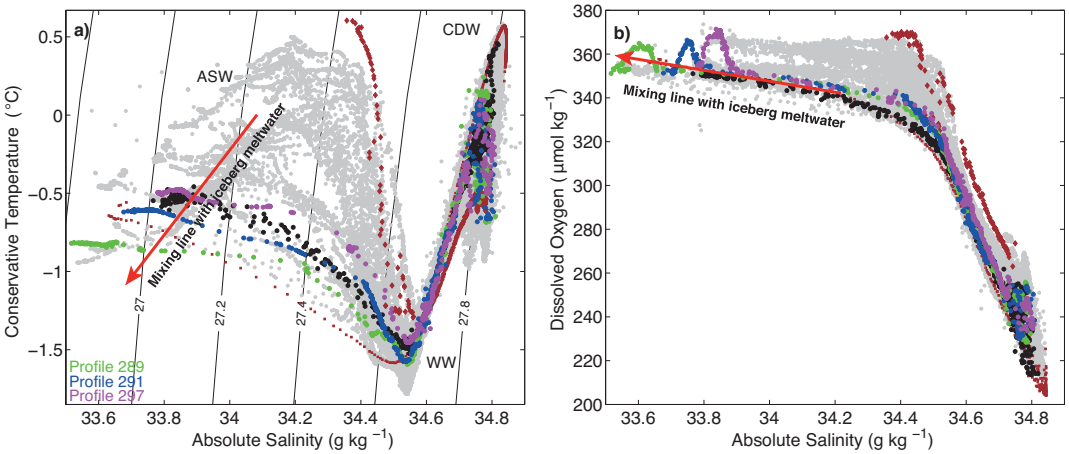

Figure 4.3: Glider data showing the three main water masses; Antarctic Surface Water (AASW), Winter Water (WW), Circumpolar Deep Water (CDW), where any data-points lying between these water masses indicate mixing between them. (a) Conservative temperature against absolute salinity; (b) dissolved oxygen against salinity. It also highlights the three profiles of interest (289, 291 and 297, in colour); grey profiles represent other profiles in the ASC (selected through the hydrographic definition of the ASC) and the brown lines represent the other two groups of profiles (dots are in deeper waters, squares are on shelf). The black lines represent profiles 283 - 310. The red arrows represent the mixing line between surface waters and iceberg meltwater.

crease, it shows increased temperature and salinity compared to surrounding waters, which is likely due to its location on the inshore side of the ASC (Figure 4.1).The elevated dissolved oxygen concentrations could be due to glacial meltwater: the dissolved oxygen concentration in pure (zero salinity) iceberg meltwater is calculated to be (1120±95) μmol kg^{-1} (Hellmer *et al.*, 1998; Martinerie *et al.*, 1992). Assuming this value, we can calculate the meltwater contribution to measured oxygen concentrations for each glider profile.

$$S_{\mathrm{a}} A + S_{\mathrm{MW}}(1 - A) = S_{\mathrm{O}}, \tag{4.1}$$

$$A = \frac{S_{\mathrm{O}}}{S_{\mathrm{a}}}. \tag{4.2}$$

$$c(O_{2,\mathrm{a}})A + c(O_{2,\mathrm{MW}})(1 - A) = c(O_{2,\mathrm{b}}). \tag{4.3}$$

This calculation is shown in equations 4.1 – 4.3, where the salinity observed (S_O), the meltwater salinity (S_{MW}) and the average salinity (S_a, from local profiles)

are used to calculate the fraction of meltwater present, $(1 - A)$. This value is used to calculate how much oxygen is added to the average oxygen concentration ($c(O_{2,\mathrm{a}})$) by the meltwater ($c(O_{2,\mathrm{MW}})$), resulting in $c(O_{2,\mathrm{b}})$. This is represented in Figure 4.3b, where the uncertainty relating to the pure meltwater oxygen value is not shown, as the change in slope of the line is indistinguishable at these salinities. The measured values for the average profiles can be seen to follow this mixing line in Figure 4.3b, but the three profiles that observed the striking peaks show values greater than that expected from meltwater dissolved oxygen alone.

Icebergs can deposit micronutrients (including dissolved iron) through meltwater, which can enhance biological production (Raiswell *et al.*, 2008; Lin *et al.*, 2011), which in turn increases dissolved oxygen concentrations. The combination of the evidence for meltwater and a mechanism for enhanced biological production of oxygen from icebergs shows that these dissolved oxygen concentration peaks were caused by iceberg-enhanced biological production. The production is most likely stimulated by iceberg micronutrients deposited at the surface, as opposed to nutrient rich CDW being upwelled. Upwelled CDW would show distinct warmer, saltier anomalies in the Θ-S_A profiles, but the meltwater appears here as colder, fresher and only within the top 15 m. There are also four profiles between 289 - 299 that do not show any influence from the iceberg (profiles 293 - 296). Figure 4.1 shows that these profiles are in the core of the Antarctic Slope Current, indicating that any micronutrients or possible signs of production would have been advected away quickly.

The iceberg passed through the area of observed meltwater between January 27th - January 29th, whilst the glider sampled the water on February 14th. Schwarz and Schodlok (2009) found that SeaWiFS ocean colour data showed peak production rates six days after an iceberg's passage, whilst in-situ observations still recorded elevated chlorophyll *a* concentrations up to 10 days after (Helly *et al.*, 2011). This may explain why no peak in chlorophyll fluorescence is observed 17 days after the iceberg's passage, as the glider has sampled waters after the biological production

peak, when chlorophyll *a* concentrations have returned to background values.

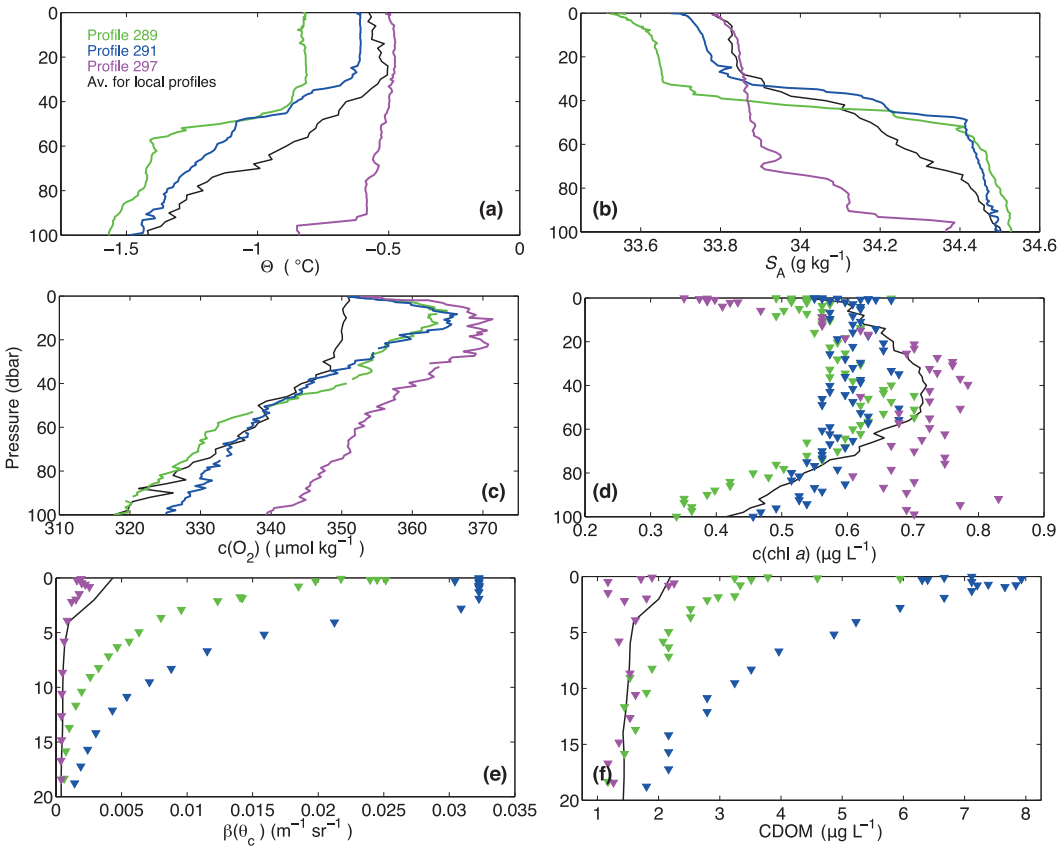

Figure 4.4: Glider profiles of (a) conservative temperature, (b) absolute salinity, (c) dissolved oxygen concentration, (d) chlorophyll a fluorescence, (e) backscatter and (f) coloured dissolved organic matter (CDOM). The coloured lines or triangles represent data collected on the profiles of interest, whilst the black lines represent the average values from profiles surrounding the area of interest (profiles 283 -310).

An estimate of the net community production (NCP) can be made from the amount of additional dissolved oxygen observed in the profiles affected by iceberg meltwater. As the dissolved oxygen measurements are not calibrated against *in situ* water samples, the difference between the dissolved oxygen concentrations in profile 289 or 291 and the background dissolved oxygen concentrations is used to represent the oxygen added through production, similar to methods used by Riser and Johnson (2008). The dissolved oxygen concentrations calculated in equation 4.3 ($c(O_{2,\mathrm{b}})$) include $c(O_{2,\mathrm{MW}})$ and so are used as the background values.

The dissolved oxygen concentration is integrated between the points where the elevated O_2 profile intersects the background O_2 profile (shown in Figure 4.4). The

difference between these profiles corresponds to an increase in the dissolved oxygen inventory of (328±9) mmol m^{-2} between 0 and 37.5 m for profile 291 (Figure 4.5). We assume that this increase is entirely due to NCP over (16±2) days. This requires a NCP of (21±3) mmol m^{-2} d^{-1} O_2 to produce the dissolved oxygen observed. A correction can be made for air-sea gas exchange by assuming that the peak dissolved oxygen concentration was initially present at the surface (dotted line, Figure 4.5, following Riser and Johnson, 2008). Integrating along the new line and following the same methodology as before results in an O_2 inventory increase of (422±9) mmol m^{-2}, corresponding to a NCP of (27±4) mmol m^{-2} d^{-1} O_2. Using the approximation that NCP(O_2) divided by the photosynthetic quotient is equal to net primary production (14C-NPP; Marra, 2009), 14C-NPP is calculated to be (232±34) mg m^{-2} d^{-1}. This is comparable to values found by Vernet *et al.* (2011) in the Weddell Sea (average of (275.7±123.1) mg m^{-2} d^{-1}). The same method was used for profiles 289 and 297, which resulted in 14C-NPP values of (77±14) mg m^{-2} d^{-1} and (615±82) mg m^{-2} d^{-1} respectively.

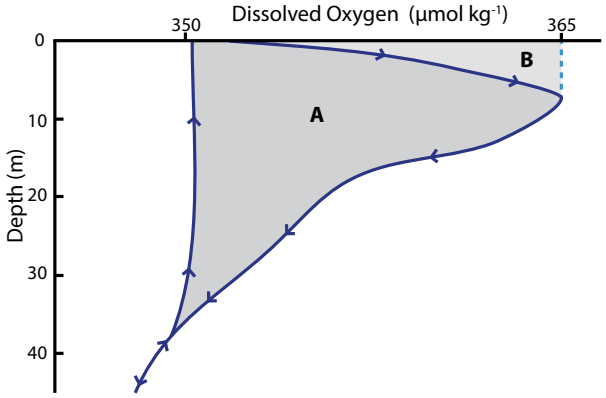

Figure 4.5: Schematic from profile 291 illustrating how the additional oxygen was calculated. The difference between profile 291 and average dissolved oxygen concentration from the local area (area A) provides the excess dissolved oxygen inventory. Since the meltwater influence likely extended to the surface, area B is added to area A in the NCP calculation to correct for any oxygen lost due to air-sea exchange (following Riser and Johnson, 2008).

Enhanced biological production caused by micronutrients from an iceberg has been reported before (Martin *et al.*, 1990; Raiswell *et al.*, 2008; Lancelot *et al.*, 2009), but what is important about these glider observations is the spatial scale and

timing of the production. The production is affected by fine-scale variability in the region, with productive profiles less than 2 km from profiles showing no enhanced production. This small scale patchiness of the production would not be visible on typical MODIS or SeaWiFS chlorophyll products, with a resolution of 4 or 9 km (e.g. those used by Arrigo *et al.*, 2008). However the satellite imagery is available in up to 1 km resolution (e.g. Schwarz and Schodlok, 2009), which is likely to resolve these features, and the use of which should be encouraged. Yet Schwarz and Schodlok (2009) did not identify any similar small scale production features, and also observed lower chlorophyll *a* concentrations in February around icebergs. A further complication is the high levels of cloud cover around Antarctica. At about 60 °S, the annual mean cloud cover is 65-70% (King and Turner, 1997), which during the 'growing' season of October to March could correspond to 118 days of cloud cover. Neither MODIS or SeaWiFS imagery was available for the period covered by this study, suggesting that cloud cover could cause significant underestimates in local production rates.

The lack of any evidence for an increase in chlorophyll *a* in the profiles affected by meltwater and increased production may suggest that there is a decoupling between chlorophyll *a* concentrations and carbon removal, and that NCP may be enhanced even where there is no observable chlorophyll *a* increase. This decoupling could be due to the time lag between the production and observations being made resulting in accumulation of the dissolved oxygen. Alternatively, the community structure of phytoplankton could lead to variations in the carbon to chlorophyll *a* ratio (Westberry and Behrenfeld, 2014). This can explain why no increase was seen in chlorophyll *a* concentrations around icebergs Schwarz and Schodlok (2009). The cause of decoupling is potentially an important mechanism that requires further study.

4.4 Conclusion

Ocean gliders deployed in the northwestern Weddell Sea observed lower temperature and salinity, and increased dissolved oxygen, CDOM and backscatter at depths between 5 and 15 m following the passage of a large iceberg. The dissolved oxygen concentrations were higher than values expected from iceberg meltwater, indicating that biological production had occurred, most likely due to the deposition of micronutrients from the iceberg. There was no observed enhancement of chlorophyll *a* concentrations, suggesting a decoupling between NCP and chlorophyll *a* concentrations. This is a mechanism that will require a focused study in the future.

All properties showed submesoscale spatial variability. On such small scales, even sampling by gliders have limitations; out of over 80 profiles in the direct track of the iceberg, only three showed a signature of biological production. These smaller, localised production zones are an important consideration for future calculations of Southern Ocean production. Previous reports have suggested that icebergs have little, or no, effect on biological production in the later summer months (Schwarz and Schodlok, 2009). More high-resolution observations are required to identify how frequent these localised production areas are in order to quantify more accurately their overall effect on the Southern Ocean carbon budget. Ocean gliders may prove to be an invaluable resource for iceberg studies, as they have the potential to move in closer to the waters surrounding an iceberg than a ship can.

Although this study was focussed on the Weddell Sea, the processes observed here will be applicable to the Amundsen Sea as well. The relationship observed between dissolved oxygen concentrations and iceberg meltwater, where the micronutrients contained in the iceberg meltwater likely enhanced biological activity, is important to consider when calculating glacial meltwater signatures. At the surface, this increase in biological productivity will act to artificially decrease the meltwater signature, and so these processes must be in some way accounted for.

Chapter 5

Modified Price-Weller-Pinkel Model for the Amundsen Sea

5.1 Introduction

In the Amundsen Sea, we identified a curvature in the mixing line between mCDW and WW, appearing as a meltwater signature (Chapter 3). Alternative hypotheses for the curvature focused on endpoint variability, due to sea ice processes or on-shelf transport of LCDW, or respiration decreasing dissolved oxygen concentrations. To identify which of these processes most likely contributes to the curvature, simulations of the Amundsen Sea were undertaken using a one-dimensional ocean model.

Models are an essential part of oceanographic studies: through modelling the oceans, we can observe how different boundary conditions, parameterisations or initial forcings can affect each variable. Stommel's two-box model (1961) first informed us about thermohaline convection. In a matter of decades, complex global atmosphere-ocean-ice coupled models have been developed that can attempt to forecast the climate over hundreds of years (cf. HadCM3; Gordon *et al.*, 2000). Yet simple models still play an important role in research, especially when stripping back complex ocean interactions and instead focusing only on the fundamental processes

at play in a certain ocean column.

One-dimensional ocean models are typically defined by what vertical mixing scheme is used for the mixed layer. These can be split into two categories; turbulence closure scheme models and bulk mixed layer models. Turbulence closure scheme models use eddy diffusivity (K; they are also known as K-models) to parameterise small-scale turbulence within the mixed layer. Where the mixing takes place varies with each time-step; the mixing is spatially and temporally variable. These models vary in what order of turbulence is dealt with numerically, and the most frequently cited are the first-order closure K Profile Parameterisation scheme (KPP; Large *et al.*, 1994) and second-order closure Mellor-Yamada model (Mellor and Yamada, 1982). Whilst these models arguably have a good representation of ocean dynamics, they are computationally expensive due to the number of calculations required for the turbulent fluxes.

Bulk mixed layer models treat the mixed layer as a 'slab', where all water properties are homogeneous; some of the first examples of mixed layer ocean models use this mechanism (e.g. Kraus and Turner, 1967). Kraus and Turner (1967) use momentum and buoyancy fluxes to calculate the entrainment velocity, which then determines the mixed layer depth (MLD; h). This mechanism largely drives the deepening of the MLD, as the entrainment velocity will only become negative (and therefore upwards) when the thermal stratification is stronger than the wind stirring. Niiler and Kraus (1977) list further developments on this model type, including allowances for horizontal shearing motions. Treating the mixed layer as a homogeneous slab is computationally efficient, but typically these models neglect any turbulent mixing below the mixed layer.

The model used in this study is the Price-Weller-Pinkel model (PWP; Price *et al.*,1986). This falls within the bulk mixed layer category, but diagnoses the MLD using critical Richardson number values and allows for shear mixing across the mixed layer boundary. The model will be developed for use in the Amundsen Sea using

a hybrid of a Kraus-Turner scheme and the PWP bulk mixed layer model, similar to Chen *et al.* (1994), resulting in a modified Price-Weller-Pinkel model (mPWP). Finally, the model will be run to try to simulate the processes hypothesised to cause the curvature observed in Chapter 3.

5.2 Price-Weller-Pinkel model

The PWP model was developed to investigate mixed layer processes in tropical oceans, and uses simple physics to describe what is occurring in the water column. By developing the fundamental equations it is easy to modify the model for our purpose and to identify which processes contribute to water mass transformations. The model script used originates from Lazarevich and Stoermer (2001), which is a modification of the original PWP script from Fortran into Matlab code and includes background diffusion.

PWP is a bulk mixed layer model, which means that it considers the main driving equations over the entire mixed layer, and averages the ocean properties (temperature, salinity, and meridional and zonal current velocities) over the mixed layer depth. The main differences between the various bulk mixed layer models are how they parameterise the turbulent kinetic energy (TKE) budget. The TKE budget is used to determine whether the mixed layer depth will increase or decrease, in order to keep the overall energy budget in balance: if the TKE is negative the mixed layer will shoal, and if it is positive it will deepen. The TKE budget can be considered to be made up of five constituent parts (Gaspar, 1988). Each part represents different sources (or sinks) of TKE, also shown in Figure 5.1:

(1) Entrainment of waters into the mixed layer across the mixed layer boundary (sink)

(2) Surface flux of TKE through wind stirring or breaking waves (source)

(3) Shear production of TKE across the base of the mixed layer (source)

(4) Buoyancy forcing through stratification or overturning (sink or source)

(5) Dissipation of TKE (sink).

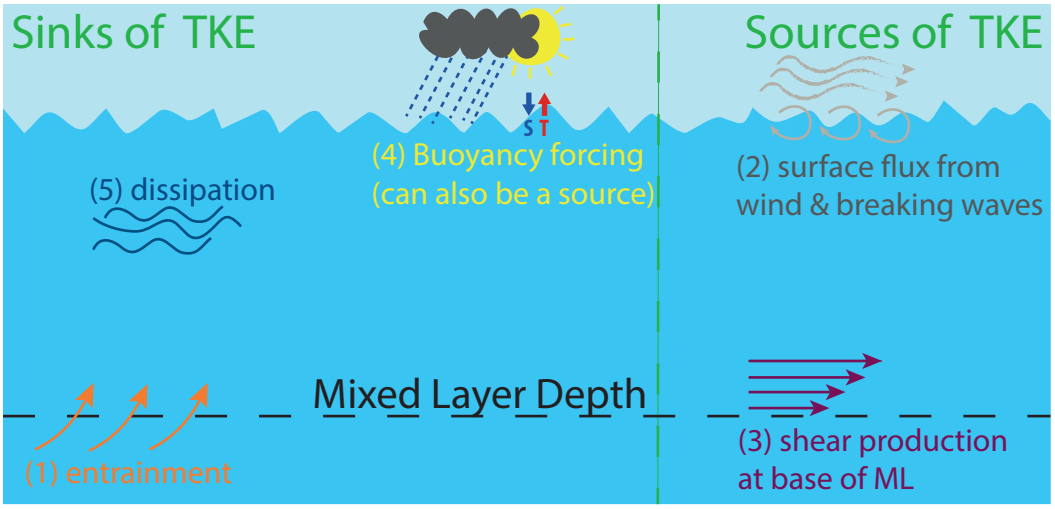

Figure 5.1: Schematic showing the sources and sinks of TKE in (and around) the mixed layer.

Kraus and Turner (1967) use parts (2), (4) and (5) to calculate the entrainment velocity (part (1)), which then determines the mixed layer depth. However, the PWP uses diagnostic equations to calculate the mixed layer depth, focusing instead on the parameterisation of part (3). This part of the TKE budget is parameterised in the PWP model using bulk and gradient Richardson number calculations (discussed further below). The bulk Richardson number is used to check that the interface at the base of the mixed layer is stable, whilst shear driven mixing in the pycnocline is parameterised through the gradient Richardson number. Both of these processes are excluded from the Kraus-Turner schemes. Their inclusion is the reason for our use of the PWP model, as shear production of TKE is important for the development of the thermocline – the region where the processes that could cause the curvature seen in Chapter 3 may occur. The mixed layer depth is determined from the profile independently at each time-step (Δt = 100 s). To do this, the model requires a fixed, high-resolution grid, with depth increment Δz (3 m; where z is equal to $(k-1)\Delta z$).

The model requires meteorological forcings that include heat (Q_i – heat inputs and Q_o – heat outputs) and freshwater fluxes (Q_fw), which are then applied to the topmost grid cell, with solar irradiation being further absorbed at depth (equations 5.1 - 5.2). The heat fluxes consist of sensible heat, latent heat and net longwave radiation (which are defined as positive out of the ocean). χ_k represents the property χ at depth index k. The model adds each process as a separate step at each timestep.

$$T_1 = T_1 + \frac{(Q_\mathrm{i}\ \alpha - Q_\mathrm{o})}{\sigma_\theta\ c_\mathrm{w}} \frac{\Delta t}{\Delta z}, \tag{5.1}$$

$$S_1 = \frac{S_1}{1 - \left(Q_\mathrm{fw} \frac{\Delta t}{\Delta z}\right)}, \tag{5.2}$$

where T_k is the ocean temperature (°C), S_k is the salinity, σ_θ is the potential density, c_w is the specific heat capacity of water and α is a parameterisation of the attenuation of solar irradiation with depth (equations 5.3 - 5.4; Paulson and Simpson, 1977).

$$I(z) = I(0)\left(0.6e^{\frac{-z}{0.6}} + 0.4e^{\frac{-z}{20}}\right), \tag{5.3}$$

$$\alpha = 0.6\left(e^{\frac{-z}{0.6}} - e^{\frac{-z+\Delta z}{0.6}}\right) + 0.4\left(e^{\frac{-z}{20}} - e^{\frac{-z+\Delta z}{20}}\right). \tag{5.4}$$

The parameterisation of the attenuation of solar irradiation uses the difference of solar irradiation between each grid cell (at depths z and $z+\Delta z$) as the fraction of solar irradiation that has been absorbed in that water parcel (equation 5.4). The equations are made up of two parts – the longer-wave (red) component, and the shorter-wave (blue) component, which decrease with depth at different rates. It is assumed that approximately 60% of the incoming solar radiation is made up of the 'red' light, and each wavelength has an attenuation length (Paulson and Simpson, 1977; 0.6 or 20 m). These coefficients vary depending on the optical properties of the water type in the region, and for this model study we use type 1a (in Jerlov classification; Jerlov, 1968). Compared with the Ocean2ice hydrographic observations, this water type is similar to a large proportion of the profiles from PIB and at the continental shelf edge,

which are two areas where we are interested in identifying how the processes affect the meltwater calculation (Figure 5.2).

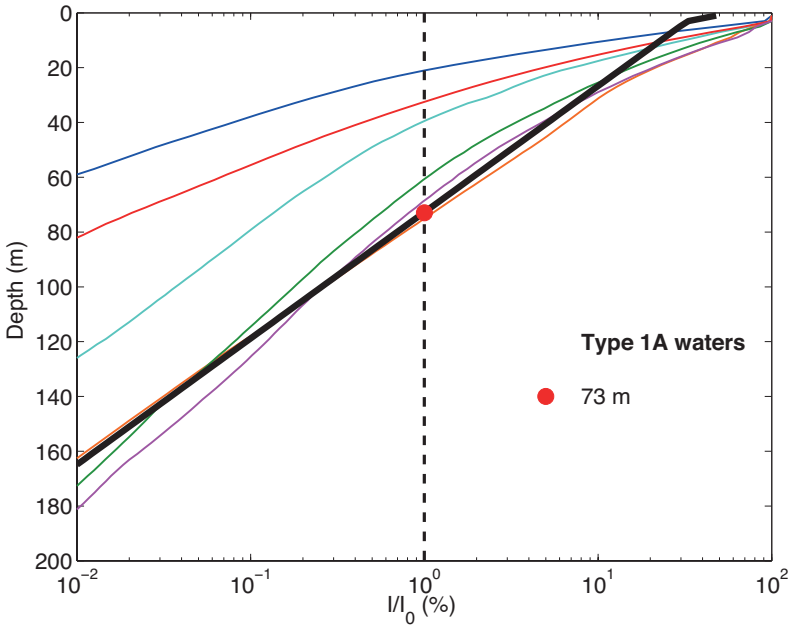

Figure 5.2: Percentage of surface irradiance ($\frac{I}{I_0}$ %) plotted against depth (m). The attenuation of light in Type 1A waters is plotted as a black line, and light levels for Ocean2ice data derived from Photosynthetically Active Radiation values (coloured following categories defined in Chapter 3) are plotted behind. The red line shows the point at which light levels are 1 % of the initial light level. Pine Island Bay (orange) and off shelf (green) values typically lie around the Type 1A line, but other stations on shelf have water with a higher light attentuation.

Vertical mixing occurs when the results of the diagnostic equations for static stability, mixed layer stability and shear flow stability do not satisfy their stability criteria. Static stability is diagnosed by calculating the vertical density gradient; this value must be non-negative for the water column to be gravitationally stable (equation 5.5).

$$\frac{\Delta\sigma_\theta}{\Delta z} \geq 0. \tag{5.5}$$

The mixed layer and shear flow stability equations (as will be seen in equations 5.12-5.14) parameterise the effects of wind driven shear on the water column. Critical Richardson numbers are used as the limits of stability for the mixed layer and shear flow stability equations. The velocities (u, v) are adjusted to account for inertial

motion caused by the rotation of the Earth, in combination with applying the wind stress to the water column. The order of these processes is outlined below (equations 5.6-5.11):

$$u'_k = u_k \cos\left(\frac{-f\ \Delta t}{2}\right) - v_k \sin\left(\frac{-f\ \Delta t}{2}\right), \tag{5.6}$$

$$v'_k = v_k \cos\left(\frac{-f\ \Delta t}{2}\right) + u_k \sin\left(\frac{-f\ \Delta t}{2}\right), \tag{5.7}$$

where f is the Coriolis parameter and for $(k-1)\Delta z < h$. The effect of rotation for the time-step is halved, as it is completed after the wind stress has been applied to the surface water.

$$u'_k = u'_k + \frac{\tau_x}{h\ \sigma_{\theta 1}}\ \Delta t, \tag{5.8}$$

$$v'_k = v'_k + \frac{\tau_y}{h\ \sigma_{\theta 1}}\ \Delta t, \tag{5.9}$$

where τ_x and τ_y are the zonal and meridional wind stress and h is the mixed layer depth. Finally, the affect of the rotation of the Earth on the water column is completed:

$$u_k = u'_k \cos\left(\frac{-f\ \Delta t}{2}\right) - v'_k \sin\left(\frac{-f\ \Delta t}{2}\right), \tag{5.10}$$

$$v_k = v'_k \cos\left(\frac{-f\ \Delta t}{2}\right) + u'_k \sin\left(\frac{-f\ \Delta t}{2}\right). \tag{5.11}$$

The bulk Richardson number calculates the ratio between buoyancy and current shear over the entire mixed layer and $\Delta\sigma_\theta$ or ΔV (where V is the current speed) relates to the difference in those variables between the layer being examined and the mixed layer values (equation 5.12). This parameterises the effect of an increase in velocity shear at the base of the mixed layer; if the mixed layer starts moving too quickly and becomes unstable, extra layers will be entrained. The critical bulk Richardson number is 0.65 (Price *et al.*, 1978), determined from field and laboratory experiments. If the calculated bulk Richardson number is less than this value, the

MLD in the model will increase.

$$Ri_{\mathrm{B}} = \frac{g\ h\ \Delta\sigma_\theta}{\sigma_\theta\ (\Delta V)^2} \geq \quad 0.65. \tag{5.12}$$

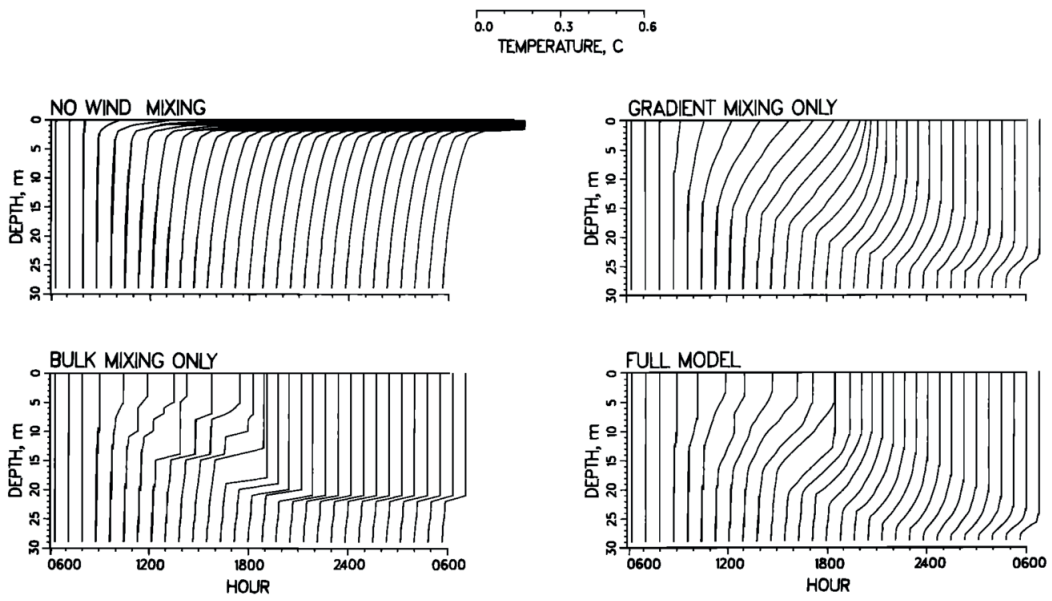

Figure 5.3: Figure 10 from Price et al. *(1986). This shows a PWP model run over a 24 hour period with varying mixing parameterisations. It is evident that without gradient or bulk Richardson number mixing the mixed layer is purely defined by surface heating, whilst gradient mixing causes a smoother profile than bulk mixing alone.*

The gradient Richardson number (equation 5.14) is a dimensionless ratio between the square of the buoyancy frequency (or Brunt-Väisälä frequency, N; equation 5.13) and the square of the vertical shear of horizontal velocities. It parameterises the mixing that occurs when the velocity gradient across two layers (typically across the base of the mixed layer) becomes too great. This process is what sets the PWP model apart from other bulk mixed layer models, and helps to create the thermocline structure. The value at which this mixing occurs – called the critical gradient Richardson number ($Ri_{\mathrm{G,c}}$) – was determined through laboratory experiments in the 1960s (Miles, 1961; Howard, 1961) as 0.25. More recent studies suggest that turbulent mixing (mainly driven by internal waves) can continue to occur in layers with $Ri_{\mathrm{G}} > 1$ (Galperin *et al.*, 2007). For this study, we use $Ri_{\mathrm{G,c}} = 0.25$, and include turbulence

from internal wave breaking within the background diffusion (K, see below).

$$N \equiv \sqrt{-\frac{g}{\sigma_\theta}\frac{\Delta\sigma_\theta}{\Delta z}}. \tag{5.13}$$

$$Ri_{\mathrm{G}} = \frac{g\ \frac{\Delta\sigma_\theta}{\Delta z}}{\sigma_\theta\ \left(\frac{\Delta V}{\Delta z}\right)^2} \geq \quad 0.25, \tag{5.14}$$

where $\Delta\sigma_\theta, \Delta V$ or Δz is the difference in those variables between two adjacent layers. When the calculated gradient Richardson number drops below its prescribed critical value ($Ri_{\mathrm{G,c}}$), mixing will occur between two adjacent layers, and will be repeated until the local Richardson number returns to the critical value.

The effect of including the bulk and gradient Richardson number mixing schemes can be seen in Figure 5.3 (from Price *et al.*, 1986). This shows that the gradient Richardson number mixing causes a smoothing of the transition between the mixed layer and the level below, which is unrealistically sharp when bulk Richardson number mixing alone is used.

Finally, an overall background diffusion is applied to the whole water column (equation 5.15, parameterised in the model as equation 5.16), where χ represents the property (T, S, u, v) being diffused.

$$\frac{d\chi}{dt} = K\frac{d^2\chi}{dz^2}, \tag{5.15}$$

$$\chi_k = \chi_k + \frac{\Delta t}{\Delta z^2}\ K\left(\chi_{k+1} - 2\chi_k + \chi_{k-1}\right). \tag{5.16}$$

All of the processes that occur in one time-step of the PWP model can be seen schematically in Figure 5.4.

5.3 Set up of the PWP model

The set up of the PWP model requires meteorological forcing, including heat and freshwater fluxes, and an initial ocean profile of temperature and salinity. The me-

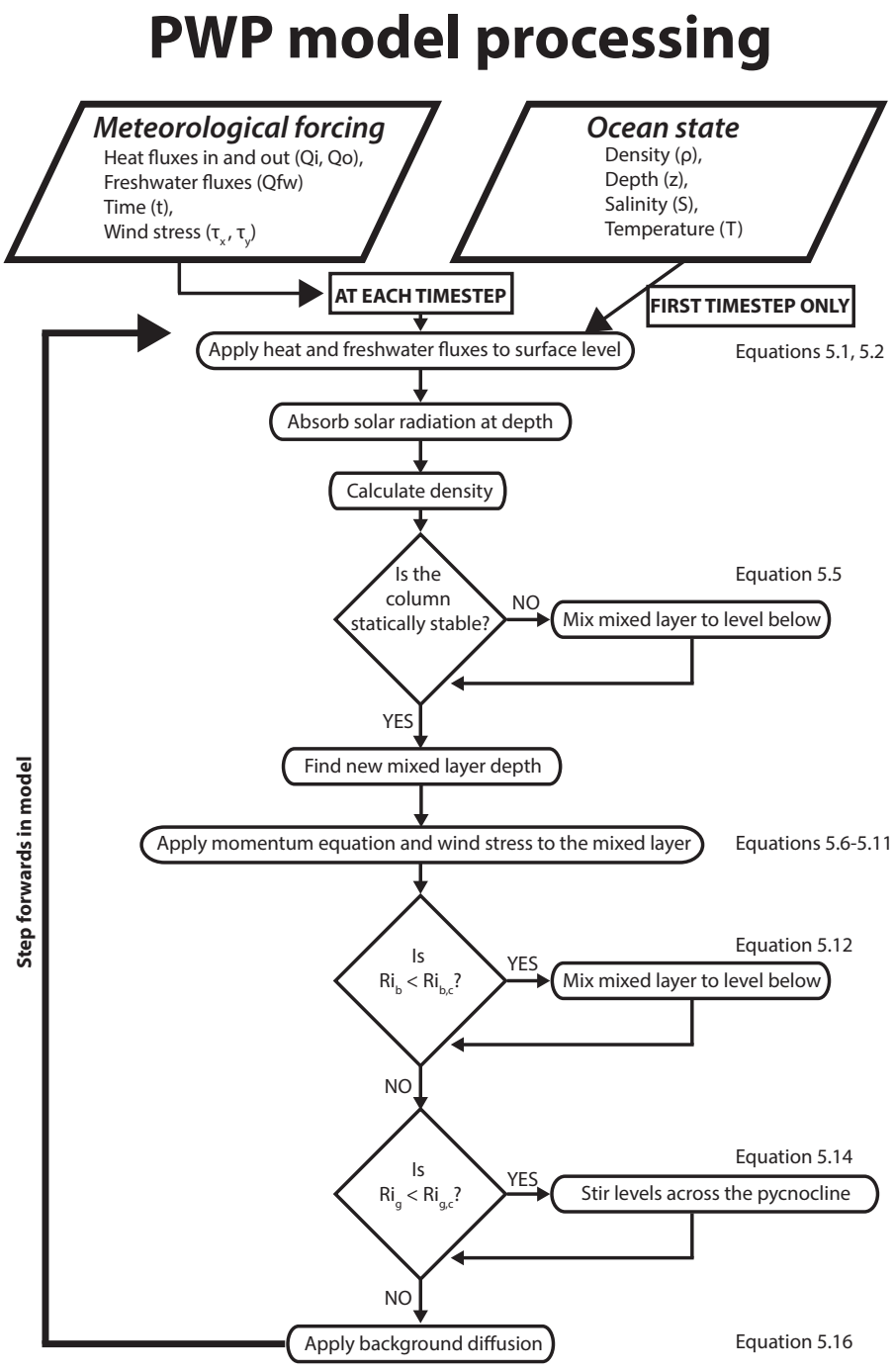

Figure 5.4: Flowchart showing the processes within the PWP model (Matlab code; Lazarevich and Stoermer, 2001).

teorological data are then interpolated to the time intervals prescribed for that model run, and applied at each time-step of the model run. The initial ocean profile is interpolated to the depth intervals used, and only used for the first time-step.

As the purpose of the model is to investigate the effect of various ocean processes, a climatological dataset of surface fluxes from the continental shelf of the Amundsen Sea is used, and repeated annually. This means that whilst the meteorological input is appropriate for the Amundsen Sea region, it is the same year on year, removing any variability in the water column due to climatic interannual variability. The climatology used is averaged from the 32-year long National Centers for Environmental Prediction (NCEP) – Climate Forecast System (CFS) v1 atmosphere reanalysis (Saha *et al.*, 2006), as used by Petty *et al.* (2013). the ergion that the climatology data is taken from can be seen in Figure 1 of Petty *et al.*. The dataset is 6 hourly and includes air temperature (T_{air}, 2 m), specific humidity (q, 2 m), precipitation (p), incoming shortwave radiation (Q_{i}), incoming longwave radiation ($Q_{\mathrm{lw,net}}$), and windspeed (U; Figure 5.5). As PWP requires latent and sensible heat fluxes, initially a constant surface ocean temperature was used to calculate these variables, but this was later developed to vary at each time-step (see section 5.4).

The initial ocean profile used was based on CTD 22 in Pine Island Bay in the Amundsen Sea (Figure 5.6). The CTD data consisted of temperature, salinity, depth and potential density, all at 2 m intervals (Figure 5.6a). This CTD station is representative of the water column on the shelf in the Amundsen Sea, with the colder and fresher WW overlying the warmer and saltier mCDW. The profile was used to set the initial endpoints of three of the main water masses (AASW, WW and UCDW), creating a new profile with linear mixing lines between these endpoints (Figure 5.6b). UCDW was used rather than LCDW so that the effects of switching from a warm end-point to a cooler end-point (such as UCDW to LCDW) could be observed.

Two other parameters can affect the model runs: the increments for time and depth (Δt and Δz). The vertical resolution is important if we are concerned with

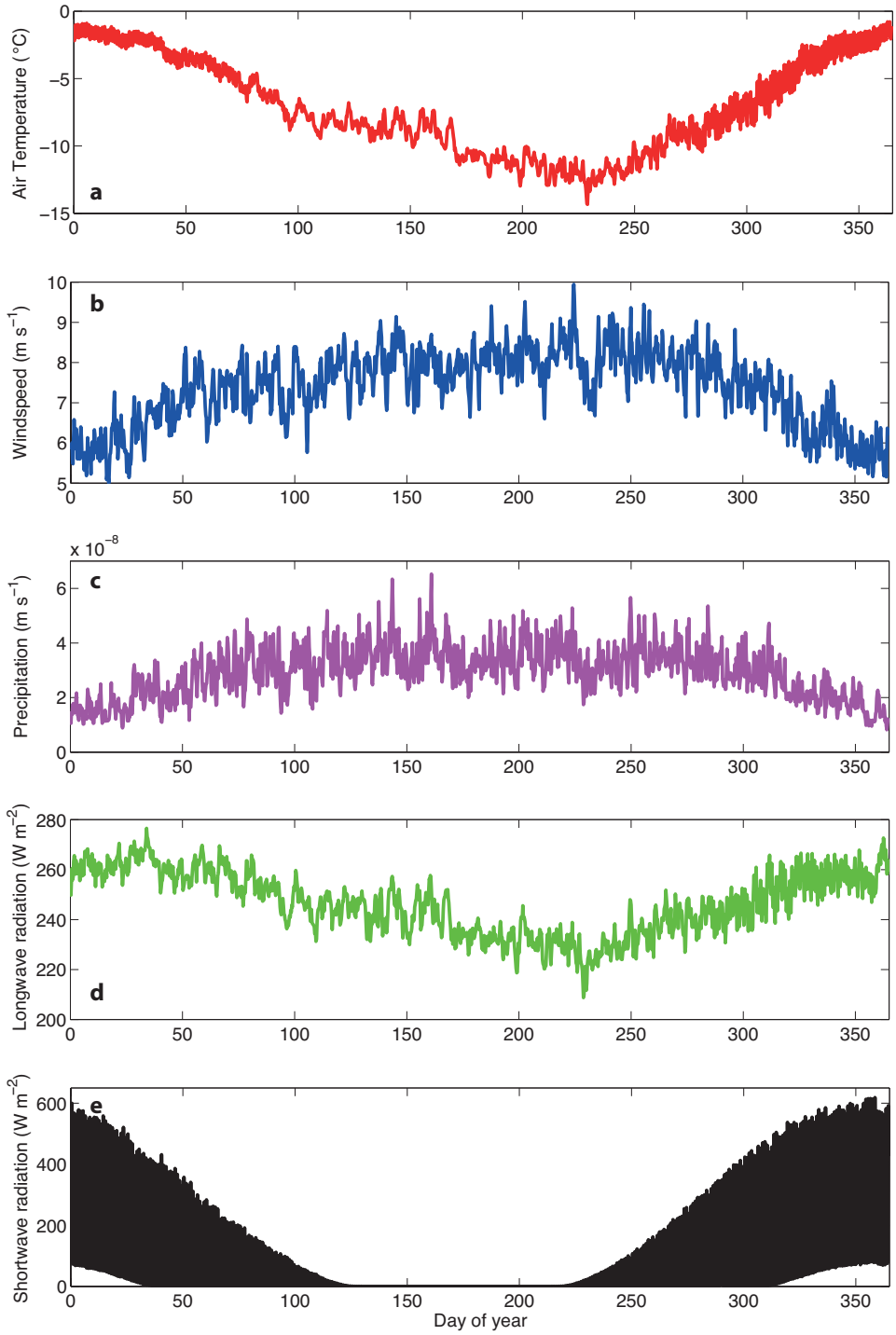

Figure 5.5: NCEP-CFS 6-hourly climatology data for the Amundsen Sea, showing an annual cycle of (a) Air temperature (2 m), (b) Windspeed (10 m), (c) Precipitation, (d) Net longwave radiation, (e) Shortwave radiation.

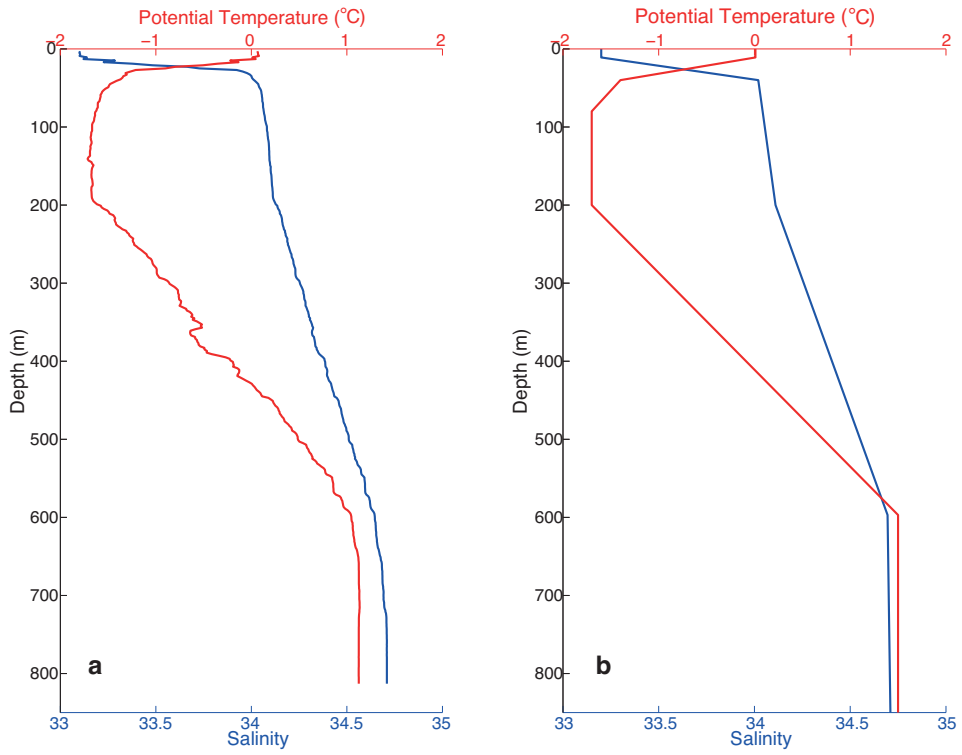

Figure 5.6: CTD profiles showing potential temperature (red) and salinity (blue) for (a) CTD 22, real data from Amundsen Sea and (b) Linearised profile used in the PWP model. The temperature is warmer at depth in (b) so that variations in mCDW (between UCDW and LCDW) could be modelled.

resolving thin surface layers, and the combination of temporal and vertical resolution will affect how diffusion is represented in the model, as the Courant-Friedrichs-Lewy condition must be taken into account (CFL; Courant *et al.*, 1967). The CFL condition states that a finite difference formula (such as the one used within the model for diffusion, equation 5.16) can only be stable if its numerical domain of dependence is at least as large as the resolution of the model; i.e. the diffusion must reach no further than the next grid cell in the time-step given. Price *et al.* (1986) use a very high vertical resolution of 0.5 m and a time-step of 900 s for their tropical mixed layer model, which is focused on the top 40 m of the water column over a diurnal cycle.

5.4 Modifications to the PWP model

In order to adapt the model for use in the Amundsen Sea, several changes were made – both to initial forcing inputs and fundamental equations within the model. The model is not intended to replicate 'real-life' conditions, but should include the basic processes that influence the water column in this region. This means that whilst we attempt to replicate the WW seasonal cycle and the mixing between WW and mCDW, the exact temperature, and depth are not expected to match the observations. This modified PWP model will be referred to as 'mPWP'.

5.4.1 Latent and sensible heat fluxes

The calculation of the latent and sensible heat fluxes was incorporated into the model, so that the changing ocean surface temperature could be used. The heat and freshwater fluxes are now all calculated based on the surface conditions of the ocean for that time-step. The outgoing heat flux (Q_o) consists of the sensible and latent heat fluxes (Q_{sens} and Q_{lat}), as well as the longwave radiative flux ($Q_{lw,net}$; equations 5.19 - 5.22). In order to calculate these, the saturated vapour partial pressure (e_w, measured in Pa; WMO, 2008) and saturated humidity (q_{sat}; Gill, 1982) must be calculated:

$$e_w = 100 \times 6.112 \; e^{\frac{17.62 T_1}{243.12 + T_1}}, \tag{5.17}$$

$$q_{sat} = \frac{\epsilon_r \; e_w}{P_{atm} - (e_w(1 - \epsilon_r))}, \tag{5.18}$$

where ϵ_r is the ratio of molecular mass of water and dry air, P_{atm} is the atmospheric pressure at the ocean surface (in Pa). These values can then be used to calculate the outgoing fluxes (equations 5.19-5.21; Parkinson and Washington, 1979).

$$Q_{lw,net} = \epsilon_{lw} \; \sigma \; (T_1 + 273)^4 - \epsilon_{lw} \; Q_{lw,in}, \tag{5.19}$$

$$Q_{sens} = \rho_a \; c_a \; C_d \; U \; (T_1 - T_{air}), \tag{5.20}$$

$$Q_{\text{lat}} = \rho_{\text{a}}\ L_{\text{v}}\ C_{\text{d}}\ U\ (q_{\text{sat}} - q). \tag{5.21}$$

In these equations, ϵ_{lw} is the longwave emissivity of water, σ is the Stefan-Boltzmann constant, ρ_{a} is the density of air, c_{a} is the specific heat capacity of air, C_{d} is the drag coefficient and L_{v} is the latent heat of vaporisation. Together, these heat fluxes can be used to provide the outgoing heat flux (Q_{o});

$$Q_{\text{o}} = Q_{\text{lw,net}} + Q_{\text{sens}} + Q_{\text{lat}}. \tag{5.22}$$

The freshwater flux is simply evaporation minus precipitation (equations 5.23-5.24), using the density of freshwater (ρ_{fw}) to calculate evaporation.

$$E = \frac{Q_{\text{lat}}}{\rho_{\text{fw}} L_{\text{v}}}, \tag{5.23}$$

$$Q_{\text{fw}} = E - p. \tag{5.24}$$

5.4.2 Simple sea ice model

As PWP was not originally designed to model freezing temperatures, it has no way of allowing for surface freezing and sea ice production during winter months. To prevent unrealistically low ocean temperatures (< -2 °C; Figure 5.7a), a simple sea ice model is used. It is entirely based on a basic thermodynamical sea ice model, using the difference between the temperature of the surface of the ocean and the freezing temperature (T_{fp}; Fofonoff and Millard, 1983) to calculate a melt rate (m; equation 5.25) of sea ice. This melt rate is then used to calculate a thickness of sea ice (h_{i}; equation 5.26) – the melt rate is multiplied by the mixed layer depth (h) as the bulk mixed layer model prescribes all changes to happen over the length scale of the mixed layer. Finally, a concentration of sea ice is assigned. Rather than using wind stress and melt rates to calculate a theoretical sea ice concentration, one of two

values is assigned depending on whether the sea ice is growing or melting (A_{grow} or A_{melt}; equation 5.27). These values are used as broadly representative of the values for sea ice concentration seen in Figure 1.4. The assigned concentration is lower during periods of sea ice melt as a simple parameterisation of advection of sea ice out of the model domain.

$$m = \frac{\sigma_{\theta 1}}{\rho_{\text{fw}}} \frac{c_{\text{w}}}{L_{\text{f}}} (T_1 - T_{\text{fp}}) \frac{1}{\Delta t}, \tag{5.25}$$

$$h_{\text{i}} = h_{\text{i}} - m\, h\, \Delta t, \tag{5.26}$$

$$A_{\text{grow}} = 0.77, \qquad A_{\text{melt}} = 0.6, \tag{5.27}$$

where L_{f} is the latent heat of fusion. When sea ice is present, the mixed layer temperature is set to the freezing point and the mixed layer salinity is affected by the growth of the sea ice (equations 5.28-5.29). The sea ice salinity is set to zero for simplicity.

$$T_k = T_{\text{fp}}, \tag{5.28}$$

$$S_k = \frac{S_k}{1 + (A\ m)}, \tag{5.29}$$

for $(k-1)\Delta z < h$.

On the next time-step, the atmosphere-ocean heat and freshwater fluxes are reduced by the concentration of the sea ice (1-A), simulating a cover on the fraction of the ocean surface where sea ice is present (equations 5.30-5.31).

$$T_1 = T_1 + [1 - A] \frac{(Q_{\text{i}}\ \alpha_1 - Q_{\text{o}})}{\sigma_{\theta 1}\ c_{\text{w}}} \frac{\Delta t}{\Delta z}, \tag{5.30}$$

$$S_1 = \frac{S_1}{1 - [1 - A]\, Q_{\text{fw}}\ \left(\frac{\Delta t}{\Delta z}\right)}, \tag{5.31}$$

Whilst this is a simplistic sea ice model, our mPWP model is aimed at recreating the physical processes of the water column, rather than an exact replica of reality. When sea ice is present, it forms a partial cap to the ocean, and by reducing the

air-sea fluxes in proportion with the concentration of sea ice we are using a crude parameterisation of true air-sea ice-ocean processes. Therefore, we believe that this is a suitable method to use for this case study.

Including this sea ice parameterisation allows reasonable ocean temperatures throughout the winter season (Figure 5.7b), whereas without it unreasonably low surface temperatures appeared (Figure 5.7a).

5.4.3 Buoyancy and wind forced mixing parameterisations

With these modifications made, the sea ice production maintains reasonable winter temperatures, and the depth of the mixed layer increases during sea ice growth due to the cold (freezing point), salty water (here called WW*) produced. However, the way that the PWP model sets the mixed layer depth (excluding any direct buoyancy forcing) makes it hard for it to shoal again in the following summer, and each winter, the mixed layer depth rapidly descends again. Eventually, this results in the mixed layer depth descending below the domain of the model, causing the model to stall (Figure 5.7b). This is due to the main controls on the mixed layer depth being the stability criteria outlined in section 5.2, and so there is minimal (or no) effect caused by buoyancy (or stratification). The model requires better parameterisation of these detrainment processes in order to combat this deep mixed layer.

To fix this, the parameterisation of buoyancy and wind driven mixing needs to be improved. The Kraus-Turner parameterisation of TKE budgets was used (as discussed in Section 5.2) to include buoyancy forcing and surface fluxes of TKE. These are used to calculate the vertical entrainment velocity for the base of the mixed layer, which will determine whether it shoals or deepens (Kraus and Turner, 1967; Niiler, 1975; Niiler and Kraus, 1977). This requires recalculation of the new freshwater fluxes (after sea ice growth or melt is taken into account, F_{fw}; equation 5.32),

$$F_{\mathrm{fw}} = S_1 \left((1 - A)\ Q_{\mathrm{fw}} - A\ m\left(\frac{\Delta z}{\Delta t}\right)\right), \tag{5.32}$$

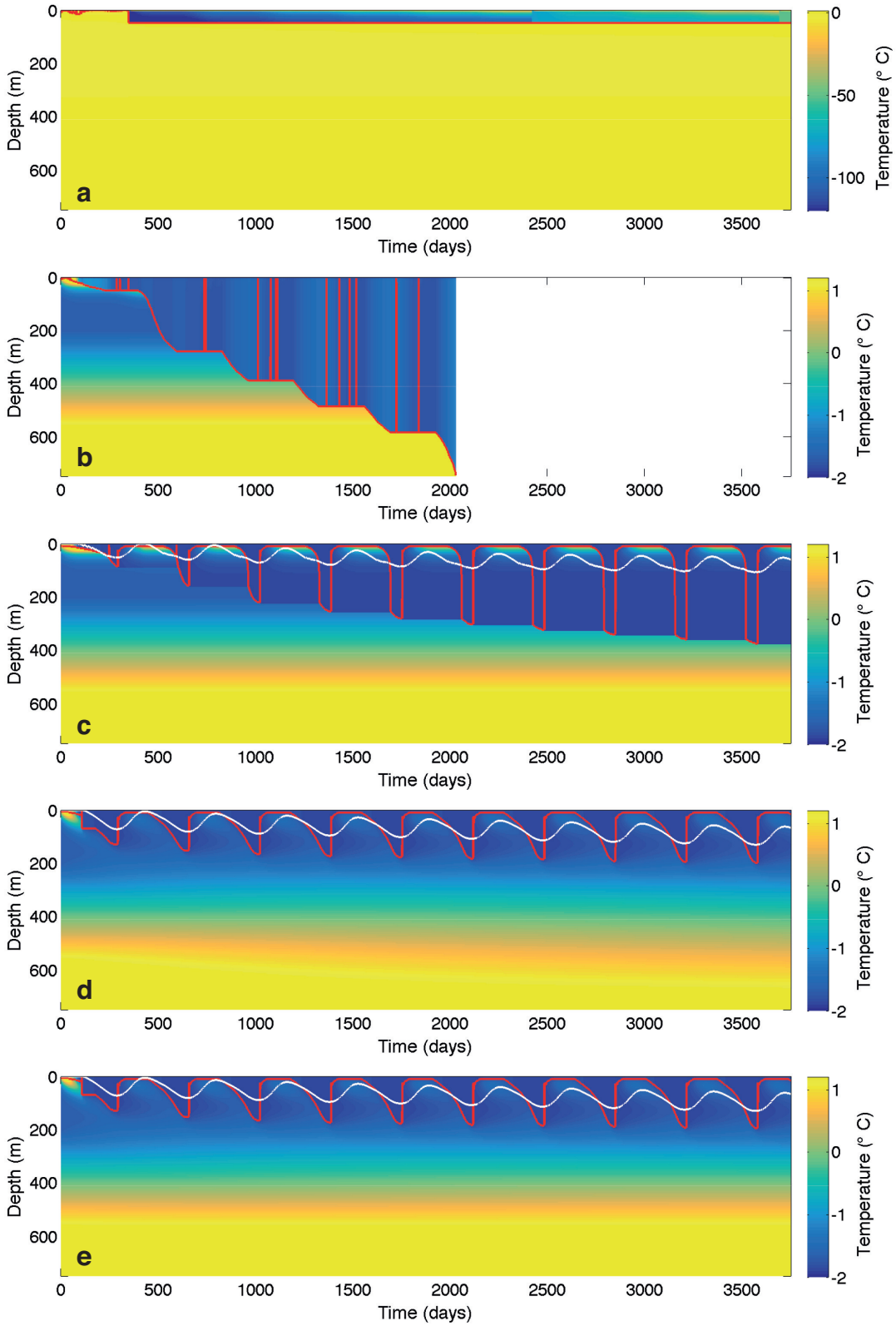

Figure 5.7: Time-series plots of θ from stages of the mPWP development, with the mixed layer depth plotted on as a red line, and the sea ice thickness multiplied by 50 plotted on as a white line. (a) shows the original PWP model with no sea ice processes in, (b) is the mPWP with sea ice processes, (c) is with added Kraus-Turner mixing parameterisation, (d) is with increased diffusion and (e) is with advection.

as well as calculating the power supplied for mixing by wind stresses (P_{w}; equations 5.33 - 5.34),

$$U_* = U \sqrt{\frac{\rho_{\mathrm{a}}}{\rho_{\mathrm{w}}} C_{\mathrm{d}}}, \tag{5.33}$$

$$P_{\mathrm{w}} = 2 m_{\mathrm{kt}} \, e^{-\frac{h}{z_{\mathrm{w}}}} \, {U_*}^3, \tag{5.34}$$

where U_* is the friction velocity, m_{kt} is the coefficient for power provided by wind and z_{w} is the dissipation length scale. Buoyancy fluxes must also be calculated (P_{b}; equations 5.35 - 5.36).

$$B = \left(\frac{g \, \alpha_{\mathrm{T}}}{\rho_{\mathrm{w}} \, c_{\mathrm{w}}} \, (Q_{\mathrm{o}} - 0.45 Q_{\mathrm{i}}) \right) - g \, \beta \, F_{\mathrm{fw}}, \tag{5.35}$$

$$P_{\mathrm{b}} = \frac{h}{2} \, \left(B \, (1 + n_{\mathrm{kt}}) - |B| \, (1 - n_{\mathrm{kt}}) \right), \tag{5.36}$$

where B is the buoyancy term, α_{T} is the thermal expansion coefficient, β is the salinity contraction coefficient and n_{kt} is the coefficient for power provided by buoyancy. The vertical entrainment (w_{e}) is then calculated as a balance between the power for mixing provided by the wind and buoyancy forcing, and the gravitational stability of the column (equation 5.37).

$$w_{\mathrm{e}} = \frac{P_{\mathrm{w}} + P_{\mathrm{b}}}{h \, [g \, \alpha_{\mathrm{T}} \, (T_1 - T_k) - g \, \beta \, (S_1 - S_k)]}, \tag{5.37}$$

for $(k-1)\Delta z = h+1$. If the vertical entrainment is positive, the new mixed layer depth is adjusted by:

$$\Delta h = w_{\mathrm{e}} \, \Delta t, \tag{5.38}$$

and is recalculated until the increase in mixed layer depth is smaller than the grid cell. However, if the vertical entrainment is negative, then the new (shallower) mixed layer depth is calculated by balancing the wind mixing (P_{w}) with the buoyancy (B);

$$h = \frac{P_{\mathrm{w}}}{-B}. \tag{5.39}$$

This new mixed layer is then homogenised (as is required in a bulk mixed layer model) by mixing all of the properties within the layer. This inclusion of Kraus-Turner type mixing provides a more realistic development of the mixed layer depth, allowing both deepening and shoaling (Figure 5.7c).

5.4.4 Diffusion

The downloaded Matlab script (Lazarevich and Stoermer, 2001) did not effectively parameterise diffusion and so there was minimal effect from this term on the water column. To ensure that diffusion was applied within the model, equation 5.16 was included at the start of each time-step. The resulting change within the water column was noticeable (cf. Figure 5.7c and 5.7d).

Analysis of the Ocean2ice temperature and salinity observations using the Turner angle (Turner, 1973) can help to identify regions of diffusive mixing. The Turner angle uses the gradients of temperature or salinity with depth to calculate which property is controlling the stability of the water column, and the likelihood of instabilities or diffusive mixing (Turner, 1973; You, 2002; equation 5.40).

$$Tu = \tan^{-1}\left(\frac{\alpha_{\mathrm{T}}\partial_{\mathrm{z}}T + \beta\partial_{\mathrm{z}}S}{\alpha_{\mathrm{T}}\partial_{\mathrm{z}}T - \beta\partial_{\mathrm{z}}S}\right). \tag{5.40}$$

In Figure 5.8, there are large areas dominated by diffusive mixing across the Amundsen Sea shelf, especially associated with the thermocline (typically found below $\sigma_\theta = 27.6$; Chapter 3). Due to this, the background diffusivity (K) was increased from 10^{-5} m^2 s^{-1} (on initial runs; based on Munk and Wunsch, 1998) to 10^{-4} m^2 s^{-1}. This value of K applied to temperature and salinity (and so is referred to as $K_{T,S}$). Whilst included under 'diffusion', the transfer of momentum through the water column can be linked to eddy viscosity, and so for u and v a different value of K is used ($K_{u,v} = 5 \times 10^{-4}$ m^2 s^{-1}). This increased diffusion is an important process to include in the Amundsen Sea model, as once it was included the water column

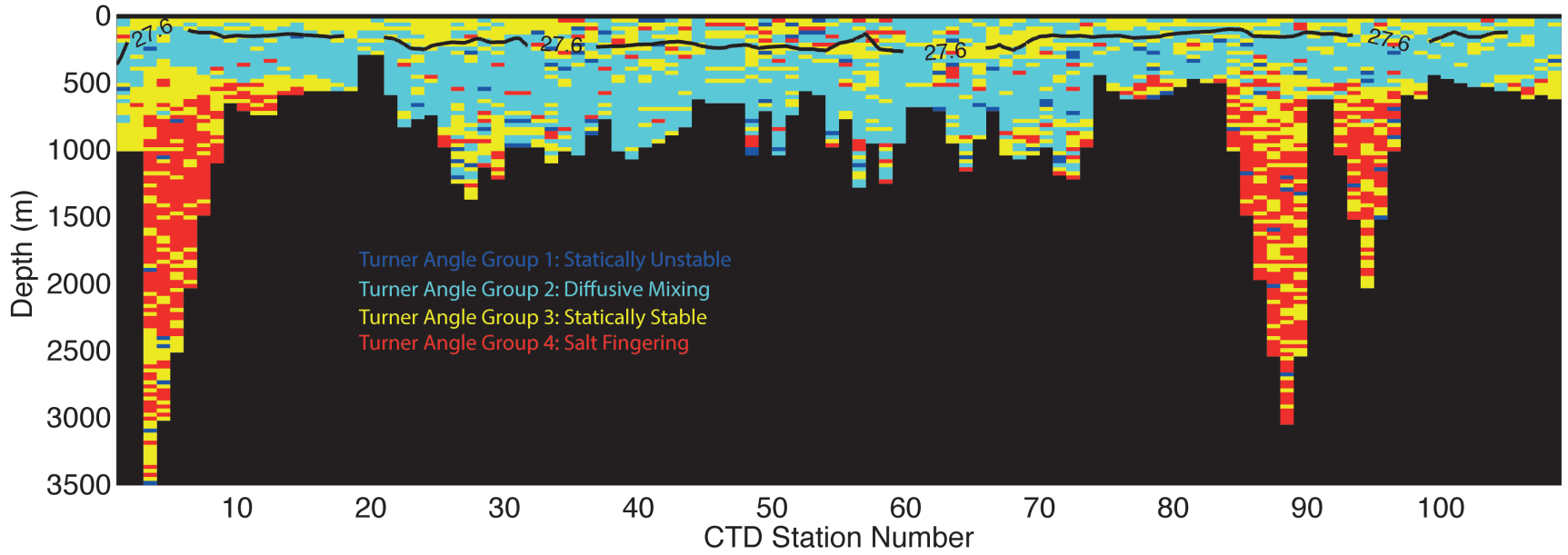

Figure 5.8: Turner angle groups from all CTD stations during the Ocean2ice cruise, smoothed to 25 m intervals. The Turner angle is derived from the ratio of stability from temperature to stability from salinity and tells us how likely the water column is to mix, and by what form of mixing. There are 4 main groups; (1) Turner angle is $-180°$ *to* $-90°$ *or* $90°$ *to* $180°$*: statically unstable; (2) Turner angle is* $-90°$ *to* $-45°$*: diffusive convection; (3) Turner angle is* $-45°$ *to* $45°$*: statically stable; (4) Turner angle is* $45°$ *to* $90°$*: salt fingering. This figure shows that the WW and mCDW water masses mix mainly through diffusive convection in the Amundsen Sea.*

followed an annual cycle after a 5 year spin up (Figure 5.7d). This provided a consistent mixed layer depth between winters, which was expected with a repeated annual climatology forcing the model.

5.4.5 Relaxation of the ocean column at depth

Without any replenishment of the mCDW at the base of the water column, the warm waters are gradually eroded by the cold WW* formed each season (Figure 5.7d). In reality, the mCDW is supplied to the Amundsen Sea by advection from cross-shelf transport, and there are no processes within the model that could replicate this. To rectify this, a one-dimensional advection analogue is introduced, which relaxes the ocean profile back to its original conditions (χ_{init}) below the depth that CDW was generally observed at during Ocean2ice (597 m; Figure 5.7e). This follows the equation:

$$\chi_k = \chi_k - V_{\text{adv}} \ (\chi_k - \chi_{\text{init},k}) \ \frac{\Delta t}{\Delta x}. \tag{5.41}$$

The values used for Δx (10 km) and advective current speed (V_{adv}; 0.01 m s^{-1}) in equation 5.41 are based on approximate orders of magnitude from observations, but are also fitted to the model runs used in this study. This ensures that the 'advection' is constant and the mCDW layer does not diffuse away.

The advective current velocity (V_{adv}) does not vary in time, and only applies below the depth where we consistently see mCDW in CTD profiles from the Amundsen Sea. This means that any changes higher up in the water column can affect the mixing line between WW* and mCDW, whilst ensuring the warm base of the water column remains.

The effect of including this 'advection' can be seen between Figure 5.7d and 5.7e.

5.5 Addition of dissolved oxygen to the model

The meltwater calculation includes dissolved oxygen as a conservative tracer, but within this study we have already identified areas of biological productivity (Section 3.7 and Chapter 4), where dissolved oxygen concentrations have been locally enhanced. This increase in dissolved oxygen would cause a false decrease in meltwater fractions, but equally a decrease in dissolved oxygen – caused by respiration – would result in an apparent increase in meltwater fractions. This has been suggested as a possible process for the curvature observed in c(O_2)-S_A figures from the Amundsen Sea (Section 3.6.2). In order to explore this hypothesis further, dissolved oxygen must be added to the mPWP model. It is included in the initial ocean profile, based on the CTD 22 values (Figure 5.9). Similarly to the temperature profile, UCDW values of dissolved oxygen are used rather than LCDW. This section describes the way that dissolved oxygen is added, including both physical and biological processes.

5.5.1 Physical processes

The exchange of dissolved oxygen between the atmosphere to the ocean is strongly influenced by windspeed, as greater windspeeds will result in greater turbulence and shear at the atmosphere-ocean boundary layer (Wanninkhof, 2014). Whilst the windspeed controls the rate of gas exchange, the overall amount of oxygen that can be absorbed by the ocean is limited by surface saturation and the amount of bubbles present. The saturation value varies with temperature and salinity, as colder and fresher water can absorb more oxygen than water that is warmer and more saline.

To model this process, the updated gas transfer velocity equation from Wanninkhof (2014) is used (equation 5.43). This equation is generic to all soluble gases, and the Schmidt number (Sc; equation 5.42) is used to make the equation specific to the gas of interest – taking into account the molecular diffusivity of the gas and the

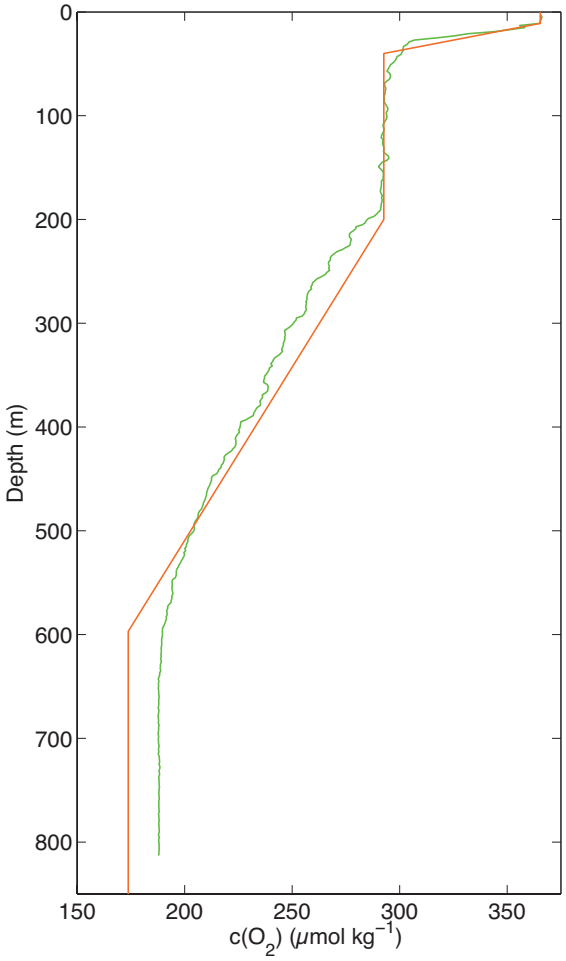

Figure 5.9: CTD profiles showing CTD 22 dissolved oxygen ($c(O_2)$) data from the Amundsen Sea (green) and the linearised profile used in the mPWP model (orange). The $c(O_2)$ is lower at depth in the mPWP profile so that variations in mCDW (between UCDW and LCDW) could be modelled.

thickness of the atmosphere-ocean boundary layer (or its kinematic viscosity).

$$Sc = \frac{\nu}{D}, \tag{5.42}$$

$$k = 1.791 \times 10^{-5} U^2 (Sc)^{-0.5}, \tag{5.43}$$

where ν is the kinematic viscosity of the ocean surface, D is the molecular diffusivity of oxygen, Sc is a unitless number and k is measured in m s^{-1}. This velocity is then

applied to the dissolved oxygen concentrations ($c(O_2)$) as:

$$\Delta\, c(O_2) = -\left(k\ (c(O_2)_s - c(O_2)_{sat})\ \frac{\Delta t}{h}\right), \tag{5.44}$$

where $c(O_2)_s$ is the surface value of dissolved oxygen, and $c(O_2)_{sat}$ is the saturation value for the surface temperature and salinity. The change in dissolved oxygen is positive out of the ocean.

The exchange of dissolved oxygen between the atmosphere and ocean will be affected by the presence of sea ice. Not only will the sea ice provide a barrier between the two reservoirs, but it will also affect the gas exchange velocity. Under partial ice cover, the wind has a shorter fetch to produce the roughness on the sea surface that will encourage gas transfer. Recent laboratory experiments showed that in sea ice cover of 85 %, the gas transfer velocity was reduced to just 25 % of its original value (Loose *et al.*, 2009b). This reduction is used in the mPWP model when sea ice is present. As background diffusion has already been introduced into the mPWP, the eddy diffusivity for dissolved oxygen was set to the same value as temperature and salinity ($K_{T,S}$). Similarly, dissolved oxygen concentrations are relaxed back to the initial profile values at the same rate as temperature and salinity.

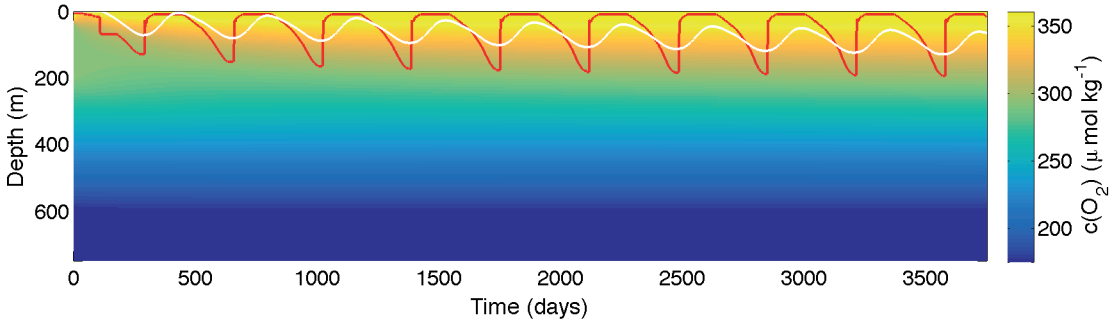

Figure 5.10: Time-series of dissolved oxygen ($c(O_2)$) with physical processes applied in the mPWP model, with mixed layer depth plotted as a red line and the sea ice thickness (multiplied by 50) plotted as a white line.

The resultant dissolved oxygen time series can be seen in Figure 5.10. There is minimal seasonal variability, and this is likely due to the almost constant presence of

sea ice – and therefore constant surface saturation values – in the mPWP model. The model does not include transfer of oxygen through bubble entrainment, or account for solute rejection during sea ice formation. When sea ice is present, the former process is likely to be minimal, due to the shorter fetch available to the wind in order to stir up the surface waters. Loose *et al.* (2009b) suggest that solute rejection may only constitute 5 % of the change in dissolved oxygen concentration when sea ice is present, with the exchange between atmosphere-ocean through leads in the sea ice playing a more important role in the gas transfer. Future development of the model would benefit from parameterisations of these processes for completeness. In addition to these processes, the lack of biological activity may also play a role in the minimal change in dissolved oxygen concentration over the 10 years of the model run.

5.5.2 Biological processes

Within the ocean reservoir, biological productivity and respiration are the main causes for changes in dissolved oxygen concentration. Biological productivity will influence the top 80 m of the water column (based on depth where 1% of light levels reach, Figure 5.2), whilst respiration can occur throughout the entire water column. Previous studies using PWP have used biological fluxes estimated from Argo floats to construct a Net Community Production (NCP) profile of the water column (Martz *et al.*, 2008). NCP is calculated as the difference between the gross primary productivity (which increases dissolved oxygen concentrations) and the community respiration (which decreases dissolved oxygen concentrations). A negative NCP rate indicates respiration rates are higher than productivity rates, and so the overall dissolved oxygen concentration will decrease. This profile can then be applied at each time-step, reducing (or increasing) the dissolved oxygen concentration by the NCP that occurred during that time.

In the Amundsen Sea, there are few studies of NCP rates (Hahm *et al.*, 2014;

Ducklow *et al.*, 2015). Hahm *et al.* (2014) use ΔO_2/Ar ratios to calculate the NCP rates, but do not correct for entrainment from the atmosphere, which can have a large impact on the magnitude and sign of NCP rates (Castro-Morales and Kaiser, 2013). Ducklow *et al.* (2015) use a sediment trap at 350 m to estimate the NCP rates in the layers above (split into 0-50, 50-100 and 100-350 m sections), finding NCP rates of approximately 56 mmol m^{-2} d^{-1} in the top 50 m (equates to approximately 1 μmol kg^{-1} d^{-1}) . Both of these studies are from the Amundsen Sea Polynya, which is located to the west of the region that the Ocean2ice measurements are from, and believed to be one of the most productive regions in Antarctica (Arrigo *et al.*, 2012; Yager *et al.*, 2012). This high productivity means that the NCP rates reported from this area are likely to be higher than those in the eastern Amundsen Sea, which is the area of interest for this thesis.

Most of the interest in primary productivity and NCP rates are concerned with surface values, as this is where biological activity can interact with, and influence, the carbon cycle (Duprat *et al.*, 2016). Due to this, values below the mixed layer are rarely measured or reported. The lack of this information will limit how 'realistic' the biological model can be in the mPWP. The model would benefit from further development to improve this, as well as additional measurements of $c(O_2)$ and CFC or SF_6 concentrations from the Amundsen Sea region in order to calculate respiration rates at depth. Instead, the NCP profile for this model is estimated based on the Martz *et al.* (2008) study in the South Pacific, and shown in Figure 5.11. The region of net productivity (approximately the top 80 m) is described by a half cosine curve, and is at a maximum at the surface (NCP of 4.8×10^{-2} μmol kg^{-1} d^{-1}). After crossing the line where NCP is equal to 0 μmol kg^{-1} d^{-1}, the NCP profile linearly decreases to 130 m where the maximum net respiration is found (NCP of -8.4×10^{-3} μmol kg^{-1} d^{-1}). The net respiration decreases (i.e. NCP increases towards zero) according to a Martin power function curve (Martin *et al.*, 1987) to a minimum net respiration at the bottom of the water column (NCP of -1.67×10^{-3} μmol kg^{-1} d^{-1}).

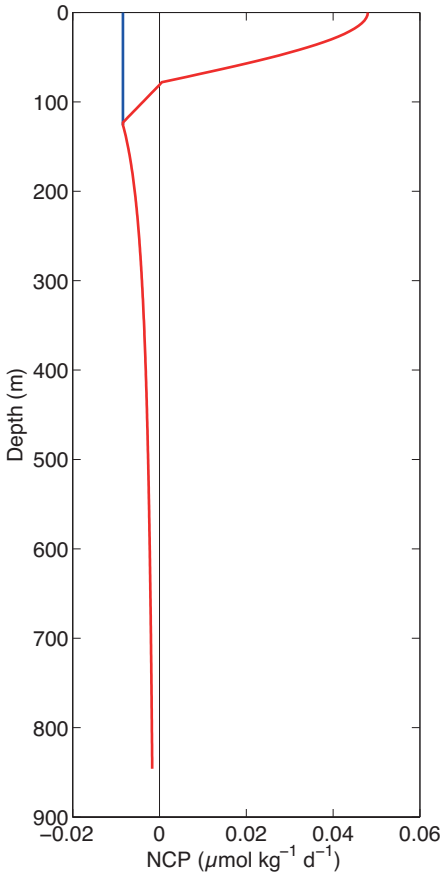

Figure 5.11: Profile of the Net Community Production (NCP; μmol kg^{-1} d^{-1}) used in the mPWP biological model. The red line shows the NCP profile for the summer months (when shortwave radiation is greater than 0), and the blue line shows the reduction in biological productivity at the surface in winter months (when shortwave radiation is 0).

The surface values of NCP are approximately 15-20 times smaller than those reported in Ducklow *et al.* (2015) and also in Chapter 4 (0.7 μmol kg^{-1} d^{-1}; Biddle *et al.*, 2015), where biological productivity was enhanced by the presence of an iceberg. Initial runs did use NCP values an order of magnitude greater (increasing both net production at the surface and net respiration at depth), but the effects of the respiration at depth were too great and resulted in a significant depletion of dissolved oxygen (Figure 5.12a). This is likely due to the limitations associated with a one-dimensional model, where parameterisations of processes such as eddy diffusivity and advection may be not be sufficient for modelling dissolved oxygen concentrations over a long period of time. To temporarily fix this, the NCP rates discussed above were used, resulting in only slightly depleted dissolved oxygen concentrations at depth after the

10 year model run (Figure 5.12b).

Biological productivity – and to a lesser extent respiration – will have a distinct seasonal cycle, as the phytoplankton and bacteria will be affected by light levels, availability of nutrients and water temperature. Ideally, in order to model this, time series data of oxygen and respiration rates (using CFC or SF_6 as tracers) below the mixed layer are required. As this information is currently lacking for the Amundsen Sea, no changes are made to the net respiration portion of the curve throughout the year. Through the austral winter, there is no sunlight and therefore no productivity can occur. The region of the water column where net productivity occurs in the summer is instead set to the maximum respiration rates during periods when shortwave radiation is zero (Figure 5.11).

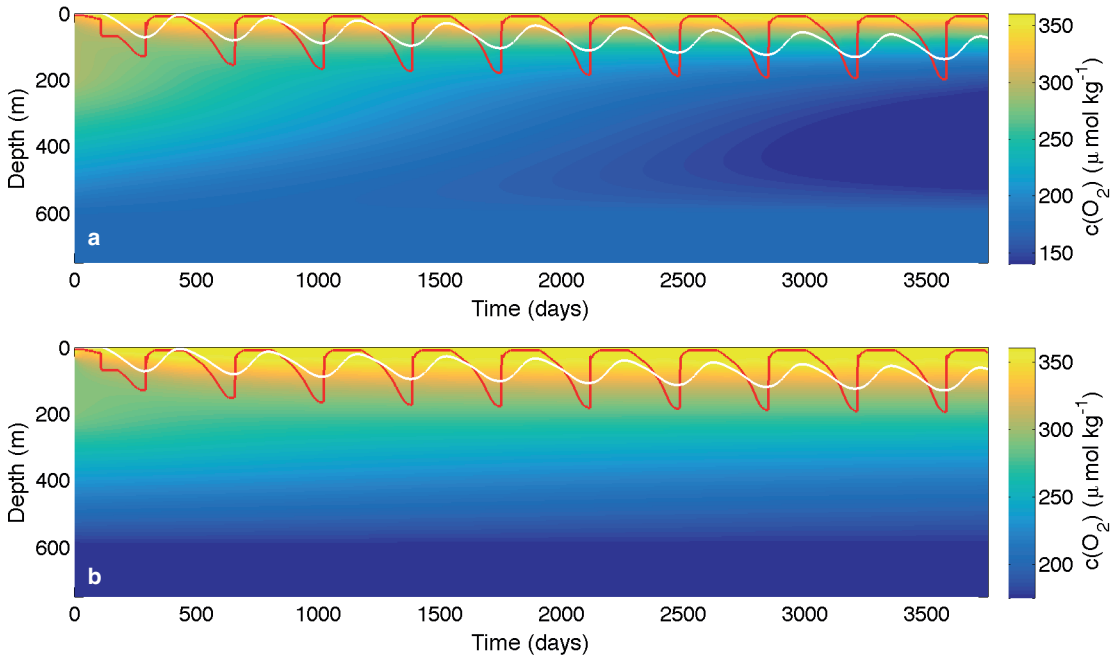

Figure 5.12: Time-series of dissolved oxygen ($c(O_2)$) with both physical and biological processes applied in the mPWP model, with mixed layer depth plotted as a red line and the sea ice thickness (multiplied by 50) plotted as a white line. (a) Shows the depletion of dissolved oxygen at depth with the initial NCP profile, whilst (b) shows the run using the final NCP profile (rates a magnitude lower than typical published values).

Although modifications of the NCP rates and improvements to the parameterisation of the oxygen fluxes are required, the addition of dissolved oxygen to the mPWP

model still provides a useful indication of how physical and biological processes may affect dissolved oxygen concentrations throughout the water column. The ability to separate the effects of biological and physical processes is especially useful for the simulations of the Amundsen Sea in order to identify the cause of the curvature seen in Chapter 3.

5.6 Application of the model

With the modifications that have been made to the original PWP, this mPWP model can now be used to run simulations of the Amundsen Sea, in order to assess the effects of different processes on the mixing line between mCDW and WW. A curvature was observed in this mixing line (Section3.6), and three alternative hypotheses were suggested as causes: variations in the CDW endpoint, variations in the WW endpoint, and biological activity. These processes will be tested using the mPWP model in this section, with the results highlighting the processes that result in the curvature seen. For all runs, the NCEP-CFS climatology described in Section 5.3 is used, and unless otherwise stated, the UCDW endpoint is used for mCDW.

5.6.1 Variations in the WW endpoint

In Chapter 3, it was suggested that a colder year than average will result in a more sea ice production, and so a more saline (and fractionally colder) WW endpoint. If the entire water column does not re-equilibrate with this new endpoint, or if there is horizontal advection of WW with different properties to the local WW, then the resulting mCDW-WW mixing line will display curvature (Figure 3.22).

The model was run for 10 years, with the NCEP-CFS climatology repeated each year. No biological processes were included in order to separate the effects of the variation in WW and biological activity on the dissolved oxygen. As the one dimensional model is unable to realistically advect sea ice from the domain, the model

grows more sea ice throughout the 10 year run, resulting in a more saline and slightly colder WW endpoint (WW′). This is the change in WW that we want to model, and so is left in the model.

Over the 10 year model run, in Θ-S_A space, the WW endpoint gradually shifts along the seawater freezing temperature line (grey lines; Figure 5.13a) towards the colder and more saline values (final profile, red line; Figure 5.13a). The final profile, after 10 years, shows clear curvature in the upper water column section of the mCDW-WW′ mixing line, with the base of the water column still displaying the linear mCDW-WW mixing line. In c(O_2)-S_A space, a curvature also forms over the 10 year model run, with the WW′ endpoint being a more saline but much higher dissolved oxygen concentration (Figure 5.13b). The dissolved oxygen concentration probably shifts to these much higher concentrations because of the lack of biological activity included in this simulation of the mPWP model, and therefore no respiration to reduce dissolved oxygen concentrations.

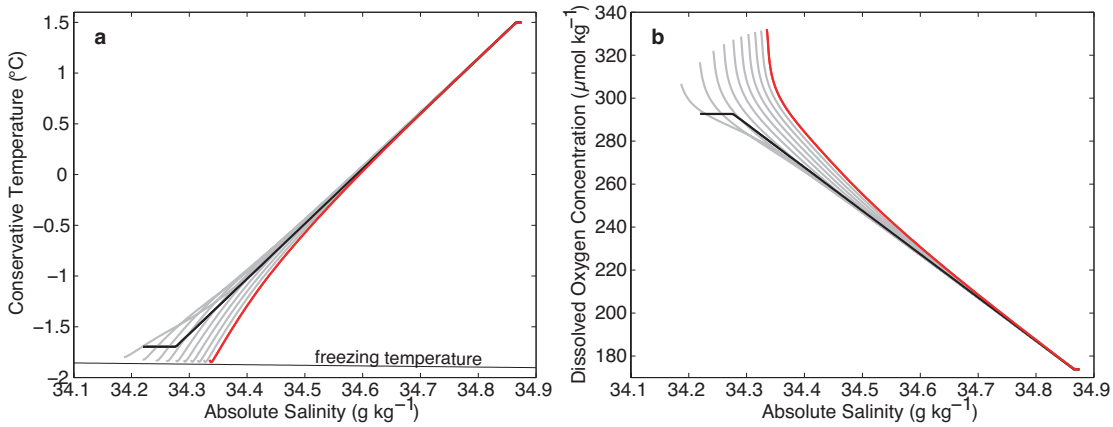

Figure 5.13: Conservative temperature - absolute salinity (a) and dissolved oxygen - absolute salinity (b) plots of a 10 year mPWP run with varying WW. The black line shows the initial profile (from 70 m depth to the base of the water column), with the grey lines showing the profile each year (years 2 - 9). The red line shows the final profile after 10 years. The temperature of the freezing point is also plotted on (a), showing the slight decrease in temperature with the increased salinity associated with sea ice production.

In Chapter 3, the level of curvature was quantified by calculating the area between a linear mixing line and the curve (Section 3.6.1). This method was useful for observing the spatial variation in the size of curvature across the Amundsen Sea, but is not

useful here, as we only have the one mPWP simulation. Instead, whether curvature was produced will be assessed qualitatively by the shape of the curve.

Overall, whilst this simulation of the production of the WW′ endpoint shows curvature in the mixing line, the shape of curvature does not reflect what is observed in the Ocean2ice data. The hydrographic observations from the Ocean2ice cruise appear to show curvature at both ends of the mCDW-WW mixing line, with a maximum point of curvature (Figures 3.19c and 3.20c). However, the profile produced by this simulation retains a linear mixing line at the base of the water column. This suggests that whilst variation in the WW endpoint can produce some curvature, it is unlikely to be the only process occurring at the central shelf edge. The next simulation will therefore include both WW variation and mCDW variation.

5.6.2 Variations in the mCDW endpoint

The second hypothesis for what could be causing the curvature is variation in the mCDW endpoint. This would involve a cycle or switch between the UCDW and LCDW endpoints at the shelf edge, resulting in a changes to a cooler, slightly more saline and higher dissolved oxygen endpoint (if UCDW to LCDW). This is modelled in mPWP by running the model for five years with the UCDW endpoint, before switching the relaxation endpoint to the LCDW characteristics. The initial 5 year run with UCDW is included to ensure that any effects from the initiation of the model have disappeared. The variation in the WW endpoint is included in this simulation, due to the drift and gradual increase in sea ice as mentioned above (Section 5.6.1). In addition, as the production of the WW′ endpoint alone was not enough to explain the curvature seen in the hydrographic observations, the inclusion of that process in this simulation is useful to see if the contribution of both of these processes is important.

The switch between the endpoints can be seen clearly in both of the property-property plots (Figure 5.14). The curvature caused by the variation in the WW′ endpoint can still be seen at the less saline end of the profile, but a midpoint from which

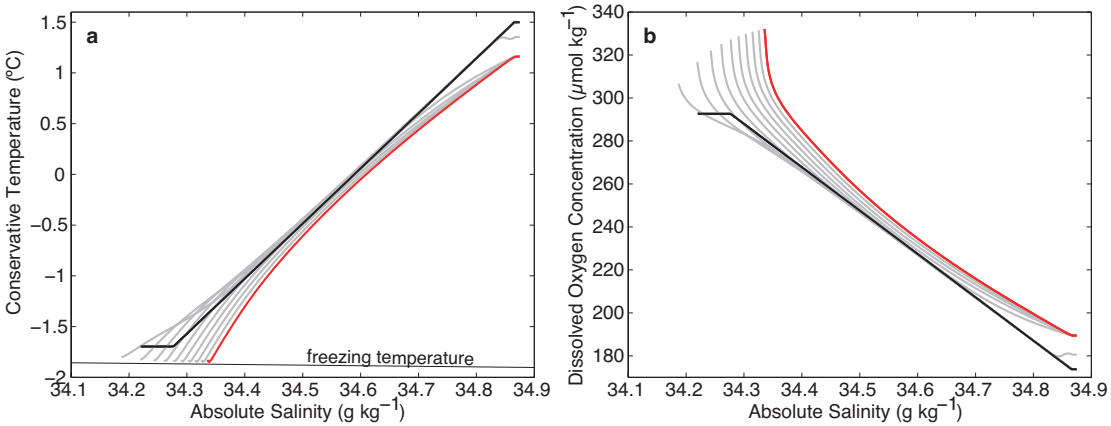

Figure 5.14: Conservative temperature - absolute salinity (a) and dissolved oxygen - absolute salinity (b) plots of a 10 year mPWP run with varying WW and mCDW. The black line shows the initial profile (from 70 m depth to the base of the water column), with the grey lines showing the profile each year (years 2 - 9). The red line shows the final profile after 10 years. The mCDW endpoint is switched from UCDW (black line) to LCDW (end of red line) after 5 years run. The temperature of the freezing point is also plotted on (a), showing the slight decrease in temperature with the increased salinity associated with sea ice production.

both ends of the profile curve away from is now visible (at approximately 34.6 g kg^{-1}). This curvature seems to replicate the shape seen in the hydrographic observations much better, suggesting that there are likely two processes occurring to modify Θ, S_A and $c(O_2)$ at the central shelf edge.

5.6.3 Effects of biological activity

In addition to the curvature observed in Θ-S_A and $c(O_2)$-S_A space at the central shelf edge, a more spatially homogenous curvature was seen in $c(O_2)$-S_A. This was hypothesised to be due to a more regional process, such as biological respiration at depth. To test this, biological processes affecting the dissolved oxygen concentrations were introduced to the mPWP model, using a 'varying WW' run with the UCDW endpoint fixed. This included an estimate of NCP rates below the mixed layer, which there are few observations of in the Amundsen Sea. Due to this, these model simulations can give an indication of the shape of the curve that may be produced, but it is unlikely to reproduce the magnitude that might be seen in the hydrographic observations.

The profile produced (Figure 5.15) can be compared with the $c(O_2)$-S_A diagram

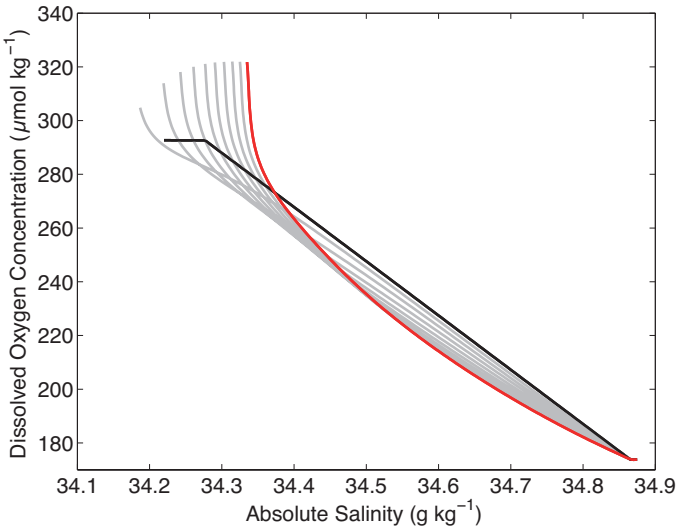

Figure 5.15: Dissolved oxygen - absolute salinity plot of a 10 year mPWP run with varying WW and biological processes parameterised. The black line shows the initial profile (from 70 m depth to the base of the water column), with the grey lines showing the profile each year (years 2 - 9). The red line shows the final profile after 10 years.

from the varying WW run (Figure 5.13b). The most noticeable difference is that the mixing line now has lower dissolved oxygen concentrations than the initial mCDW-WW mixing line, and despite no change in the mCDW endpoint, there is a clear curvature throughout the entire profile. If the excess surface productivity is ignored, the lower portion of the profile (from approximately 34.4 g kg^{-1}) can be seen to replicate the shapes of the profiles seen in Figure 3.20, indicating that biological respiration plays an important role in depleting dissolved oxygen concentrations.

5.7 Conclusion

In Chapter 3, a curvature was identified in the mixing line between mCDW and WW. In order to identify processes that may cause this curvature, a one-dimensional ocean model was adapted for use in the Amundsen Sea. The Price-Weller-Pinkel model (PWP) was used, which is a bulk mixed layer model with mixing parameterised using Richardson numbers as diagnostic tools. This model was modified (becoming the mPWP) to calculate heat and freshwater fluxes on each iteration, and to include sea

ice processes in order to deal with the freezing surface temperatures throughout the winter. Due to the strength of the buoyancy stratification from the cold WW* layer, the mixed layer did not shoal in the summer months. An additional mixing parameterisation, based on Kraus-Turner type mixing (Niiler and Kraus, 1977), was included, allowing seasonal shoaling of the mixed layer. As a one-dimensional model cannot have advection, an analogue was introduced in order to maintain the warm mCDW layer at depth. This involved a relaxation of the water column back to the initial values below 597 m, over a specified timescale.

The meltwater calculations described in Chapter 2 include dissolved oxygen as a conservative tracer, and so it was necessary to add this to the mPWP model. A simple parameterisation of physical atmosphere-ocean processes was used, ignoring exchange of oxygen due to bubble entrainment. The sea ice relationship was also simplified, reducing the gas transfer velocity when sea ice was present and ignoring any addition of oxygen through solute rejection during sea ice formation. This resulted in an almost constant dissolved oxygen concentration throughout the water column over the 10 year model run. Biological processes were also included, with addition or subtraction of dissolved oxygen based on a simulated NCP profile. The NCP rates were reduced greatly from previous reported values, in order to avoid excessive depletion of dissolved oxygen at depth.

The model still has some limitations, primarily induced by the one-dimensional nature of the model and the simple parameterisation of sea ice. The lack of realistic advection and horizontal diffusion will have implications when the model is run for time-scales of this length (10 years), with initial boundary conditions affecting the entire water column. This is evident especially in the dissolved oxygen model data when biological processes are included; the dissolved oxygen becomes excessively depleted at depth. The simple parameterisation of sea ice ignores heat and gas exchange through the sea ice itself. This possibly has a minimal affect on the dissolved oxygen, but the heat transfer through the sea ice may assist in summer melting of the

ice – something which is lacking in this model. The sea ice parameterisation also assumes set concentrations of sea ice; either 0.6 or 0.77 when it is melting or growing. Advection of sea ice in a one-dimensional model is unlikely to ever be realistic, so this may be a limitation associated with the dimensions of the model rather than the parameterisation. Finally, the biological processes that affect the dissolved oxygen concentrations are limited by a lack of observations of respiration below the mixed layer depth, and would also benefit from a seasonally changing NCP profile.

Despite these limitations – mainly focused on advection, sea ice parameterisation and realistic NCP rates – the mPWP model produces useful results, with temperature and salinity seasonal cycles that act reasonably when compared with heat and freshwater fluxes in the region. The temporal changes in dissolved oxygen, whilst not as reliable as the temperature and salinity, are still useful in identifying processes that may affect meltwater calculations.

The mPWP model was used to simulate processes in the Amundsen Sea that may produce the curvature observed in hydrographic datasets from the region. Through testing the effects of variations in WW and mCDW endpoints, and the effects of biological activity, it was found that all three of these processes play important roles in affecting ocean properties. The central shelf edge curvature was likely caused by a combination of increased sea ice formation and variations in the mCDW properties that were able to access the shelf. These changes produced curvature throughout the profile, replicating the shape seen in observations. Biological respiration depleted dissolved oxygen concentrations at depth, and, whilst the NCP rates are a magnitude lower that those observed, replicated the shapes of profiles seen in c(O_2)-S_A space across the eastern Amundsen Sea continental shelf.

In order to produce reliable results of glacial meltwater fractions across the Amundsen Sea, these processes must be accounted for in the observations, or the uncertainty that they cause must be quantified. This will be addressed in Chapter 6, where recommendations will be made for glacial meltwater calculations in the Amundsen Sea.

Chapter 6

Identifying Glacial Meltwater in the Amundsen Sea

6.1 Introduction

A one dimensional ocean model, modified for use in the Amundsen Sea, revealed that variations in sea ice production (identified by the temperature drift) and mCDW properties can reproduce a curvature in the mixing line between mCDW and WW. Dissolved oxygen concentrations were also included as a tracer in the model, with both physical and biological processes affecting the concentrations. This showed that biological respiration below the mixed layer can deplete dissolved oxygen concentrations, also resulting in curvature in the mixing line between mCDW and WW in c(O_2)-S_A space.

Previous studies have shown evidence for the deeper component of the CDW (the LCDW) travelling on to the continental shelf (Assmann *et al.*, 2013; Walker *et al.*, 2013), which is also supported by our observations from the 2014 Ocean2ice cruise (Chapter 3) and model results (Chapter 5). This suggests that the occurrence of LCDW on the continental shelf is not a unique feature only observed in the 2014 data. However, due to a lack of studies of NCP rates below the mixed layer, there

is no information on the temporal variability of biological respiration in the eastern Amundsen Sea.

The potential impacts that glacial meltwater may have on local and global scales are significant: from causing changes in sea ice formation rates to affecting the global heat transport (Richardson *et al.*, 2005; Jacobs and Giulivi, 2010). The multiple observations of the LCDW signature coming up from depth at the edge of the continental shelf suggests that it is important to try to understand how to adjust the glacial meltwater calculations for this signature. In addition, it will be useful to be able to account for the effects that biological respiration has, despite poor representation in the mPWP model and minimal measurements of NCP rates below the mixed layer. This chapter will discuss the changes that can be made to the current glacial meltwater calculation methods, and provide recommendations for the future.

6.2 Adjusting for mCDW variations

The current glacial meltwater calculation results in an apparent meltwater fraction at the central shelf edge due to curvature in the mixing line between mCDW and WW (Figures 3.11 and 3.19). In order to understand this further, it is useful to reappraise the values used in this calculation. Throughout this thesis, the calculation has used the mCDW endpoint for the PIB region (Θ = 1.15 °C; S_A = 34.87 g kg^{-1}; c(O_2) = 187 μmol kg^{-1}), and a WW endpoint from the eastern channel (Θ = -1.76 °C; S_A = 34.27 g kg^{-1}; c(O_2) = 291 μmol kg^{-1}). The endpoints were chosen in the same way as previous studies have selected endpoints, resulting in similar values between studies (e.g. Nakayama *et al.*, 2013, shown in Table 2.1 of this thesis).

To explore how realistic it is to use these values, the mCDW-WW and mCDW-MW mixing lines were plotted on top of the CTD data from in front of PIIS (Figure 6.1). This location is chosen as it is where the glacial meltwater has just emerged from under the ice shelf and so the meltwater signature is likely to be larger than any noise

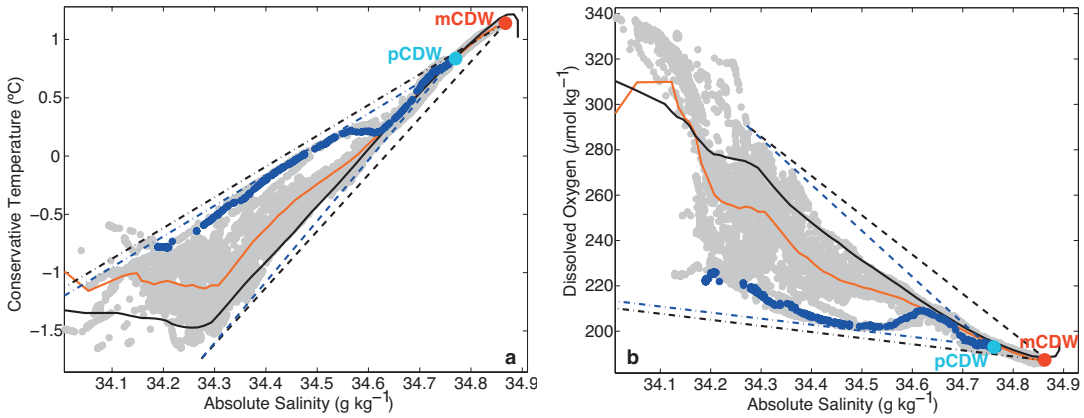

Figure 6.1: Conservative temperature - absolute salinity (a) and dissolved oxygen concentration - absolute salinity (b) diagrams for CTD stations in front of PIIS (see Figure 3.1), showing all data points (grey), the density-average for the continental shelf (black line) and the density-average for PIIS (orange line). The original mCDW-WW mixing line is plotted (black dashed line), as well as the mCDW-MW mixing line (black dot dash line), with the mCDW endpoint shown as a red dot. The new mixing lines formed with the pCDW endpoint are plotted in blue, and the data points from CTD 49 are also shown as blue dots. The pCDW endpoint is marked as a light blue dot.

or other processes (such as biological respiration) that could affect it (Jenkins and Jacobs, 2008). The mCDW-WW mixing line is approximately parallel to the average profile of Θ-S_A properties across the whole Amundsen Sea, but the average profile for PIIS veers away from this mixing line towards lower salinities below approximately 34.55 g kg^{-1}. This is due to the glacial meltwater identified in this location (Chapter 3), with CTD Stations 37 and 49 showing the most concentrated outflow (blue profile; Figure 6.1). However, this profile shows a different gradient to the mCDW-MW mixing line (black line; Figure 6.1), and has a different intercept with the mCDW-WW mixing line (blue line; Figure 6.1). As this CTD profile is taken in the location of the highest concentration of glacial meltwater, the gradient of the line can be taken to represent the true gradient of the mCDW-MW mixing line (Chapter 2; Jenkins, 1999; Jenkins and Jacobs, 2008). The new intercept for the mCDW-MW line is referred to as a pseudo-mCDW endpoint (or pCDW). The pCDW endpoint intercepts the mCDW-WW mixing line at Θ = 0.76 °C, S_A = 34.75 g kg^{-1} and c(O_2) = 194 μmol kg^{-1}.

The depth that these properties are found at is shown by the contours (of Θ, S_A

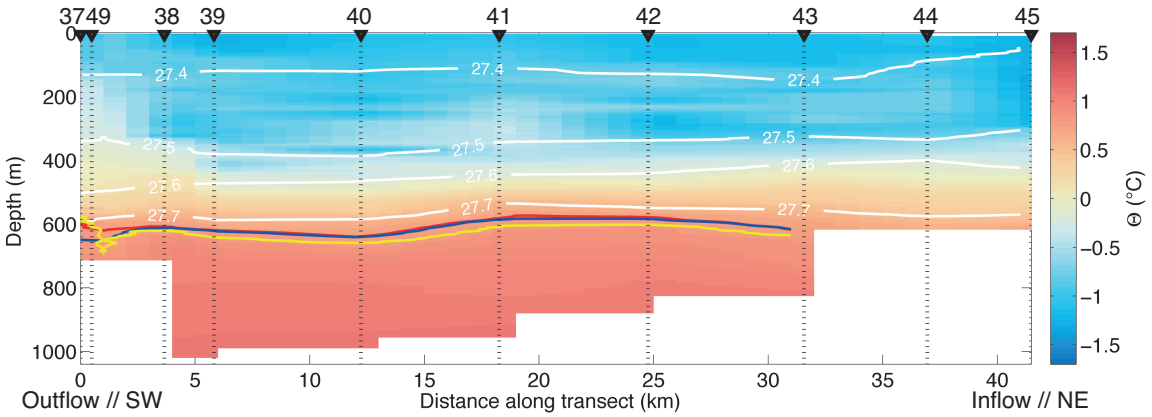

Figure 6.2: Section of Θ across the front of PIIS (Section 6), with isopycnals in white (kg m^{-3}), and contours of Θ = 0.76 ° (red), S_A = 34.75 g kg^{-1} (blue) and c(O_2) = 194 µmol kg^{-1} (yellow).

and c(O_2)) plotted onto the section of Θ across the front of PIIS (Figure 6.2). This shows that these pCDW properties occur at a depth of approximately 600 m across the section. In Chapter 1, the bathymetry under PIIS was discussed and the under ice ridge that is perpendicular to the flow of the glacier was highlighted (Figure 1.2 of this thesis; Jenkins *et al.*, 2010). The gap between this ridge and the bottom of the ice shelf can control how much mCDW reaches past this point and can continue on to the grounding line of the glacier where the melting occurs (Jenkins *et al.*, 2010; Jacobs *et al.*, 2011; Dutrieux *et al.*, 2014). The combination of the ridge and the ice shelf leaves a 200 m gap for water to flow through, reaching between 400 m and 600 m below sea level. This is significant, as the deepest point of the water column that can theoretically reach the grounding line corresponds to the depth at which the water properties attributed to the pCDW endpoint can be found.

Using the new pCDW endpoint, the glacial meltwater fractions were re-calculated across the Amundsen Sea. Of particular interest are the changes in front of PIIS and at the central shelf edge, and both the original glacial meltwater sections and the new sections for these locations are shown for comparison (Figure 6.3). In the new MW section across the front of PIIS, the glacial meltwater signature appears to be a higher concentration at depths with densities greater than σ_θ = 27.72 kg m^{-3}. This is an unfortunate compromise introduced by the pCDW endpoint and the non-negativity con-

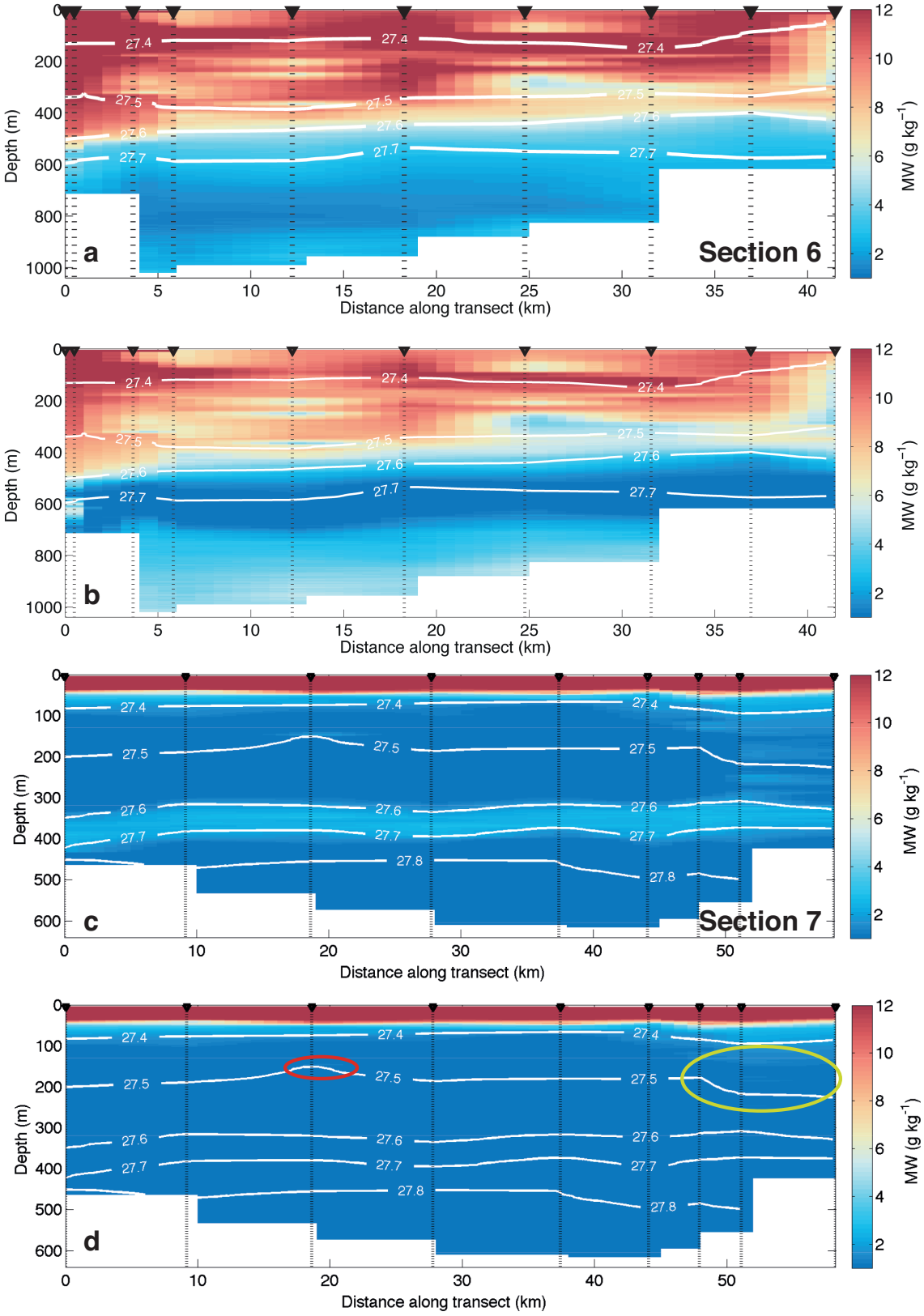

Figure 6.3: Sections of glacial meltwater fractions from Sections 6 and 7 (Figure 3.1). All panels show the isopycnals in white (kg m^{-3}). (a) and (c) show the glacial meltwater fractions using the mCDW endpoint for: PIIS (a) and the central shelf edge (c). (b) and (d) show the glacial meltwater fractions using the pCDW endpoint for the same sections. Also circled are traces of glacial meltwater at the shelf edge (d), in red and yellow.

straint applied during OMPA. The non-negativity constraint means that data points with properties that are warmer, more saline and with lower dissolved oxygen concentrations will appear as apparent positive glacial meltwater fractions (similar to the eastern channel in Chapter 2). This means that whilst using this correction, glacial meltwater fractions at depths with densities greater than σ_θ = 27.72 kg m^{-3} are excluded.

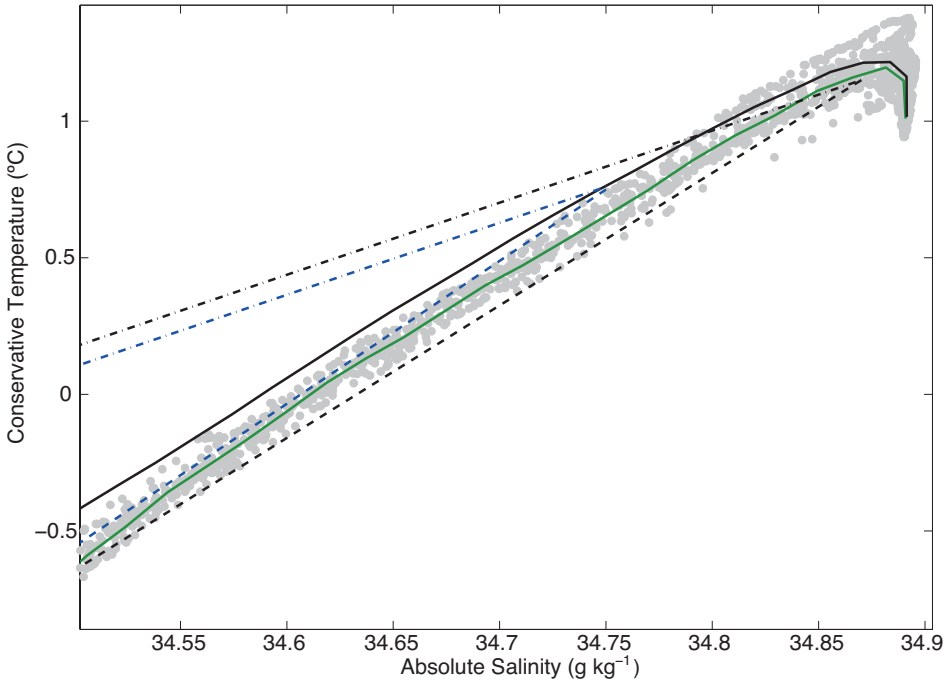

Figure 6.4: Conservative temperature - absolute salinity diagram for CTD stations at the central shelf edge (see Figure 3.1), showing data points (grey), the density-average for the continental shelf (black line) and the density-average for the central shelf edge (green line). The original mCDW-WW mixing line is plotted (black dashed line), as well as the mCDW-MW mixing line (black dot dash line). The new mixing lines formed with the pCDW endpoint are plotted in blue.

The significant result from the new glacial meltwater fractions is that the apparent glacial meltwater plume across the central shelf edge no longer exists. This indicates that by correcting the mCDW endpoint, the curvature that existed in the mCDW-WW mixing line at the central shelf edge may be accounted for. This shift of the mixing line, shown in Figure 6.4, effectively removes the 'curved', more saline, portion of the line that is caused by the mCDW variability.

Despite removing the apparent glacial meltwater plume at approximately 400 m

depth, the use of the pCDW endpoint does not completely remove all traces of glacial meltwater at the shelf edge. Towards the eastern end of the section, there are low concentrations of glacial meltwater, associated with the CTD station at about 50 km distance along the section (circled in yellow; Figure 6.3d). A small, localised amount of glacial meltwater is also apparent at nearly 20 km distance along the section at approximately 150 m depth (circled in red; Figure 6.3d). Both of these occurrences of apparent glacial meltwater are of low concentration (≤ 2 g kg^{-1}) and can be seen to coincide with changes in the $\sigma_\theta = 27.5$ kg m^{-3} contour – but in opposite directions. The eastern portion of apparent glacial meltwater makes that section of the water column less dense, whilst the smaller portion of apparent glacial meltwater appears to make the water column more dense. These horizontal variations in density are typically associated with geostrophic currents, and so the changes in density observed in this section may be a 2D representation of an eddy or lens of meltwater. For both of these signatures, the only way to identify glacial meltwater for certain would be through analysis of noble gas samples or δ^{18}O isotopes.

Overall, by adjusting the mCDW endpoint to the 'pseudo-CDW', or pCDW, endpoint the curvature observed at the shelf break was corrected for. The pCDW endpoint has a strong physical basis to be used: it is likely the deepest water that is able to access the cavity and melt PIG at the grounding line. However, the effects of biological respiration on the curvature across all profiles in the Amundsen Sea have not yet been discussed (Section 6.3).

6.3 Adjusting for biological respiration

All of the profiles from the Amundsen Sea continental shelf displayed curvature in c(O_2)-S_A space (Chapter 3 and Figure 3.20). This was attributed to a different process than that causing the curvature in Θ-S_A space at the central shelf edge due to the differences in the spatial variability. Model simulations of biological activity in

the Amundsen Sea suggested that biological respiration could create similar curvature to that observed (Chapter 5, Section 5.6.3). However, in order to correct for biological respiration, the approximate magnitude of this process needs to be known, which requires CFC or SF_6 measurements in addition to the $c(O_2)$ measurements already collected. As these measurements do not exist for the Amundsen Sea, the only option available is to assess the uncertainty that may be associated with biological respiration.

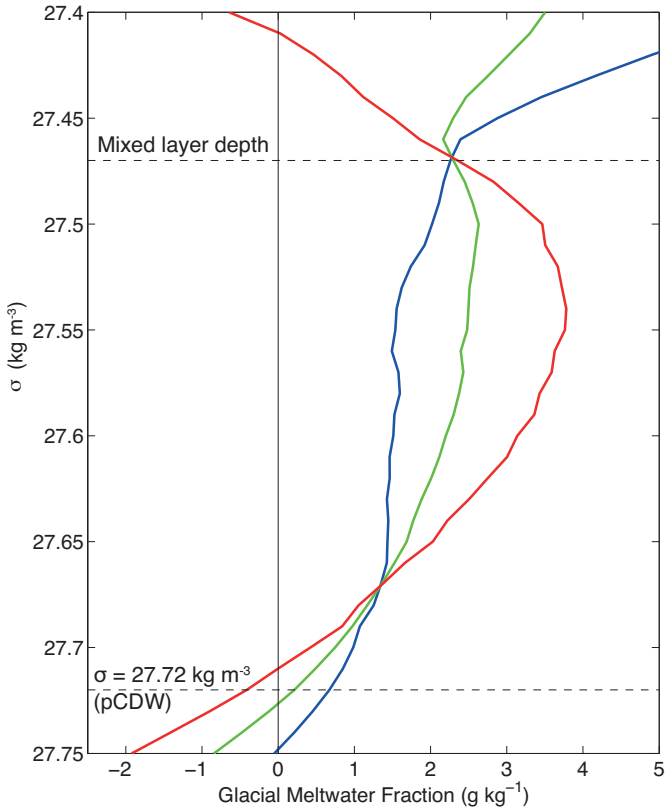

Figure 6.5: Density-average glacial meltwater fractions (g kg^{-1}) from the Pine Island Bay area (see Figure 3.1) calculated using ESM, plotted against σ_θ (kg m^{-3}). The ESM uses pairings of properties: Θ-S_A (blue line), c(O_2)-S_A (green line) and c(O_2)-Θ (red line). These values diverge above the mixed layer depth due to atmospheric processes, and are not expected to be reliable for values more dense than the pCDW endpoint (σ_θ = 27.72 kg m^{-3}).

The exact system method (ESM) can be used to calculate glacial meltwater fractions (Chapter 2), allowing a comparison between fractions calculated using the Θ-S_A pairing to those calculated using c(O_2)-S_A or c(O_2)-Θ (Figure 6.5). This comparison shows that the c(O_2)-Θ pairing produces the highest glacial meltwater fractions be-

low the mixed layer, and in this example is 2.14 g kg^{-1} higher than the Θ-S_A fractions (3.63 g kg^{-1} compared with 1.49 g kg^{-1}). The c(O_2)-S_A pairing produces fractions that are around 1 g kg^{-1} higher than the Θ-S_A pairing. These differences are comparable to the uncertainty associated with the selection of endpoints ($\pm$2 g kg^{-1} ; Chapter 2).

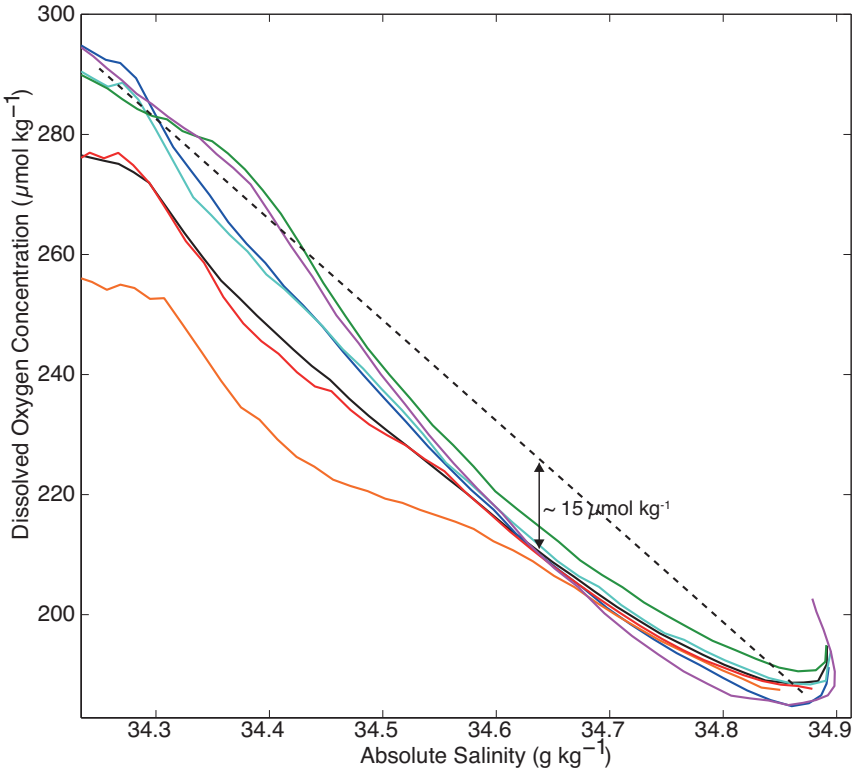

Figure 6.6: Dissolved oxygen concentration - absolute salinity diagram for all of the density-average profiles from across the Amundsen Sea, coloured according to Figure 3.1. The mCDW-WW mixing line is plotted on (black dashed line), and the difference between this mixing line and the profiles is shown with arrowheads.

By using OMPA to calculate the glacial meltwater fractions, the different properties can be weighted based on the uncertainties associated with them (Chapter 2). Despite the lack of information to correct for the biological respiration, this may be one way to account for this process within the calculation method. If the entire decrease in glacial meltwater fraction is assumed to be due to biological respiration, the respiration can be assumed to have decreased the c(O_2) values by approximately 15 μmol kg^{-1} (Figure 6.6). However, the uncertainty associated with dissolved oxygen

concentrations in the current OMPA is 400 μmol kg^{-1} ($\pm$ 200 μmol kg^{-1}; Chapter 2), which is far larger than the uncertainty introduced by biological respiration. This means that the glacial meltwater fractions are already heavily weighted towards Θ and S_A, and so no changes are made to the weightings in OMPA.

6.4 Glacial meltwater pathways in the Amundsen Sea

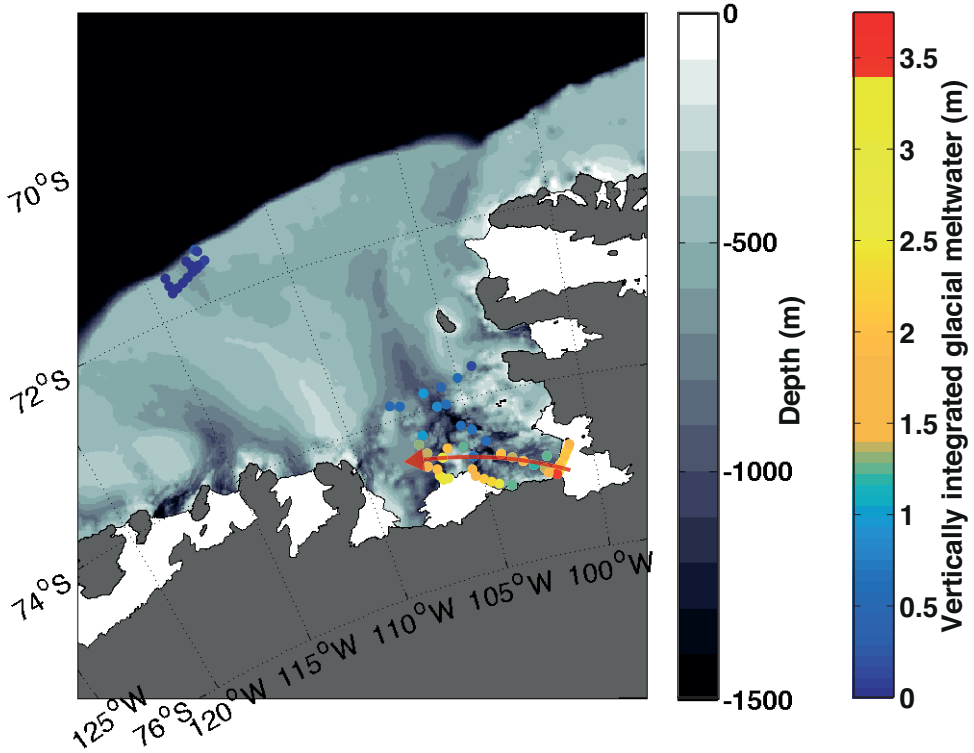

Figure 6.7: Map of the Amundsen Sea showing CTD stations from in front of PIIS, PIB and the central shelf edge (see Figure 3.1). The bathymetry is shown in greyscale, and each CTD station is coloured by the vertically integrated content of glacial meltwater (m) between 150 and 600 m. A red arrow indicates the possible pathway of glacial meltwater after leaving PIIS.

Using these modifications to the meltwater calculation method, the CTD stations can be analysed to identify the spatial variability of the glacial meltwater in the Amundsen Sea (Figure 6.7). As the apparent glacial meltwater fractions are affected by atmospheric effects at the surface (Figure 3.15), and by the use of pCDW at depth, only values between 150 and 600 m are used. This is a reasonable depth

range to use, as the majority of glacial meltwater is expected to lie between these depths (Naveira-Garabato *et al.*, *submitted*). The glacial meltwater values between 150 and 600 m are integrated to give an estimate of the vertical meltwater content. Due to the UCDW endpoint for the eastern channel, the CTD stations in this location are ignored.

The glacial meltwater is most highly concentrated at the western ends of PIIS and Thwaites Ice Shelf (up to 3.72 m of glacial meltwater in 450 m of the water column), where the strongest outflow was observed. The values at the central shelf edge are distinctly lower, with a maximum of 17 cm of vertically integrated glacial meltwater. Within Pine Island Bay, the higher values of vertically integrated glacial meltwater can be found towards the coast and western side of PIB. However, to trace the glacial meltwater further from the ice shelf more CTD stations are needed to the west of this area.

Nakayama *et al.* (2014) modelled the spread of glacial meltwater from the Amundsen Sea (reproduced in Figure 1.4 of this thesis), finding vertical integrations of glacial meltwater approximately 50 % lower at the central shelf edge than the front of PIIS (2 m at the continental shelf edge and 4 m at PIIS). The vertically integrated glacial meltwater values calculated for the 2014 data show a much bigger difference between the two locations (the central shelf edge is around 5 % of the value at the front of PIIS). However, the values in front of PIIS are almost exactly the same between the model and observations. The differences at the continental shelf edge could be due to many reasons, including different meteorological conditions (i.e. we sampled a low meltwater year or the off-shelf transport was different due to variability in the winds), the tuning used in the computer model was not quite right, or the contribution of glacial meltwater from other sources. However, the spatial distribution of PIG meltwater (if not the exact values) is similar between the model and our observations. This is encouraging for both the calculation method used in this thesis, and for future development of computer models of this region.

6.5 Conclusion

With the use of a one dimensional ocean model, the curvature identified in Chapter 3 was shown to be due to a combination of physical and biological processes (Chapter 5). In order to improve reliability of the glacial meltwater fractions calculated, these processes must be accounted for – whether through adjusting the calculation method or assessing uncertainties introduced.

Initially, the corrections required for the variations in mCDW endpoint were considered. The way that the mCDW endpoint was chosen was inspected, and consequently changed to a 'pseudo-mCDW' endpoint, or pCDW. This endpoint related to Θ-S_A values that were observed at 600 m depth, which is significant as it is the approximate height of the ridge that blocks deeper water from accessing the cavity and grounding line of PIG. By using the pCDW endpoint, water that is denser than the endpoint (σ_θ = 27.72 kg m^{-3}) is ignored, which essentially removes the curved end of the mCDW-WW mixing line that is observed at the central shelf edge. However, this also means that any information at the bottom of the water column is lost, and Nakayama *et al.* (2013) report observations of glacial meltwater at 800 m depth in front of PIIS using noble gas data.

Due to difficulties modelling the magnitude of biological respiration, it was not possible to correct for the effects of this process, and so the uncertainties associated with the respiration were estimated instead. Using the ESM glacial meltwater calculation, the decrease in dissolved oxygen concentrations due to biological respiration (approximately -15 μmol kg^{-1}) was found to produce fractions up to 2 g kg^{-1} higher than fractions calculated without dissolved oxygen concentrations. As the OMPA calculation can take uncertainties associated with different properties into account, no correction was made for the biological respiration as the existing dissolved oxygen concentration uncertainty outweighed the uncertainty introduced by biological respiration.

The alterations made to the glacial meltwater calculation successfully removed

an apparent glacial meltwater signature at the continental shelf edge, and allowed true glacial meltwater fractions to be observed elsewhere in the water column (Figure 6.3d). These changes emphasised the importance of taking into consideration the processes occurring underneath the ice shelf, and that the warmest waters on the continental shelf are not necessarily melting PIG at the grounding line. To improve the reliability of the glacial meltwater calculation further, the mPWP model must be developed to improve parameterisation of biological processes. Without this information, the glacial meltwater fractions are subject to significant uncertainty below the mixed layer, and can only be used qualitatively.

By plotting the spatial distribution of the vertically integrated glacial meltwater, an approximate estimate of the possible glacial meltwater pathways can be made. The concentrations at the central shelf edge are much lower than those in front of PIIS, whilst the CTD stations to the west and closer to the coastline have higher concentrations of glacial meltwater, and show the pathway of PIG meltwater (Figure 6.7). This agrees with model simulations of the region (Nakayama *et al.*, 2014) and provides encouragement for this qualitative use of the glacial meltwater calculation methods. In order to develop this further, CTD stations further to the west and historical datasets should be used to expand the spatial and temporal analysis of the glacial meltwater.

Chapter 7

Conclusions

7.1 Identifying Glacial Meltwater in the Amundsen Sea

In the Amundsen Sea, it is important to identify glacial meltwater as it travels away from the ice shelf in order to attribute possible effects of the addition of this water mass. Model simulations have shown that the addition of glacial meltwater can result in changes to the local sea ice formation, regional salinity values, and ultimately the global meridional overturning circulation (Richardson *et al.*, 2005). Observations from the Ross Sea have shown a freshening of the shelf waters over the last 30 years, and some signs of changes to AABW formation rates (Jacobs and Giulivi, 2010; Kouketsu *et al.*, 2009; Purkey and Johnson, 2012). For these reasons, this thesis aimed to examine current glacial meltwater identification methods, and assess the reliability of these methods with increasing distance from the front of PIIS.

7.1.1 Meltwater calculations

Two methods of calculating glacial meltwater fractions were described: the exact system method (ESM) and optimum multiparameter analysis (OMPA). Both of these methods are useful in a system where there are three water masses to be identified, and three tracers that can be used (plus the mass conservation equation). These melt-

water calculation methods are reliant on linear mixing lines between the water masses being identified. OMPA was favoured of these two methods, as it calculated the glacial meltwater fractions using all of the tracers available at one time. The ESM calculated the glacial meltwater fractions using pairings of the tracers and averaged the resulting three fractions (if using three tracers) to produce the overall glacial meltwater fraction. OMPA also allowed weighting of the different tracers, based on the analytical and environmental uncertainties associated with each tracer.

The uncertainties associated with the glacial meltwater calculation method were estimated using Monte Carlo simulations. These simulations varied each of the endpoints for mCDW, WW and MW to estimate how much uncertainty these variations in the endpoints could cause, with a standard deviation of ± 2 g kg^{-1} in the calculated glacial meltwater fraction if all endpoints were perturbed.

Whilst using OMPA has the benefits of using all three properties at once, and the ability of weighting different parameters, it also has limitations. The limitations of OMPA include the non-negativity constraint applied to the fractions. Although this is useful in ensuring physically possible fractions are calculated, it resulted in 'false' meltwater signatures when the CTD data lay outside of the mCDW-WW-MW triangle (e.g. the eastern channel in Chapter 3; below $\sigma_\theta = 27.72$ kg m^{-3} in Chapter 6). One way to minimise the effects of this non-negativity constraint is to choose appropriate endpoints for the dataset being used.

7.1.2 False meltwater signatures

Between January and March 2014, hydrographic observations (including conservative temperature, absolute salinity and dissolved oxygen concentrations) were collected from the Amundsen Sea. The endpoints for mCDW and WW were identified using this dataset and glacial meltwater fractions calculated using OMPA. This revealed the spatial distribution of the glacial meltwater, showing an apparent glacial meltwater signature forming a horizontal plume at about 400 m depth across the con-

tinental shelf edge of the central channel. Analysis of property-property plots showed that the mixing line between mCDW and WW was curved in this location, as may be expected when mixing between three water masses occurs (Tomczak, 1981). However, in Θ-S_A space, this feature was only observed in this location, suggesting the possibility of a unique physical process occurring here and not elsewhere on the shelf.

In $c(O_2)$-S_A space the curvature was nearly homogeneous across the shelf, suggesting a different process to that which was causing the curvature in Θ-S_A space. Hypotheses including variations in the endpoints or biological activity affecting $c(O_2)$ were described. Biological activity was shown to have a significant effect on glacial meltwater signatures. At the surface, biological productivity was shown to decrease apparent glacial meltwater fractions in the Amundsen Sea. The presence of glacial meltwater was also shown to enhance this biological productivity in the Weddell Sea. The scale that this occurs at is too small to capture through satellite observations, so it is hard to know how frequent or widespread this effect may be. At depth, biological respiration could decrease $c(O_2)$ values, resulting in an apparent increase in glacial meltwater fractions.

The development of a one dimensional model that included sea ice processes and dissolved oxygen as a tracer allowed simulation of both the physical and biological processes in a controlled environment. These simulations, over a 10 year period, revealed that the combination of varying WW properties and a switch between UCDW and LCDW endpoints for mCDW can create the curvature observed in Θ-S_A space. It is possible that these processes are linked in reality in this region: the deeper mixed layer associated with increasing sea ice formation would be more liable to block transport of UCDW on shelf, so a transition to a cold phase might result in the curvature observed. The variations in WW and mCDW endpoints created a small curvature in $c(O_2)$-S_A space, but did not replicate the size or shape of the curvature observed in the hydrographic dataset. When biological processes were applied, the stronger curvature seen in $c(O_2)$-S_A space was created. The biological model used in the mPWP

requires further development of both the parameterisations of biological processes and the seasonal variability of NCP rates. However, these model results can be used as a suggestion of how biological respiration at depth may affect the shape of the mixing line.

The ability of these processes to replicate the curvature observed in the hydrographic observations strongly indicates that they must be considered and accounted for within glacial meltwater calculations. By accounting for these processes any true meltwater signature can be observed, and initial indications of meltwater pathways can be made.

7.1.3 Recommendations for glacial meltwater calculations

The aim of this thesis was to improve the reliability of glacial meltwater calculations. The uncertainties associated with the calculation methods were assessed, and processes that may influence the calculations were identified. In order to improve the calculations further, it is important to try to account for these processes.

The most significant finding that emerged from inspecting the mCDW endpoint was that the 'typical' mCDW endpoint should not necessarily be used. Typically, the mCDW endpoint is usually the warmest waters found within PIB (approximately 1.16 °C), but this does not necessarily equate with the waters that the glacial meltwater mixes with due to the ridge that stretches across the cavity underneath PIIS. Instead, properties from approximately 600 m depth should be used, creating a 'pseudo'-mCDW endpoint (pCDW). In 2014, this displayed a much cooler endpoint: 0.76 °C. As well as creating a more realistic mixing line between pCDW and MW, this shift in endpoint removed the more saline portion of the mCDW-WW mixing line. This is an important change when considering the curvature at the central shelf edge, as it removed the portion of the mixing line that showed curvature due to the UCDW-LCDW variations.

As the magnitude of the effects of biological respiration are not represented well

in mPWP, no correction can be made for this process. Instead, uncertainties are calculated to try to understand how reliable the calculations may be at a distance from the ice shelf. If biological respiration was assumed to cause all of the curvature seen in the c(O_2)-S_A profiles, it represents a decrease of up to 15 μmol kg^{-1}. As the weightings used in OMPA are already calculated from an uncertainty of ±200 μmol kg^{-1}, this uncertainty is essentially already accounted for.

The corrections made to – and uncertainties accounted for in – the glacial meltwater calculations provide meltwater fractions for the Ocean2ice hydrographic dataset. The fractions show glacial meltwater pathways from PIG, and the uncertainties associated with them mean that values below 8 g kg^{-1} should be used as qualitative indicators of glacial meltwater. The developments made in this thesis have contributed to knowledge of processes affecting apparent glacial meltwater fractions in this region.

7.1.4 Summary

Overall, this thesis has identified processes, or features, not discussed previously in the context of glacial meltwater calculations. The two main processes identified were the variability in the mCDW properties that were transported onto the shelf and the blocking effect of the ridge underneath PIIS. The variability in mCDW endpoint resulted in a curvature in the mCDW-WW mixing line (due to switches between UCDW and LCDW properties at the shelf edge). Adjustments made for the presence of the ridge resulted in the use of a different mCDW (or pCDW) endpoint to what has been assumed previously (e.g. Nakayama *et al.*, 2013). With the use of corrections for these processes, the glacial meltwater was seen to be concentrated to the western end of the ice shelf, and close to the coast. These findings are shown schematically in Figure 7.1.

Although these findings are useful, they do not take into account biological effects. Further work is required in order to understand how biological respiration may affect dissolved oxygen concentrations at depth (discussed further in Section 7.2). In

addition, the glacial meltwater from the WAIS is thought to travel westwards around the coast to the Ross Sea. In order to verify this hypothesis, these modifications to the glacial meltwater calculations must be extrapolated to regions further west (Section 7.3).

7.2 Future Work

A simple ocean model was developed as part of this thesis in order to identify how individual processes may affect the glacial meltwater calculations, and for this purpose the mPWP has excelled. However, improvements can be made and have been outlined below:

(1) *Parameterisation of sea ice processes*. Sea ice currently acts as a cap to the system, decreasing fluxes by a fraction that represents the sea ice concentration. There are two specific areas that need further work: changes in sea ice concentration could be linked to satellite observations of the region, and air-sea ice-ocean fluxes can be better parameterised, using studies such as Semtner (1976) and Loose *et al.* (2009b). The current exclusion of these may affect the development of the mixed layer.

(2) *Physical processes affecting dissolved oxygen concentrations*. These processes will likely be affected by the changes made to sea ice parameterisations, but the mPWP is also missing any effects caused by bubble entrainment. Bubble entrainment of dissolved oxygen has been parameterised in other studies (e.g. Keeling, 1993; McNeil and D'Asaro, 2007), and so could be added to the model. This will likely modify mixed layer dissolved oxygen concentrations, as opposed to affecting the entire water column, which is why it had been left out of the mPWP model used in this thesis.

(3) *Biological processes affecting dissolved oxygen concentrations*. This has been

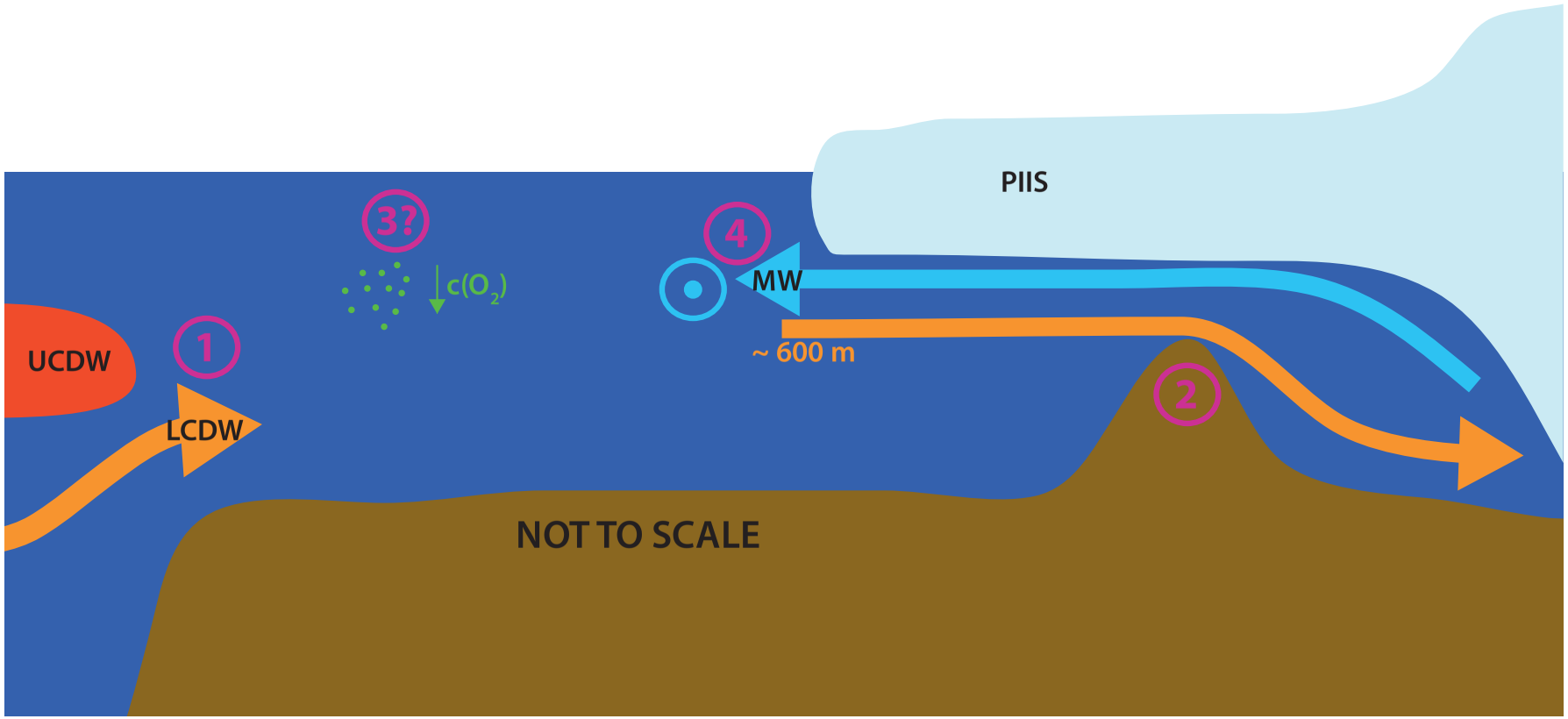

Figure 7.1: Schematic showing the main conclusions from this thesis. Horizontal and vertical lengths are not to scale. (1) Influence of LCDW at the continental shelf edge is important to take into account. (2) The height of the ridge under the ice shelf blocks the deepest waters from accessing the grounding line (approx 600 m depth). (3) Biological respiration decreases dissolved oxygen concentrations ($c(O_2)$), potentially creating false meltwater signatures. (4) Glacial meltwater emerges from under the ice shelf and is transported to the west (bullseye shows flow out of page).

flagged in Chapters 5 and 6 as well: the biological model used is not representative of reality. The magnitudes of NCP rates are too low, and seasonal changes are unlikely to be reproduced. In order to improve this element of the model, the parameterisations of biological processes need further development – especially focusing on NCP rates below the mixed layer. Time-series of respiration rates below the mixed layer (using $c(O_2)$ and CFCs or SF_6) would be beneficial as this would provide an indication of the seasonality of respiration in this region.

Throughout this thesis, the mPWP model was run with a repeated annual climatology, and used to simulate the effects of different processes. With the changes suggested above, it could instead be used to try to replicate patterns or features in observations collected in different years by using meteorological reanalysis data for those specific years. This would enable attribution of features seen in the observational data to specific processes: for example a warmer year with less sea ice formation may reveal a different curvature than what has been observed in model results so far.

This work has also highlighted the importance of understanding cross-shelf processes. At the shelf edge of the central channel, cross-shelf processes affect the properties of mCDW that are found on shelf, resulting in curvature of the mCDW-WW mixing line. Hydrographic moorings (including temperature and salinity sensors) have been deployed at the shelf edge of both the central and eastern channels, and the data from these moorings would be useful to analyse in order to identify processes driving the warm water on shelf.

By making alterations to the glacial meltwater calculations, the 'plume' observed at the shelf edge of the central channel was removed. Some signatures of glacial meltwater at the shelf edge remained, and during the Ocean2ice cruise noble gas and oxygen isotopes in water samples were collected. These samples – especially the noble gas samples – should indicate whether glacial meltwater is present, as it is the only cause of changes to some of these properties (such as high neon concentrations;

Loose *et al.*, 2014).

With this future work, the mPWP model and glacial meltwater calculation methods should be robust enough to extrapolate to other temporal and spatial scales.

7.3 Perspectives

The research done in this thesis has focussed on the eastern portion of the Amundsen Sea, and on glacial meltwater produced by Pine Island Glacier. There are many other glaciers terminating in the Amundsen Sea, including Thwaites Glacier – recently reported to be in irreversible retreat (Joughin *et al.*, 2014) – and the Getz Ice Shelf, a significant contributor to rates of volume loss in the WAIS (Paolo *et al.*, 2015). However, the further west the region of interest, the more "external" glacial meltwater there is that must be accounted for. "External" meltwater refers to glacial meltwater that has been produced further to the east: measurements in front of Thwaites Ice Shelf (TIS) will have to take into account the inflow of glacial meltwater from PIIS, and Dotson Ice Shelf will have to take into account glacial meltwater from PIIS and TIS. This will potentially create a mixing space with more than three endpoints, and the resulting mixing and transformation processes between these new endpoints must be considered.

There is also temporal variability to be considered. Our measurements and analysis have focussed on data collected in 2014, but studies have identified the interannual variability that exists in this region (Jacobs *et al.*, 2011; Dutrieux *et al.*, 2014; Webber *et al.*, submitted). This variability can affect the thickness of the mCDW layer, and therefore affects what properties exist at 600 m depth and can flow above the ridge. In some years with thicker mCDW layers, the values at 600 m depth may represent the warmest properties found on shelf, and so the pCDW method to remove curvature at the shelf edge will not be applicable.

This work has focussed on a warm-based continental shelf, where mCDW proper-

ties flood the continental shelf. The pattern of two main water masses, plus the glacial meltwater, makes identification of the glacial meltwater relatively straight-forward. Other warm-based shelves have been identified around Antarctica, especially along the West Antarctic margins. In East Antarctica, recent studies have identified warm-based continental shelves that show similar processes of ocean basal melting of the ice shelves in that region (e.g. Totten Glacier; Greenbaum *et al.*, 2015). The ability to extrapolate the methods and findings made within this thesis to these locations around Antarctica would add significant knowledge of glacial meltwater pathways, which may help with future assessment of the effects of glacial meltwater and potentially improve global ocean models.

Appendix A

Proof of equivalence of ESM to CTM

Composite Tracer Method (CTM)

This is the method documented in Jenkins (1999), using the gradient of the mixing line between Circumpolar Deep Water (CDW) and Winter Water (WW) as a composite tracer;

$$\psi = (\chi_{1,obs} - \chi_{1,CDW}) - (\chi_{2,obs} - \chi_{2,CDW}) \left(\frac{\chi_{1,CDW} - \chi_{1,WW}}{\chi_{2,CDW} - \chi_{2,WW}} \right). \tag{A.1}$$

This value (ψ) will equal zero anywhere in the ambient water column, but will become non-zero as soon as another process – such as a new water mass mixing with the ambient water – occurs. It is assumed that the only process that can do this is meltwater addition (MW), and so the maximum value that can be achieved by this process is;

$$\psi = (\chi_{1,MW} - \chi_{1,CDW}) - (\chi_{2,MW} - \chi_{2,CDW}) \left(\frac{\chi_{1,CDW} - \chi_{1,WW}}{\chi_{2,CDW} - \chi_{2,WW}} \right). \tag{A.2}$$

The water column can be assumed to be made up of three parts ($\psi, \psi_{\mathrm{w}}, \psi_{\mathrm{ice}}$),

where ψ_w is the value in the ambient water column and therefore zero. This leads to;

$$Q\psi = Q_w\psi_w + Q_{ice}\psi_{ice}, \tag{A.3}$$

$$\psi_w = 0, \tag{A.4}$$

$$F_{MW} = \frac{Q_{ice}}{Q} = \frac{\psi}{\psi_{ice}}. \tag{A.5}$$

We can expand the brackets in equations A.1 and A.2 and place them in equation A.5.

$$F_{mw} = \frac{(\chi_{1,obs} - \chi_{1,CDW}) + \frac{\chi_{2,obs}\chi_{1,WW} - \chi_{2,obs}\chi_{1,CDW} + \chi_{2,CDW}\chi_{1,CDW} - \chi_{2,CDW}\chi_{1,WW}}{\chi_{2,CDW} - \chi_{2,WW}}}{(\chi_{1,MW} - \chi_{1,CDW}) + \frac{\chi_{2,MW}\chi_{1,WW} - \chi_{2,MW}\chi_{1,CDW} + \chi_{2,CDW}\chi_{1,CDW} - \chi_{2,CDW}\chi_{1,WW}}{\chi_{2,CDW} - \chi_{2,WW}}}. \tag{A.6}$$

Multiply by $\frac{\chi_{2,CDW} - \chi_{2,WW}}{\chi_{2,CDW} - \chi_{2,WW}}$;

$$F_{mw} = \frac{\chi_{1,obs}\chi_{2,CDW} - \chi_{1,obs}\chi_{2,WW} - \cancel{\chi_{1,CDW}\chi_{2,CDW}} + \cancel{\chi_{1,CDW}\chi_{2,CDW}}}{\chi_{1,MW}\chi_{2,CDW} - \chi_{1,MW}\chi_{2,WW} - \chi_{2,CDW}\chi_{1,WW} + \chi_{1,CDW}\chi_{2,WW}} \ldots$$
$$\ldots \frac{-\chi_{2,obs}\chi_{1,CDW} + \chi_{2,obs}\chi_{1,WW} + \chi_{1,CDW}\chi_{2,WW} - \chi_{2,CDW}\chi_{1,WW}}{-\chi_{2,MW}\chi_{1,CDW} + \chi_{2,MW}\chi_{1,WW} + \cancel{\chi_{1,CDW}\chi_{2,CDW}} - \cancel{\chi_{1,CDW}\chi_{2,CDW}}}. \tag{A.7}$$

Let

$$\chi_{1,CDW}\chi_{2,WW} - \chi_{2,CDW}\chi_{1,WW} = c, \tag{A.8}$$

then F_{MW} becomes:

$$\boxed{F_{mw} = \frac{\chi_{1,obs}(\chi_{2,CDW} - \chi_{2,WW}) + \chi_{2,obs}(\chi_{1,WW} - \chi_{1,CDW}) + c}{\chi_{1,MW}(\chi_{2,CDW} - \chi_{2,WW}) + \chi_{2,MW}(\chi_{1,WW} - \chi_{1,CDW}) + c}.} \tag{A.9}$$

Exact System Method (ESM)

The matrix representation of the meltwater fraction calculation is;

$$\begin{pmatrix} \chi_{1,\mathrm{mCDW}} & \chi_{1,\mathrm{WW}} & \chi_{1,\mathrm{MW}} \\ \chi_{2,\mathrm{mCDW}} & \chi_{2,\mathrm{WW}} & \chi_{2,\mathrm{MW}} \\ 1 & 1 & 1 \end{pmatrix} \begin{pmatrix} \mathrm{F_{mCDW}} \\ \mathrm{F_{WW}} \\ \mathrm{F_{MW}} \end{pmatrix} = \begin{pmatrix} \chi_{1,\mathrm{obs}} \\ \chi_{2,\mathrm{obs}} \\ 1 \end{pmatrix}, \tag{A.10}$$

which can also be written as;

$$\mathbf{Ax} = \mathbf{B}. \tag{A.11}$$

The inverse of matrix **A** is taken and multipled by **B** in order to calculate $\mathrm{F_{MW}}$;

$$\mathbf{x} = \mathbf{A}^{-1}\mathbf{B}, \tag{A.12}$$

where,

$$\mathbf{A}^{-1} = \frac{1}{\det\mathbf{A}}\mathrm{Adj}(\mathbf{A}). \tag{A.13}$$

$$\begin{aligned} \det\mathbf{A} &= \chi_{1,CDW}(\chi_{2,WW} - \chi_{2,MW}) - \chi_{1,WW}(\chi_{2,CDW} - \chi_{2,MW}) + \chi_{1,MW}(\chi_{2,CDW} - \chi_{2,WW}), \\ &= \chi_{1,MW}(\chi_{2,CDW} - \chi_{2,WW}) + \chi_{2,MW}(\chi_{1,WW} - \chi_{1,CDW}) + b. \end{aligned} \tag{A.14}$$

The adjugate is the cofactor matrix of the transpose of **A** (or the transpose of the cofactor matrix of **A**).

$$\mathbf{A}^{\mathrm{T}} = \begin{pmatrix} \chi_{1,CDW} & \chi_{2,CDW} & 1 \\ \chi_{1,WW} & \chi_{2,WW} & 1 \\ \chi_{1,MW} & \chi_{2,MW} & 1 \end{pmatrix}, \tag{A.15}$$

$$\mathrm{Adj}(\mathbf{A}) = \begin{pmatrix} +\begin{vmatrix} \chi_{2,WW} & 1 \\ \chi_{2,MW} & 1 \end{vmatrix} & -\begin{vmatrix} \chi_{1,WW} & 1 \\ \chi_{1,MW} & 1 \end{vmatrix} & +\begin{vmatrix} \chi_{1,WW} & \chi_{2,WW} \\ \chi_{1,MW} & \chi_{2,MW} \end{vmatrix} \\ -\begin{vmatrix} \chi_{2,CDW} & 1 \\ \chi_{2,MW} & 1 \end{vmatrix} & +\begin{vmatrix} \chi_{1,CDW} & 1 \\ \chi_{1,MW} & 1 \end{vmatrix} & -\begin{vmatrix} \chi_{1,CDW} & \chi_{2,CDW} \\ \chi_{1,MW} & \chi_{2,MW} \end{vmatrix} \\ +\begin{vmatrix} \chi_{2,CDW} & 1 \\ \chi_{2,WW} & 1 \end{vmatrix} & -\begin{vmatrix} \chi_{1,CDW} & 1 \\ \chi_{1,WW} & 1 \end{vmatrix} & +\begin{vmatrix} \chi_{1,CDW} & \chi_{2,CDW} \\ \chi_{1,WW} & \chi_{2,WW} \end{vmatrix} \end{pmatrix}, \tag{A.16}$$

$$\mathrm{Adj}(\mathbf{A}) = \begin{pmatrix} \chi_{2,WW} - \chi_{2,MW} & \chi_{1,MW} - \chi_{1,WW} & \chi_{1,WW}\chi_{2,MW} - \chi_{2,WW}\chi_{1,MW} \\ \chi_{2,MW} - \chi_{2,CDW} & \chi_{1,CDW} - \chi_{1,MW} & \chi_{2,CDW}\chi_{1,MW} - \chi_{1,CDW}\chi_{2,MW} \\ \chi_{2,CDW} - \chi_{2,MW} & \chi_{1,WW} - \chi_{1,CDW} & \chi_{1,CDW}\chi_{2,WW} - \chi_{2,CDW}\chi_{1,WW} \end{pmatrix}. \tag{A.17}$$

Since we are only interested in the result for $\mathrm{F_{MW}}$, rather than *formulating* equation 2.3, we solve for just $\mathrm{F_{MW}}$;

$$\mathrm{F_{MW}} = a_{31}b_1 + a_{32}b_2 + a_{33}b_3. \tag{A.18}$$

Calculated elementwise;

$$a_{31} = \frac{\chi_{2,CDW} - \chi_{2,WW}}{\chi_{1,MW}(\chi_{2,CDW} - \chi_{2,WW}) + \chi_{2,MW}(\chi_{1,WW} - \chi_{1,CDW}) + c} \qquad b_1 = \chi_{1,obs}$$

$$a_{32} = \frac{\chi_{1,WW} - \chi_{1,CDW}}{\chi_{1,MW}(\chi_{2,CDW} - \chi_{2,WW}) + \chi_{2,MW}(\chi_{1,WW} - \chi_{1,CDW}) + c} \qquad b_2 = \chi_{2,obs} \tag{A.19}$$

$$a_{33} = \frac{\chi_{1,CDW}\chi_{2,WW} - \chi_{2,CDW}\chi_{1,WW}}{\chi_{1,MW}(\chi_{2,CDW} - \chi_{2,WW}) + \chi_{2,MW}(\chi_{1,WW} - \chi_{1,CDW}) + c} \qquad b_3 = 1$$

$$\boxed{\mathrm{F_{mw}} = \frac{\chi_{1,obs}(\chi_{2,CDW} - \chi_{2,WW}) + \chi_{2,obs}(\chi_{1,WW} - \chi_{1,CDW}) + c}{\chi_{1,MW}(\chi_{2,CDW} - \chi_{2,WW}) + \chi_{2,MW}(\chi_{1,WW} - \chi_{1,CDW}) + c}.} \tag{A.20}$$

Abbreviations

14C-NPP	Net Primary Productivity calculated using 14C isotopes
AABW	Antarctic Bottom Water
AASW	Antarctic Surface Water
AIS	Abbott Ice Shelf
ASC	Antarctic Slope Current
AUV	Autonomous Underwater Vehicle
CDOM	Coloured Dissolved Organic Matter
CDW	Circumpolar Deep Water
CFL	Courant-Friedrichs-Lewy condition
CFS	Climate Forecast System
COP21	21st Conference Of the Parties
CTD	Conductivity-Temperature-Depth
CTM	Composite Tracer Method
ESM	Exact System Method
KPP	K-Profile Parameterisation scheme
LCDW	Lower Circumpolar Deep Water
mCDW	modified Circumpolar Deep Water
MLD	Mixed Layer Depth
mPWP	modified Price-Weller-Pinkel model
MW	Glacial MeltWater
NCEP	National Centers for Environmental Prediction

NCP	Net Community Production
OMPA	Optimum MultiParameter Analysis
PAR	Photosynthetically Active Radiation
PIB	Pine Island Bay
PIG	Pine Island Glacier
PIIS	Pine Island Ice Shelf
PWP	Price-Weller-Pinkel model
SAR	Synthetic Aperture Radar
TEOS-10	The Equation Of State, 2010
TIS	Thwaites Ice Shelf
TKE	Turbulent Kinetic Energy
UCDW	Upper Circumpolar Deep Water
WAIS	West Antarctic Ice Sheet
WW	Winter Water
WW’	Winter Water endpoint after increased sea ice formation
WW*	Winter Water in the mPWP model

Mathematical Notation

α		Parameterisation of attenuation of solar irradiation with depth
α_{T}	5.82×10^{-5} °C^{-1}	Thermal expansion coefficient
$\mathbf{A}$		Matrix of endpoints
$\tilde{\mathbf{A}}$		Simulated matrix of endpoints
A (Ch.3)		Area between the curve (observations) and line
A (Ch.5)		Sea ice concentration
A_{grow}	0.77	Sea ice concentration during sea ice formation
A_{melt}	0.6	Sea ice concentration during sea ice melt
β	8×10^{-4}	Salinity contraction coefficient
B	m^2 s^{-3}	Buoyancy flux
$\mathbf{b}$		Observations dataset
$\tilde{\mathbf{b}}$		Simulated observations dataset
χ		Ocean property (e.g. Θ, S_{A}, c(O_2))
χ_{init}		Initial ocean properties (in mPWP)
C_d	10^{-3}	Drag coefficient
c_a	1005 J kg^{-1} °C^{-1}	Specific heat capacity of air
c_i	2108 J kg^{-1} °C^{-1}	Specific heat capacity of ice
c_w	4183.3 J kg^{-1} °C^{-1}	Specific heat capacity of water
c(O_2)	μmol kg^{-1}	Dissolved Oxygen Concentrations
D	m^2 s^{-1}	Molecular diffusivity of oxygen
d		Normalised observations dataset

$\tilde{d}$		Weighted and normalised observations dataset
Δt	s	Time-step in mPWP
Δz	m	Depth increment in mPWP
ϵ_{lw}	0.97	Longwave emissivity of water
ϵ_r	0.622	Ratio of molecular mass of water and dry air
e_w	Pa	Saturated vapour partial pressure
F_{fw}	m s^{-1}	Freshwater flux
f	1.321×10^{-4} rad s^{-1}	Coriolis parameter
G		Normalised matrix of endpoints
$\tilde{G}$		Weighted and normalised matrix of endpoints
g	9.8 m s^{-2}	Gravitational acceleration
h	m	Mixed layer depth
h_{CDW}	m	Thickness of CDW layer
h_i	m	Thickness of sea ice
I	W m^{-2}	Irradiance
I_0	W m^{-1}	Irradiance at surface
K	m^2 s^{-1}	Eddy diffusivity
k	cm h^{-1}	Gas transfer velocity
L_f	3.35×10^5 J Kg^{-1}	Latent heat of fusion
L_v	2.501×10^6 J Kg^{-1}	Latent heat of vaporisation
m	m s^{-1}	Melt rate of sea ice
m_{kt}	0.4	Coefficient for power provided by wind
ν	Pa s	Kinematic viscosity of ocean surface
N	s^{-1}	Brunt-Väisälä frequency
n_{kt}	0.18	Coefficient for power provided by buoyancy
n_{t}		Number of tracers available
n_{w}		Number of water masses to be identified
ψ		Composite tracer

ψ_{ice}		Composite tracer value for ice
ψ_{w}		Composite tracer value in the ambient water column
P_{atm}	101325 Pa	Atmospheric pressure at the surface
P_b	$\text{m}^3\ \text{s}^{-3}$	Power supplied by buoyancy
P_w	$\text{m}^3\ \text{s}^{-3}$	Power supplied by wind
p	m s^{-1}	Precipitation
Q		Mass fraction
Q_{fw}	m s^{-1}	Freshwater flux (evaporation minus precipitation)
Q_{i}	W m^{-2}	Incoming heat flux (shortwave)
Q_{lat}	W m^{-2}	Latent heat flux
Q_{o}	W m^{-2}	Outgoing heat flux
Q_{sens}	W m^{-2}	Sensible heat flux
q		Specific humidity
q_{sat}		Saturated humidity
ρ	kg m^{-3}	Density
ρ_{a}	$1.275\ \text{kg m}^{-3}$	Density of air
ρ_{fw}	$1000\ \text{kg m}^{-3}$	Density of freshwater
ρ_{w}	$1026\ \text{kg m}^{-3}$	Density of water
Ri_B		Bulk Richardson Number
$\text{Ri}_{B,c}$	0.65	Critical value for the bulk Richardson Number
Ri_G		Gradient Richardson Number
$\text{Ri}_{G,c}$	0.25	Critical values for the gradient Richardson Number
σ (Ch.5)	$5.67\times^{-8}$	Stefan-Boltzmann constant
σ (Ch.2)		Standard deviation
σ_θ	kg m^{-3}	Potential Density
S		Practical salinity
S_{A}	g kg^{-1}	Absolute salinity
Sc		Schmidt number

τ_x	N m^{-2}	Zonal wind stress
τ_y	N m^{-2}	Meridional wind stress
Θ	°C	Conservative temperature
Θ_{fp}	°C	Freezing temperature
Θ_i	°C	Far-field ice temperature
Θ_i^*	°C	Effective conservative temperature of ice
θ	°C	Potential temperature
T	°C	Ocean temperature
T_{air}	°C	Air temperature
T_{fp}	°C	Freezing temperature
Tu	°	Turner Angle
v		Uncertainty
U	m s^{-1}	Wind Speed
U_*	m s^{-1}	Friction Velocity
u	m s^{-1}	Zonal current velocity
V	m s^{-1}	Current speed
V_{adv}	0.01 m s^{-1}	Advective current speed
v	m s^{-1}	Meridional current velocity
W		Weighting for OMPA
w_e	m s^{-1}	Vertical entrainment velocity
$\mathbf{x}$		Water mass fraction array
$\mathbf{x}_{\text{MC}}$		Water mass fraction array from Monte Carlo simulations
$\tilde{\mathbf{x}}$		Simulated water mass fraction array
$\mathbf{x}'$		Recalculated (simulated) water mass fraction array
z	m	Depth
z_w	10 m	Depth scale of dissipation

Bibliography

Arrigo, K. R., G. L. van Dijken, and S. Bushinsky (2008), Primary production in the Southern Ocean, 1997âĂŞ2006, *Journal of Geophysical Research*, *113*(C8), C08,004, doi:10.1029/2007JC004551.

Arrigo, K. R., K. E. Lowry, and G. L. V. Dijken (2012), Deep-Sea Research II Annual changes in sea ice and phytoplankton in polynyas of the Amundsen Sea , Antarctica, *Deep-Sea Research Part II*, *71-76*, 5–15, doi:10.1016/j.dsr2.2012.03.006.

Assmann, K. M., a. Jenkins, D. R. Shoosmith, D. P. Walker, S. S. Jacobs, and K. W. Nicholls (2013), Variability of Circumpolar Deep Water transport onto the Amundsen Sea Continental shelf through a shelf break trough, *Journal of Geophysical Research: Oceans*, *118*(12), 6603–6620, doi:10.1002/2013JC008871.

Bamber, J. L., R. E. Riva, B. L. Vermeersen, and A. M. LeBrocq (2009), Reassessment of the Potential of the West Antarctic Ice Sheet, *Science*, *324*, 901–903, doi:10.1126/science.1169335.

BAS (2016), ANiSEED - AmuNdsen Sea Embayment Exposure Dating, https://www.bas.ac.uk/project/reconstructing-millennial-scale-ice-sheet-change/.

Beaird, N., F. Straneo, and W. Jenkins (2015), Spreading of Greenland meltwaters in the ocean revealed by noble gases, *Geophysical Research Letters*, *42*, 1–9, doi:10.1002/2015GL065003.

Biddle, L. C., J. Kaiser, K. J. Heywood, A. F. Thompson, and A. Jenkins (2015), Ocean glider observations of iceberg-enhanced biological production in the northwestern Weddell Sea, *Geophysical Research Letters*, doi:10.1002/2014GL062850.

Bintanja, R., G. J. V. Oldenborgh, S. S. Drijfhout, B. Wouters, and C. A. Katsman (2013), Important role for ocean warming and increased ice-shelf melt in Antarctic sea-ice expansion, *Nature Geoscience*, *6*(4), 1–4, doi:10.1038/ngeo1767.

Castro-Morales, K., N. Cassar, D. R. Shoosmith, and J. Kaiser (2013), Biological production in the Bellingshausen Sea from oxygen-to-argon ratios and oxygen triple isotopes, *Biogeosciences*, *10*, 2273–2291, doi:10.5194/bg-10-2273-2013.

Chen, D., L. M. Rothstein, and A. J. Busalacchi (1994), A Hybrid Vertical Mixing Scheme and Its Application to Tropical Ocean Models, *Journal of Physical Oceanography*, *24*, 2156–2179.

Courant, R., K. Friedrichs, and H. Lewy (1967), On the Partial Difference Equations of Mathematical Physics, *IBM Journal*, (March).

Depoorter, M. A., J. L. Bamber, J. A. Griggs, J. T. M. Lenaerts, S. R. M. Ligtenberg, M. R. van den Broeke, and G. Moholdt (2013), Calving fluxes and basal melt rates of Antarctic ice shelves, *Nature*.

Ducklow, H. W., S. E. Wilson, A. F. Post, S. E. Stammerjohn, M. Erickson, S. H. Lee, K. E. Lowry, R. M. Sherrell, and P. L. Yager (2015), Particle flux on the continental shelf in the Amundsen Sea Polynya and Western Antarctic Peninsula, *Elementa: Science of the Anthropocene*, pp. 1–20, doi:10.12952/journal.elementa.000046.

Duprat, L. P. a. M., G. R. Bigg, and D. J. Wilton (2016), Enhanced Southern Ocean marine productivity due to fertilization by giant icebergs, *Nature Geoscience*, *9*(January), 219–221, doi:10.1038/ngeo2633.

Dutrieux, P., J. De Rydt, A. Jenkins, P. R. Holland, H. K. Ha, S. H. Lee, E. J. Steig, Q. Ding, E. P. Abrahamsen, and M. Schröder (2014), Strong sensitivity of Pine Island ice-shelf melting to climatic variability., *Science (New York, N.Y.)*, *343*(6167), 174–8, doi:10.1126/science.1244341.

Eriksen, C., T. Osse, R. Light, T. Wen, T. Lehman, P. Sabin, J. Ballard, and a.M. Chiodi (2001), Seaglider: a long-range autonomous underwater vehicle for oceanographic research, *IEEE Journal of Oceanic Engineering*, *26*(4), 424–436, doi:10.1109/48.972073.

Field, C. B., V. R. Barros, D. J. Dokken, K. J. Mach, M. D. Mastrandrea, T. E. Bilir, M. Chatterjee, K. L. Ebi, Y. O. Estrada, R. C. Genova, and Others (2014), IPCC, 2014: Climate Change 2014: Impacts, Adaptation, and Vulnerability. Part A: Global and Sectoral Aspects. Contribution of Working Group II to the Fifth Assessment Report of the Intergovernmental Panel on Climate Change.

Fofonoff, N., and R. Millard (1983), Algorithms for computation of fundamental properties of seawater, *Unesco Technical Papers in Marine Science*, *44*.

Galperin, B., S. Sukoriansky, and P. S. Anderson (2007), On the critical Richardson number in stably stratified turbulence, *Atmospheric Science Letters*, *8*(3), 65–69, doi:10.1002/asl.153.

Gaspar, P. (1988), Modeling the Seasonal Cycle of the Upper Ocean, *Journal of Physical Oceanography*, *18*(2), 161–180, doi:10.1175/1520-0485(1988)018<0161:MTSCOT>2.0.CO;2.

Gill, A. E. (1982), *Atmosphere-ocean dynamics*, vol. 30, Academic press.

Gladstone, R., G. Bigg, and K. Nicholls (2001), Iceberg trajectory modeling and meltwater injection in the Southern Ocean, *Journal of Geophysical Research*, *106*, 19,903–15.

Gordon, C., C. Cooper, C. a. Senior, H. Banks, J. M. Gregory, T. C. Johns, J. F. B. Mitchell, and R. a. Wood (2000), The simulation of SST, sea ice extents and ocean heat transports in a version of the Hadley Centre coupled model without flux adjustments, *Climate Dynamics*, *16*, 147–168, doi:10.1007/s003820050010.

Greenbaum, J. S., D. D. Blankenship, D. a. Young, T. G. Richter, J. L. Roberts, a. R. a. Aitken, B. Legresy, D. M. Schroeder, R. C. Warner, T. D. van Ommen, and M. J. Siegert (2015), Ocean access to a cavity beneath Totten Glacier in East Antarctica, *Nature Geoscience*, *8*(March), 6–10, doi:10.1038/NGEO2388.

Hahm, D., T. S. Rhee, H. C. Kim, J. Park, Y. N. Kim, H. C. Shin, and S. Lee (2014), Spatial and temporal variation of net community production and its regulating factors in the Amundsen Sea, Antarctica, *Journal of Geophysical Research: Oceans*, *119*(5), 2815–2826, doi:10.1002/2013JC009762.

Hellmer, H., S. S. Jacobs, and A. Jenkins (1998), Oceanic erosion of a floating Antarctic glacier in the Amundsen Sea, in *Ocean, Ice, and Atmosphere: Interactions at the Antarctic Continental Margin*, edited by S. S. Jacobs and R. Weiss, pp. 83–99, American Geophysical Union.

Helly, J. J., R. S. Kaufmann, G. R. Stephenson, and M. Vernet (2011), Cooling , dilution and mixing of ocean water by free-drifting icebergs in the Weddell Sea, *Deep-Sea Research Part II*, *58*(11-12), 1346–1363, doi:10.1016/j.dsr2.2010.11.010.

Howard, L. N. (1961), Note on a paper of John W. Miles, *Journal of Fluid Mechanics*, *10*(04), 509–512.

Huppert, H. E., and J. S. Turner (1980), Ice blocks melting into a salinity gradient, *Journal of Fluid Mechanics*, *100*(2), 367–384.

IOC, SCOR, and IAPSO (2010), The international thermodynamic equation of seawater - 2010: Calculation and use of thermodynamics properties., in *Intergovernmental Oceanographic Commission, Manuals and Guides No. 56*, p. 196, UNESCO (English).

Jacobs, S., A. Jenkins, H. Hellmer, C. Giulivi, F. Nitsche, B. Huber, and R. Guerrero (2012), The Amundsen Sea and the Antarctic Ice Sheet, *Oceanography*, *25*(3), 154–163, doi: http://dx.doi.org/10.5670/oceanog.2012.90.

Jacobs, S. S. (1991), On the nature and significance of the Antarctic Slope Front, *Marine Chemistry*, *35*(1-4), 9–24, doi:10.1016/S0304-4203(09)90005-6.

Jacobs, S. S., and C. F. Giulivi (2010), Large multidecadal salinity trends near the Pacific-Antarctic continental margin, *Journal of Climate*, *23*(17), 4508–4524, doi: 10.1175/2010JCLI3284.1.

Jacobs, S. S., H. H. Hellmer, and A. Jenkins (1996), Antarctic ice sheet melting in the Southeast Pacific, *Geophysical Research Letters*, *23*(9), 957–960.

Jacobs, S. S., C. F. Giulivi, and P. A. Mele (2002), Freshening of the Ross Sea During the Late 20th Century, *Science*, *297*(July), 386–390.

Jacobs, S. S., A. Jenkins, C. F. Giulivi, and P. Dutrieux (2011), Stronger ocean circulation and increased melting under Pine Island Glacier ice shelf, *Nature Geoscience*, *4*(8), 519–523, doi:10.1038/ngeo1188.

Jenkins, A. (1999), The impact of melting ice on ocean waters, *Journal of Physical Oceanography*, (3), 2370–2381.

Jenkins, A., and S. Jacobs (2008), Circulation and melting beneath George VI Ice Shelf, Antarctica, *Journal of Geophysical Research*, *113*(C4), C04,013, doi: 10.1029/2007JC004449.

Jenkins, A., P. Dutrieux, S. S. Jacobs, S. D. McPhail, J. R. Perrett, A. T. Webb, and D. White (2010), Observations beneath Pine Island Glacier in WestÂăAntarctica and implications for its retreat, *Nature Geoscience*, *3*(7), 468–472, doi:10.1038/ngeo890.

Jenkins, A., P. Dutrieux, S. Jacobs, S. Mcphail, J. Perrett, A. Webb, and D. White (2012), Autonomous Underwater Vehicle Exporation of the Ocean Cavity Beneath an Antarctic Ice Shelf, *Oceanography*, *25*(3), 202–203, doi:10.5670/oceanog.2012.95.

Jerlov, N. G. (1968), *Optical oceanography*, vol. 5, Elsevier Amsterdam.

Joughin, I., B. E. Smith, and B. Medley (2014), Marine Ice Sheet Collapse Potentially Under Way for the Thwaites Glacier Basin, West Antarctica, *Science*, (May), 735–739.

Karstensen, J., and M. Tomczak (1997), Ventilation processes and water mass ages in the thermocline of, *Geophysical Research Letters*, *24*(22), 2777–2780.

Keeling, R. F. (1993), On the role of large bubbles in air-sea gas exchange and supersaturation in the ocean, *Journal of Marine Research*, *51*(2), 237–271, doi:10.1357/0022240933223800.

Kim, I., D. Hahm, T. S. Rhee, T. W. Kim, C.-S. Kim, and S. Lee (2016), The distribution of glacial meltwater in the Amundsen Sea, Antarctica, revealed by dissolved helium and neon, *Journal of Geophysical Research : Oceans*, *121*, 1–12, doi:10.1002/2015JC011211.

King and J. Turner., J. C. (1997), *Antarctic Meteorology and Climatology*, Cambridge University Press.

Kouketsu, S., M. Fukasawa, I. Kaneko, T. Kawano, H. Uchida, T. Doi, M. Aoyama, and K. Murakami (2009), Changes in water properties and transports along 24??N in the North pacific between 1985 and 2005, *Journal of Geophysical Research: Oceans*, *114*(1), 1–15, doi:10.1029/2008JC004778.

Kraus, E. B., and J. S. Turner (1967), A one-dimensional model of the seasonal thermocline, *Tellus*, *29*, 98–106.

Lancelot, C., A. de Montety, H. Goosse, S. Becquecvort, V. Schoemann, B. Pasquer, and M. Vancoppenolle (2009), Spatial distribution of the iron supply to phytoplankton in the Southern Ocean: a model study, *Biogeosciences*, *6*, 2861–2878.

Large, W. G., J. C. Mcwilliams, and S. C. Doney (1994), Oceanic Vertical Mixing - a Review and a Model with a Nonlocal Boundary-Layer Parameterization, *Reviews of Geophysics*, *32*(94), 363–403, doi:10.1029/94rg01872.

Lazarevich, P., and S. Stoermer (2001), A Matlab version of the Price, Weller, Pinkel model, http://www.po.gso.uri.edu/rafos/research/pwp/.

Lin, H., S. Rauschenberg, C. R. Hexel, T. J. Shaw, and B. S. Twining (2011), Free-drifting icebergs as sources of iron to the Weddell Sea, *Deep-Sea Research Part II*, *58*(11-12), 1392–1406, doi:10.1016/j.dsr2.2010.11.020.

Loose, B., and W. J. Jenkins (2014), The five stable noble gases are sensitive unambiguous tracers of glacial meltwater, *Geophysical Research Letters*, *41*, 2835–2841, doi:10.1002/2013GL058804.Received.

Loose, B., P. Schlosser, W. M. Smethie, and S. Jacobs (2009a), An optimized estimate of glacial melt from the Ross Ice Shelf using noble gases, stable isotopes, and CFC transient tracers, *Journal of Geophysical Research: Oceans*, *114*(8), 1–15, doi: 10.1029/2008JC005048.

Loose, B., W. R. McGillis, P. Schlosser, D. Perovich, and T. Takahashi (2009b), Effects of freezing, growth, and ice cover on gas transport processes in laboratory seawater experiments, *Geophysical Research Letters*, *36*(5), 1–5, doi:10.1029/2008GL036318.

Marra, J. (2009), Net and gross productivity: weighing in with 14C, *Aquatic Microbial Ecology*, *56*(September), 123–131, doi:10.3354/ame01306.

Martin, J., R. Gordon, and S. Fitzwater (1990), Iron in Antarctic waters, *Nature*, *345*, 156–158.

Martin, J. H., G. a. Knauer, D. M. Karl, and W. W. Broenkow (1987), VERTEX: carbon cycling in the northeast Pacific, *Deep Sea Research Part A, Oceanographic Research Papers*, *34*(2), 267–285, doi:10.1016/0198-0149(87)90086-0.

Martinerie, P., D. Raynaud, D. M. Etheridge, J.-M. Barnola, and D. Mazaudier (1992), Physical and climatic parameters which influence the air content in polar ice, *Earth and Planetary Science Letters*, *112*(1-4), 1–13, doi:10.1016/0012-821X(92)90002-D.

Martz, T. R., K. S. Johnson, and S. C. Riser (2008), Ocean metabolism observed with oxygen sensors on profiling floats in the South Pacific, *Limnology and Oceanography*, *53*(5, part 2), 2094–2111, doi:10.4319/lo.2008.53.5_part_2.2094.

McNeil, C., and E. D'Asaro (2007), Parameterization of air-sea gas fluxes at extreme wind speeds, *Journal of Marine Systems*, *66*(1-4), 110–121, doi:10.1016/j.jmarsys.2006.05.013.

Mellor, G. L., and T. Yamada (1982), Development of a Turbulence Closure Model for Geophysical Fluid Problems, *Reviews of Geophysics and Space Physics*, *20*(4), 851–875.

MetOffice (2016), Record breaking winter for England and Wales, http://www.metoffice.gov.uk/news/releases/2016/winter-statistics.

Miles, J. W. (1961), On the stability of heterogeneous shear flows, *Journal of Fluid Mechanics*, *10*(04), 496–508.

Munk, W., and C. Wunsch (1998), Abyssal recipes II: Energetics of tidal and wind mixing, *Deep-Sea Research Part I: Oceanographic Research Papers*, *45*(12), 1977–2010, doi: 10.1016/S0967-0637(98)00070-3.

Nakayama, Y., M. Schröder, and H. Hellmer (2013), From circumpolar deep water to the glacial meltwater plume on the eastern Amundsen Shelf, *Deep Sea Research Part I: Oceanographic Research Papers*, *77*, 50–62, doi:10.1016/j.dsr.2013.04.001.

Nakayama, Y., R. Timmermann, C. B. Rodehacke, M. Schröder, and H. H. Hellmer (2014), Modeling the spreading of glacial meltwater from the Amundsen and Bellingshausen Seas, *Geophysical Research Letters*, *41*, 7942–7949, doi:10.1002/2014GL061600.1.

NASA/GISS (2016), Climate Change: Vital Signs of the Planet: Effects, http://climate.nasa.gov/effects.

Naveira-Garabato, A. C., A. Forryan, P. Dutrieux, L. Brannigan, L. C. Biddle, K. J. Heywood, A. Jenkins, Y. L. Firing, and S. Kimura (), Vigorous lateral export of the meltwater outflow from beneath an Antarctic ice shelf, *Nature Geoscience (submitted)*.

Neshyba, S. (1977), Upwelling by icebergs, *Nature*, *267*, 508.

Niiler, P. P. (1975), Deepening of wind-mixed layer, *Journal of Marine Research*, *33*(3), 405–422.

Niiler, P. P., and E. B. Kraus (1977), One-dimensional models of the Upper Ocean, in *Modelling and Prediction of the Upper Layers of the Ocean*, pp. 143–172, Pergamon.

Nitsche, F. O., S. S. Jacobs, R. D. Larter, and K. Gohl (2007), Bathymetry of the Amundsen Sea continental shelf: Implications for geology, oceanography, and glaciology, *Geochemistry, Geophysics, Geosystems*, *8*(10), 1–10, doi:10.1029/2007GC001694.

NOAA (2016), Winter was record warm for the contiguous U.S., http://www.noaa.gov/winter-was-record-warm-contiguous-us.

Paolo, F. S., H. A. Fricker, and L. Padman (2015), Volume loss from Antarctic ice shelves is accelerating, *Science*, *348*(6232), 327–332, doi:10.1126/science.aaa0940.

Parkinson, C. L., and W. M. Washington (1979), A Large-Scale Numerical Model of Sea Ice, *Journal of Geophysical Research*, *84*(8), 311–337.

Paulson, C. A., and J. J. Simpson (1977), Irradiance measurements in the upper ocean, *Journal of Physical Oceanography*, *7*, 952–956, doi:10.1175/1520-0485(1977)007<0952:IMITUO>2.0.CO;2.

Payne, A. J., A. Vieli, A. P. Shepherd, D. J. Wingham, and E. Rignot (2004), Recent dramatic thinning of largest west antarctic ice stream triggered by oceans, *Geophysical Research Letters*, *31*, L23,401, doi:10.1029/2004GL021284.

Petty, A. A., D. L. Feltham, and P. R. Holland (2013), Impact of Atmospheric Forcing on Antarctic Continental Shelf Water Masses, *Journal of Physical Oceanography*, *43*(5), 920–940, doi:10.1175/JPO-D-12-0172.1.

Poole, R., and M. Tomczak (1999), Optimum multiparameter analysis of the water mass structure in the Atlantic Ocean thermocline, *Deep Sea Research I*, *46*, 1895–1921.

Price, J. F., C. N. K. Mooers, and J. C. Van Leer (1978), Observation and Simulation of Storm-Induced Mixed-Layer Deepening, doi:10.1175/1520-0485(1978)008<0582:OASOSI>2.0.CO;2.

Price, J. F., R. A. Weller, and R. Pinkel (1986), Diurnal Cycling ' Observations and Models of the Upper Ocean Response to Diurnal Heating , Cooling , and Wind Mixing, *Journal of Geophysical Research*, *91*, 8411–8427.

Pritchard, H. D., S. R. M. Ligtenberg, H. a. Fricker, D. G. Vaughan, M. R. van den Broeke, and L. Padman (2012), Antarctic ice-sheet loss driven by basal melting of ice shelves., *Nature*, *484*(7395), 502–5, doi:10.1038/nature10968.

Purkey, S. G., and G. C. Johnson (2012), Global contraction of Antarctic Bottom Water between the 1980s and 2000s, *Journal of Climate*, *25*(17), 5830–5844, doi:10.1175/JCLI-D-11-00612.1.

Raiswell, R., L. Benning, M. Tranter, and S. Tulaczyk (2008), Bioavailable iron in the Southern Ocean: the significance of the iceberg conveyor belt., *Geochemical Transactions*, *9*(7).

Randall-Goodwin, E., M. P. Meredith, a. Jenkins, P. L. Yager, R. M. Sherrell, E. P. Abrahamsen, R. Guerrero, X. Yuan, R. a. Mortlock, K. Gavahan, a. C. Alderkamp, H. Ducklow, R. Robertson, and S. E. Stammerjohn (2015), Freshwater distributions and water mass structure in the Amundsen Sea Polynya region, Antarctica, *Elementa: Science of the Anthropocene*, *3*(1), 000,065, doi:10.12952/journal.elementa.000065.

Richardson, G., M. R. Wadley, K. J. Heywood, D. P. Stevens, and H. T. Banks (2005), Short-term climate response to a freshwater pulse in the Southern Ocean, *Geophysical Research Letters*, *32*(3), 1–4, doi:10.1029/2004GL021586.

Rignot, E. (1998), Fast Recession of a West Antarctic Glacier, *Science*, *281*, 549–551.

Rignot, E., J. L. Bamber, M. R. V. D. Broeke, C. Davis, Y. Li, W. J. V. D. Berg, and E. V. Meijgaard (2008), Recent Antarctic ice mass loss from radar interferometry and regional climate modelling, *Nature Geoscience*, *1*(February), 106–110, doi:10.1038/ngeo102.

Rintoul, S. R. (2007), Rapid freshening of Antarctic Bottom Water formed in the Indian and Pacific oceans, *Geophysical Research Letters*, *34*(6), L06,606, doi:10.1029/2006GL028550.

Riser, S. C., and K. S. Johnson (2008), Net production of oxygen in the subtropical ocean, *Nature*, *451*(7176), 323–325.

Saha, S., S. Nadiga, C. Thiaw, J. Wang, W. Wang, Q. Zhang, H. M. Van den Dool, H.-L. Pan, S. Moorthi, D. Behringer, D. Stoke, M. Pena, S. Lord, G. White, W. Ebisuzaki, P. Peng, and P. Xie (2006), The NCEP Climate Forecast System, *Journal of Climate*, *19*(15), 3483–3517, doi:10.1175/JCLI3812.1.

Sancetta, C. (1992), Primary production in the glacial North Atlantic and North Pacific oceans, *Nature*, *360*, 249–251.

Scambos, T., C. Hulbe, M. Fahnestock, and J. Bohlander (2000), The link between climate warming and break-up of ice shelves in the Antarctic Peninsula, *Journal of Glaciology*, *46*, 516–530.

Schmidtko, S., K. J. Heywood, A. F. Thompson, and S. Aoki (2014), Multidecadal warming of Antarctic waters, *Science (New York, N.Y.)*, *346*(6214), 1227–1232.

Schodlok, M. P., D. Menemenlis, E. Rignot, and M. Studinger (2012), Sensitivity of the ice-shelf/ocean system to the sub-ice-shelf cavity shape measured by NASA IceBridge in Pine Island Glacier, West Antarctica, *Annals of Glaciology*, *53*(60), 156–162.

Schoof, C. (2007), Ice sheet grounding line dynamics : Steady states , stability , and hysteresis, *Journal of Geophysical Research*, *112*(August 2006), 1–19, doi:10.1029/2006JF000664.

Schwarz, J. N. . A., and M. P. Schodlok (2009), Impact of drifting icebergs on surface phytoplankton biomass in the Southern Ocean : Ocean colour remote sensing and in situ iceberg tracking, *Deep Sea Research I*, *56*, 1727–1741, doi:10.1016/j.dsr.2009.05.003.

Semtner Jr, A. J. (1976), A model for the thermodynamic growth of sea ice in numerical investigations of climate, *Journal of Physical Oceanography*, *6*(3), 379–389.

Shaw, T., R. Raiswell, C. Hexel, H. Vu, W. Moore, R. Dudgeon, and K. Smith (2011), Input, composition, and potential impact of terrigenous material from free-drifting icebergs in the Weddell Sea, *Deep Sea Research Part II: Topical Studies in Oceanography*, *58*(11-12), 1376–1383, doi:10.1016/j.dsr2.2010.11.012.

Shepherd, A., D. J. Wingham, and E. Rignot (2004), Warm ocean is eroding West Antarctic Ice Sheet, *Geophysical Research Letters*, *31*(23), 4–7, doi:10.1029/2004GL021106.

Smith, K. L. (2011), Free-drifting icebergs in the Southern Ocean : An overview, *Deep-Sea Research Part II*, *58*(11-12), 1277–1284, doi:10.1016/j.dsr2.2010.11.003.

Smith, K. L., K. L. S. Jr, B. H. Robison, J. J. Helly, R. S. Kaufmann, H. A. Ruhl, T. J. Shaw, B. S. Twining, and M. Vernet (2007), Free-Drifting Icebergs : Hot Spots of Chemical and Biological Enrichment in the Weddell Sea, *Science*, *317*, 478–482, doi: 10.1126/science.1142834.

Stammerjohn, S. E., T. Maksym, R. A. Massom, K. E. Lowry, K. R. Arrigo, X. Yuan, M. Raphael, E. Randall-Goodwin, R. M. Sherrell, and P. L. Yager (2015), Seasonal sea ice changes in the Amundsen Sea, Antarctica, over the period of 1979 – 2014, *Elementa: Science of the Anthropocene*, *3*(1), 000,055, doi:10.12952/journal.elementa.000055.

Steig, E. J., Q. Ding, D. S. Battisti, and A. Jenkins (2012), Tropical forcing of Circumpolar Deep Water Inflow and outlet glacier thinning in the Amundsen Sea Embayment , West Antarctica, *Annals of Glaciology*, (53), 19–28, doi:10.3189/2012AoG60A110.

Stommel, H. (1961), Thermohaline convection with two stable regimes of flow, *Tellus*, *13*(2), 224–230.

Stuart, K., and D. Long (2011), Tracking large tabular icebergs using the SeaWinds Ku-Band microwave scatterometer, *Deep Sea Research II*, *58*, 1285–300.

Sverdrup, H. U., M. W. Johnson, R. H. Fleming, and Others (1942), *The Oceans: Their physics, chemistry, and general biology*, vol. 7, Prentice-Hall New York.

Thoma, M., A. Jenkins, D. Holland, and S. Jacobs (2008), Modelling Circumpolar Deep Water intrusions on the Amundsen Sea continental shelf, Antarctica, *Geophysical Research Letters*, *35*(18), L18,602, doi:10.1029/2008GL034939.

Thompson, A. F., and K. J. Heywood (2008), Frontal structure and transport in the northwestern Weddell Sea, *Deep Sea Research I*, *55*, 1229–1251, doi:10.1016/j.dsr.2008.06.001.

Thompson, A. F., J. Willis, A. Payne, and Others (2015), The Sleeping Giant: Measuring Ocean-Ice Interactions in Antarctica, *Tech. rep.*

Thurnherr, A., S. S. Jacobs, P. Dutrieux, and C. F. Giulivi (2014), Export and circulation of ice cavity water in Pine Island Bay, West Antarctica, *Journal of Geophysical Research : Oceans*, pp. 1754–1764, doi:10.1002/2013JC009307.

Tomczak, M. (1981), A multi-parameter extension of temperature / salinity diagram techniques for the analysis of non-isopycnal mixing, *Progress in Oceanography*, *10*, 147–171.

Tomczak, M., and D. G. B. Large (1989), Optimum Multiparameter Analysis of Mixing in the Thermocline of the Eastern Indian Ocean, *Journal of Geophysical Research*, *94*(Cll).

Turner, J. S. (1973), *Buoyancy effects in fluids*, Cambridge University Press.

UNFCCC (2016), Report of the Conference of the Parties on its twenty-first session, held in Paris from 30 November to 13 December 2015, *Tech. rep.*

Vaughan, D., A. Smith, and H. Corr (2001), *A REVIEW OF PINE ISLAND GLACIER, WEST ANTARCTICA: HYPOTHESES OF INSTABILITY VS. OBSERVATIONS OF CHANGE*, vol. 77, 237–256 pp.

Vernet, M., K. Sines, D. Chakos, A. O. Cefarelli, and L. Ekern (2011), Impacts on phytoplankton dynamics by free-drifting icebergs in the NW Weddell Sea, *Deep-Sea Research Part II*, *58*(11-12), 1422–1435, doi:10.1016/j.dsr2.2010.11.022.

Wåhlin, A. K., X. Yuan, G. Björk, and C. Nohr (2010), Inflow of Warm Circumpolar Deep Water in the Central Amundsen Shelf, *Journal of Physical Oceanography*, *40*(6), 1427–1434, doi:10.1175/2010JPO4431.1.

Walker, D. P., M. A. Brandon, A. Jenkins, J. T. Allen, J. A. Dowdeswell, and J. Evans (2007), Oceanic heat transport onto the Amundsen Sea shelf through a submarine glacial trough, *Geophysical Research Letters*, *34*(2), L02,602, doi:10.1029/2006GL028154.

Walker, D. P., A. Jenkins, K. M. Assmann, D. R. Shoosmith, and M. a. Brandon (2013), Oceanographic observations at the shelf break of the Amundsen Sea, Antarctica, *Journal of Geophysical Research: Oceans*, *118*(6), 2906–2918, doi:10.1002/jgrc.20212.

Wanninkhof, R. (2014), Relationship between wind speed and gas exchange over the ocean, *Limnology and Oceanography: Methods*, *12*, 351–362, doi:10.1029/92JC00188.

Webber, B., K. J. Heywood, D. P. Stevens, P. Dutrieux, E. P. Abrahamsen, A. Jenkins, S. S. Jacobs, H. K. Ha, S. H. Lee, and T. W. Kim (), Mechanisms driving variability in the ocean forcing of Pine Island Glacier, *Nature Communications (in review)*.

Westberry, T. K., and M. J. Behrenfeld (2014), Oceanic net primary production, in *Biophysical Applications of Satellite Remote Sensing*, pp. 205–230, Springer.

WMO (2008), Guide to Meteorological Instruments and Methods of Observation, *Tech. rep.*

Wüst, G. (1935), Schichtung und Zirkulation des Atlantischen Ozeans. Die Stratosph{ä}re des Atlantischen Ozeans: Wissenschaftliche Ergebnisse Deutschen Atlantischen Expedition auf dem Forschungs und Vermessungsschiff, *" Meteor" 1925-1927*, *6*.

Yager, P., L. Sherrell, S. E. Stammerjohn, a. Alderkamp, O. M. Schofield, A. Ep, K. R. Arrigo, S. Bertilsson, D. Garay, R. Guerrero, K. Lowry, P. Moksnes, K. Ndungu, A. Post, E. Randall-Goodwin, L. Riemann, S. Severmann, S. Thatje, G. L. van Dijken, and S. Wilson (2012), ASPIRE: The Amundsen Sea Polynya International Research Expedition, *Oceanography*, *25*(3), 40–53, doi:10.5670/oceanog.2012.73.

You, Y. (2002), A global ocean climatological atlas of the Turner angle : implications for double-diffusion and water-mass structure, *Deep Sea Research I*, *49*(2002), 2075–2093.